https://doi.org/10.15388/vu.thesis.119
https://orcid.org/0000-0002-0000-3004

VILNIUS UNIVERSITY
STATE RESEARCH INSTITUTE CENTER FOR PHYSICAL SCIENCES AND TECHNOLOGY

Jonas
KLIMANTAVIČIUS - KLIMANTAS

Tuning of Magnetoresistive Properties of Nanostructured La-Sr-Mn-O Films

DOCTORAL DISSERTATION

Technological Sciences,
Material Engineering (T008)

Vilnius, 2020

This dissertation was written between 2015 and 2019 at State research institute Center for Physical Sciences and Technology. Part of the results of the dissertation have been obtained by implementing SMAPS project, supported by the Research Council of Lithuania under Grant S-MIP-17-110.

Academic supervisor:
Prof. Dr. Nerija Žurauskienė (State research institute Center for Physical Sciences and Technology, Material engineering – T 008).

This doctoral dissertation will be defended in a public meeting of the Dissertation Defence Panel:
Chairman - Prof. Dr. Kęstutis Arlauskas (Vilnius University, Technological Sciences, Material Engineering – T 008).
Members:
Doc. Dr. Renata Butkutė (State research institute Center for Physical Sciences and Technology, Technological Sciences, Material Engineering – T 008).
Prof. Dr. Alvydas Lisauskas (Institute of High Pressure Physics of the Polish Academy of Sciences, Natural Sciences, Physics - N 002).
Dr. Šarūnas Meškinis (Kaunas University of Technology, Technological Sciences, Material Engineering – T 008).
Prof. Dr. Jurij Novickij (Vilnius Gediminas Technical University, Technological Sciences, Electrical and Electronics Engineering - T 001).

The dissertation will be defended at the public meeting of the Dissertation Defence Panel at 14:00 on the 18^{th} of December, 2020 in the Center for Physical Sciences and Technology.
Address: Saulėtekio Ave. 3, Vilnius, Lithuania.

The text of this dissertation can be accessed at the libraries of Vilnius University, library of the State research institute Center for Physical Sciences and Technology as well as on the website of Vilnius University:
www.vu.lt/lt/naujienos/ivykiu-kalendorius.

https://doi.org/10.15388/vu.thesis.119
https://orcid.org/0000-0002-0000-3004

VILNIAUS UNIVERSITETAS
VALSTYBINIS MOKSLINIŲ TYRIMŲ INSTITUTAS FIZINIŲ IR
TECHNOLOGIJOS MOKSLŲ CENTRAS

Jonas
KLIMANTAVIČIUS - KLIMANTAS

Magnetovaržinių savybių valdymas nanostruktūrizuotuose La-Sr-Mn-O sluoksniuose

DAKTARO DISERTACIJA

Technologijos mokslai,
medžiagų inžinerija (T008)

Vilnius, 2020

Disertacija rengta 2015 - 2019 metais Valstybiniame mokslinių tyrimų institute Fizinių ir technologijos mokslų centre. Dalis šios disertacijos tyrimų rezultatų buvo gauta, vykdant SMAPS projektą, remiamą Lietuvos mokslo tarybos (sutarties Nr. S-MIP-17-110).

Mokslinis vadovas:
prof. dr. Nerija Žurauskienė (Valstybinis mokslinių tyrimų institutas Fizinių ir technologijos mokslų centras, technologijos mokslai, medžiagų inžinerija – T 008).

Gynimo taryba:
Pirmininkas - **prof. dr. Kęstutis Arlauskas** (Vilniaus universitetas, technologijos mokslai, medžiagų inžinerija – T 008).
Nariai:
doc. dr. Renata Butkutė (Valstybinis mokslinių tyrimų institutas Fizinių ir technologijos mokslų centras, technologijos mokslai, medžiagų inžinerija – T 008).
prof. dr. Alvydas Lisauskas (Lenkijos mokslų akademijos Aukšto slėgio fizikos institutas, gamtos mokslai, fizika - N 002).
dr. Šarūnas Meškinis (Kauno technologijos universitetas, technologijos mokslai, medžiagų inžinerija – T 008).
prof. dr. Jurij Novickij (Vilniaus Gedimino technikos universitetas, technologijos mokslai, elektros ir elektronikos inžinerija - T001).

Disertacija ginama viešame Gynimo tarybos posėdyje 2020 m. gruodžio mėn. 18 d. 14 val. VMTI FTMC A101 auditorijoje.
Adresas: Saulėtekio al. 3, Vilnius, Lietuva.

Disertaciją galima peržiūrėti Vilniaus universiteto bibliotekose, Fizinių, technologijos mokslų centro bibliotekoje adresu Saulėtekio al. 3. ir VU interneto svetainėje adresu: https://www.vu.lt/naujienos/ivykiu-kalendorius

Acknowledgements

The first and most important acknowledgement is to my scientific supervisor prof. dr. Nerija Žurauskienė: her passion to develop CMR sensors and equipment has motivated me to enter this research area, her enthusiasm and devotion have motivated me to complete this work.

I sincerely thank prof. dr. Saulius Balevičius - he, together with prof. dr. Nerija Žurauskienė, have encouraged me to embrace this endeavour and consulted throughout the work.

I very much appreciate contribution of prof. dr. Voitech Stankevič: knowledge sharing, managing project, experimental work and friendly advises while preparing this work. The research results came to light due to valuable scientific input of dr. Skirmantas Keršulis, dr. Valentina Plaušinaitienė, dr. Česlovas Šimkevičius and dr. Bonifacas Vengalis.

I was interesting to work with the colleagues in projects, dr. Rasuolė Lukošė and Milita Vagner, Justas Dilys and get useful knowledge from of dr. Dainius Pavilonis.

The international perspective to the practical implementation of the CMR technology came from discussions with dr. Emil Spahn, the application in MPW came from discussions with dr. Jörg Bellman and dr. Jörn Lueg-Althoff, it was a pleasure to work with him on MPW tests. I also thank prof. dr. Erman Tekkaya and dr. Marlon Hahn for support in SMAPS project and providing facilities and resources for MPW testing.

I thank prof. dr Kęstutis Arlauskas and dr. Renata Butkutė for reviewing this dissertation and providing valuable recommendations, Scientific Comittee, especially prof. dr. Valdas Sirutkaitis for monitoring progress, support and advices.

The patience of my colleagues from Laser LT Digital Innovations Hub and Science Technology and Innovation Agency dr. Gediminas Račiukaitis and Paulius Petrauskas helped to keep pace writing the Dissertation.

I am very happy with my family, Miglė, Saulė and Adomas and my Mother Nijolė support and motivation through these several years.

Life is a journey and I am thankful for this part of it ...

Jonas Klimantavičius - Klimantas
Vilnius

Table of Contents

List of abbreviations

AF Antiferromagnetic
AFM Atomic Force Microscopy
CMR Colossal Magnetoresistance
DE Double Exchange
EDS Energy Dispersive X-ray Spectroscopy
EMF Electromotive force
FESEM Field Emission Scanning Electron Microscope
FI Ferromagnetic Insulator
FM Ferromagnetic Metal
GB Grain Boundary
HFMR High-Field Magnetoresistance
LCMO or La-Ca-Mn-O $\mathrm{La_{1-x}Ca_xMnO_3}$
LFMR Low-Field Magnetoresistance
LSMO or La-Sr-Mn-O $\mathrm{La_{1-x}Sr_xMnO_3}$
MFM Magnetic Force Microscope
MPW Magnetic Pulse Welding
MOCVD Metal Organic Chemical Vapour Deposition
MRA Magnetoresistance anisotropy
MR Magnetoresistance
PI Paramagnetic Insulator
PI MOCVD Pulsed-Injection Metalorganic Chemical Vapor Deposition
PM Paramagnetic Metal
RHEED Reflection High-Energy Electron Diffraction
SEM Scanning Electron Microscopy
TEM Transmission Electron Microscopy
VRH Variable range hopping

Chapter 1

Introduction

Motivation.

The magnetoresistive properties of lanthanum manganites $\mathrm{La_{1-x}A_xMnO_3}$ (where A is an alkaline-earth cation) are attracting considerable interest of research and applications [1, 2]. Nanostructured manganite La-Sr-Mn-O films which exhibit colossal magnetoresistance (CMR) effect can be successfully used for the development of CMR-B-scalar sensors operating at room temperatures [3, 4]. These sensors allow measurements of absolute magnitude of magnetic flux density during high magnetic field pulses in very small volumes.

The negative CMR phenomenon is based on the decrease of the manganite resistivity in the applied magnetic field, and can be explained in a simplified manner by the double-exchange mechanism [5] when the electrical transport is carried out by the hopping of the electron between Mn^{3+} and a Mn^{4+} ions through an oxygen. The application of an external magnetic field aligns the magnetic moments of the manganese ions and enhances hopping probability, thereby causing a decrease of the manganite resistivity.

However, the magnetoresistance (MR) of manganite films decreases at temperatures higher than metal-insulator transition temperature (T_m) and it is important to increase the operating temperature of the films for use in CMR-B-scalar sensors, still keeping high sensitivity to magnetic field. The magnetoresistance of manganite films strongly depends on the chemical composition, crystal structure and deposition [6].

The polycrystalline manganite films exhibit high MR values in a wide temperature range down from T_m, but for optimal Sr content not higher than 250 K

T_m can be achieved. At higher temperatures in a paramagnetic phase the MR rapidly decreases [7, 8]. Nevertheless, a number of publications reported, that a strong variation of the electronic and magnetic properties can be achieved with defects such as La vacancies, induced by Mn excess.

CMR-B-scalar sensors were successfully used for the investigation of the electrodynamic processes in railguns and to measure the parameters of the magnetic field pulses and the distribution of the magnetic fields in nondestructive high magnetic field coils [9, 10]. In these cases, the maximal magnitude of the magnetic field pulses ranged from 10 Tesla to 91.4 Tesla when rise time of the pulses varied from 0.1 ms up to 20 ms. The magnitude measurement error due to the small anisotropy effect of this "CMR-B-scalar" sensor at such high magnetic fields was no more than $\pm$ 2%.

One of the possible applications of the CMR-B-scalar sensors could be measurement of magnetic field dynamics during Magnetic Pulse Welding process. Magnetic Pulse Welding (MPW) is a collision welding process, which uses a high velocity impact to join two metals. This method allows joining similar and dissimilar metals without external heat input and without critical formation of intermetallic phases. One of the simplest ways of obtaining information about the electromagnetic processes which take place during MPW is to measure the waveform of the current in the magnetic coil which is a result of the capacitor discharge through the resistive and inductive elements of the welding system (the coil, field shaper, workpiece, transmission line, etc.). However, this method is not sensitive enough and it has been suggested that the magnetic field could be measured directly in the small gap between the field shaper and the workpiece. For this purpose, various research groups have developed custom probes for the measurement of the magnetic field in the active zone of the coil [11, 12], but the use of such sensors does not completely solve the challenges that prevent detailed studies of the impact and welding procedure in MPW. An alternative to these measurement methods could be an analytical investigation of the magnetic field dynamics in the gap between the coil or field shaper and the flyer during the MPW process with the use of B-scalar CMR sensors. Each application requires special sensors with parameters determined in advance. Therefore, the investigation of magnetoresistive properties of lanthanum manganites in order to tune their main characteristics for fulfillment of application requirements is of great importance.

The aim of the work. The main aim of the present work is to investigate possibility to tune magnetoresistive properties of $\mathrm{La_{1-x}Sr_xMn_yO_3}$ manganite films in a wide range of temperatures and magnetic fields by changing techno-

logical conditions and substrates for film deposition, and to investigate possibility to measure magnetic field dynamics in magnetic pulse welding of metals.

The tasks of the work.

1. To investigate how variation in technological conditions during PI MOCVD, such as deposition temperature and thickness of $La_{1-x}Sr_xMnO_3$ films deposited on glass-ceramics substrate, influence on the magnetoresistive properties of the films in a wide range of tempertures and magnetic fields up to 20 T.

2. To investigate how Mn excess, i.e. increased ratio y=Mn/(Sr+La), influences electric transport and magnetoresistance of $La_{1-x}Sr_xMn_yO_3$ films.

3. To investigate influence of different substrates on low-field and high-field magnetoresistance of $La_{1-x}Sr_xMn_yO_3$ films.

4. To test $La_{1-x}Sr_xMn_yO_3$ film-based sensors for magnetic field dynamics measurement in magnetic pulse forming – welding system.

Scientific novelty. Novelty of this work includes the following findings:

Comprehensive study of magnetoresistive properties of $La_{1-x}Sr_xMnO_3$ manganite films prepared by the pulsed injection MOCVD technique onto glass-ceramics substrates revealed the possibility to tune these properties in a wide range of temperatures and magnetic fields by changing deposition temperature and film thickness. It was obtained that so prepared films have column-like microstructure which determines resistivity, magnetoresistance and its anisotropy of the films. Also it was obtained that films whose thicknesses are less than about 25 nm consist mainly of the amorphous phase, while polycrystalline column- shaped microstructures are typical for the thicker films. It was found that the choice of substrate for deposition of nanostructured $La_{1-x}Sr_xMn_yO_3$ films has a great influence on the low-field (<0.7 T) magnetoresistive properties, while in high fields these properties are affected insignificantly. It was demonstrated that choosing an AT-cut Quartz substrate the low field magnetoresistance increases twice in comparison with polycrystalline Al_2O_3 or amorphous Si/SiO_2-1000 substrates. It was found that the increase of Mn content in nanostructured $La_{1-x}Sr_xMn_yO_3$ films enables to shift metal-insulator transition temperature by 45 degrees and increase magnetoresistance at temperatures higher than room temperature.

Practical value. The obtained results enable to suggest development of fast high pulsed magnetic field sensor based on nanostructured manganite films with Mn-excess, which has low dimensions, increased temperature range of operation, high sensitivity at higher than room temperatures and low anisotropy. Such features allow to use manganite sensor for various applications, including measurements of magnetic field dynamics in electromagnetic forming and welding equipment.

Statements for defence.

1. The metal – insulator transition temperature T_m and temperature of maximal high-field magnetoresistance MR_{max} of nanostructured $La_{1-x}Sr_xMnO_3$ manganite films, deposited by the pulsed injection MOCVD technique onto glass-ceramic substrates, can be tuned along a wide range of temperatures (130 K – 240 K) by adjusting film thickness and deposition temperature during growth while keeping the same chemical composition of the film. For room temperature applications the films with thickness ≈400 nm deposited at 750°C are preferable due to highest magnetoresistance values at this temperature range.

2. The low-field (≈0.7 Tesla) magnetoresistance of nanostructured $La_{1-x}Sr_xMn_yO_3$ films at ferromagnetic phase is significantly increased, when using monocrystalline AT-cut Quartz substrate for film deposition in comparison with films on polycrystalline Al_2O_3 and amorphous Si/SiO_2-1000, due to formation of interdiffusive layer at the film - substrate boundary and growth of higher structural quality crystallite columns separated by thinner grain boundary regions. At paramagnetic phase the influence of substrate's type on low-field magnetoresistance values is negligible, while more significantly affecting magnetoresistance anisotropy due to change in demagnetization field.

3. Change of Mn excess y from 1.05 up to 1.21 in nanostructured $La_{1-x}Sr_xMn_yO_3$ films grown on Al_2O_3 substrate leads to the increase of the metal–insulator transition temperature T_m by at least 45 degrees (from 240 K up to 285 K), what results in the increase of magnetoresistance magnitude at higher than room temperatures.

4. Magnetic field sensors developed using nanostructured $La_{1-x}Sr_xMn_yO_3$ films with Mn excess (y>1.10) grown on polycrystalline Al_2O_3 substrate have such distinctive features, as small dimensions, increased temperature range of operation, high sensitivity at higher than room temperat-

ures and low anisotropy, what allows to use them for the local measurements of magnetic field dynamics during fast electromagnetic forming and welding processes.

Approval of the work results. 4 articles were published on the subject of the dissertation in scientific journals included in Thomson Reuters Web of Science database, 1 article in conference proceedings.

The work was presented at the following conferences:

- 15th XMR-Symposium "Magnetoresistive Sensors and Magnetic Systems", Wetzlar, Germany, March 19-20, 2019. Guest Speaker.
- 7th Euro-Asian pulsed power conference EAPPC & BEAMS 2018, Changsha, China, September 16-20, 2018.
- Collaborative Conference on Materials Research CCMR2017, Jeju, South Korea, June 26-30, 2017.
- 14th Symposium „Magnetoresistive Sensors and Magnetic Systems“, Wetzlar, Germany, March 21-22, 2017.
- 6th Euro-Asian Pulsed Power Conf. / 21th Intern. Conf. on High-Power Particle Beams / 15th International Conference on megagauss magnetic field generation and related topics, Estoril, Portugal, September 18-22, 2016.

Author's Contribution. The results and findings presented in this dissertation were obtained by the author in co-operation with his co-authors of the publications listed in the bibliography. The author performed measurements of resistivity and magnetoresistance in low and high magnetic fields of La-Sr-Mn-O films, performed measurements high induction coils with CMR sensors at Pulsolution GMBH (Switzerland), together with colleagues performed measurements of magnetic field dynamics in Magnetic Pulse Welding (MPW) equipment in Dortmund Technical University (Germany), led designing and fabrication of MPF equipment used for testing of magnetic sensors at the State research institute Center for Physical Sciences and Technology.

Structure of the Dissertation. The dissertation consists of an introduction, 3 main chapters, general conclusions, references, and list of publications. The main chapters include literature review, description of samples preparation and experimental setups, and obtained results.

Chapter 2

Review of Physical Properties of Manganites

2.1 Crystallographic structure

The manganite oxides analyzed in this Thesis are called perovskites, because they have the same type of crystal structure as $\mathrm{CaTiO_3}$, the crystal structure historically named after mineralogist Count Lev Aleksevich von Perovski. The perfect perovskite manganite crystal cell of $\mathrm{LaMnO_3}$ has cubic form with space group $Pm\bar{3}m$ [13]. In such compound Manganese (Mn) ion has an integer valence of +3; the bulk material is antiferromagnetic [14]. Mn, a transition metal, electronic configuration is: $1s^2 2s^2 2p^6 3s^2 3p^6 4s^2 3d^5$. The most important to the electronic and magnetic properties of Manganese oxides is the fact, that Manganese can have different number of valence electrons- up to 7 (two electrons from the 4s orbital and five electrons from the 3d orbital). In technological applications most typical are $\mathrm{Mn^{3+}}$ and $\mathrm{Mn^{4+}}$ states.

Doping the insulating $\mathrm{LaMnO_3}$ material with divalent alkaline-earth ions causes conversion of a number of $\mathrm{Mn^{3+}}$ to equal number of $\mathrm{Mn^{4+}}$ ions and change of Perovskite manganite oxides electronic and magnetic properties [15]. Doped Perovskite manganese oxides are denoted by the formula $\mathrm{R_{1-x}A_xMnO_3}$, where R stands for trivalent rare-earth ion (usually $\mathrm{La^{3+}}$) and A stands for divalent alkaline-earth ions ($\mathrm{Ca^{2+}}$, $\mathrm{Sr^{2+}}$, $\mathrm{Ba^{2+}}$, $\mathrm{Pb^{2+}}$, etc.). The diverse physical properties of charge ordering-disordering, orbital ordering, large magnetic anisotropy and, especially, intrinsic colossal magnetoresistance of these mater-

ials have stimulated broad interests scientific and technological communities around the world.

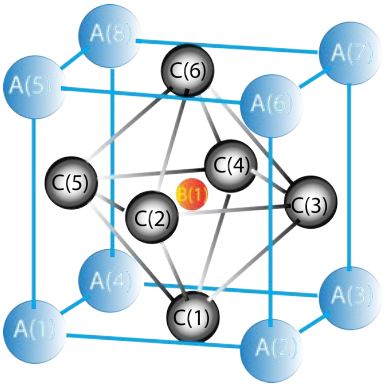

Figure 2.1: Ideal cubic perovskite structure. A site is occupied by La, Sr, Ca while small B cation is a host for Mn. Oxygen takes positions at C sites.

Schematic diagram of perovskite manganite cubic structure is shown in the Figure 1 , where Mn ion is in the center of the lattice, rare earth ions are at the corners of the lattice and oxygen ions are in the centers of each of six walls. Only ideal perovskite $LaMnO_3$ crystal could have cubic lattice, in reality, however, doping ions have different radii and cubic lattice gets distorted into orthorhombic or rhombohedral lattice [16].

Tolerance factor

The level of distortion of the lattice – the deviation of the lattice from the perfect cubic form - is described by Goldschmidt's tolerance factor T [17]. t is a dimensionless number calculated by semiempirical relationship between ionic radii:

$$T = \frac{R_A + R_C}{\sqrt{2}(R_B + R_C)}$$

where R_A, R_B and R_C are the ionic radii of the A-site, B-site, and C-site atoms. For the "ideal" cubic cell T is about 1.00, in general for perovskite cells T can be between about 0.77 and about 1.05. Materials with $T > 1$, usually have high dielectric or ferroelectricmaterial properties, while materials with $T<1$, are often associated with low symmetry. Depending upon atomic substitution (doping), at the room temperature the perovskite structure may have any of about 15 crystallographic structures. Goldschmidt's tolerance factor is used by researchers for development of new perovskite materials [18]. T factor characterizes size mismatch occurring when the R (or A) site ions are too small to

fill the space in the three-dimensional network of MnO_6 octahedra pictured in Fig. 2.2 with doping ions.

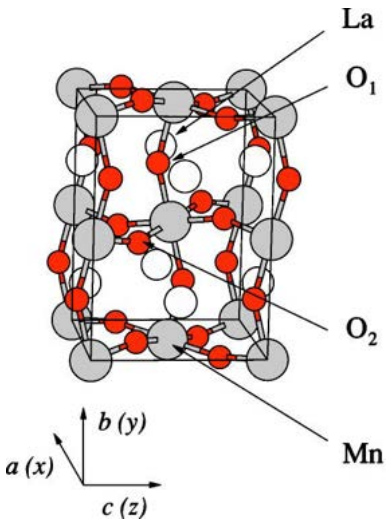

Figure 2.2: Structure of $LaMnO_3$ crystal. The oxygen O_1 ions are characterized by two identical O-Mn bonds, the oxygen ions of the basal plane of the octahedron are labeled as O_2 - they are characterized by two different - long and short - O-Mn bonds [19].

For a perfect size match ($T = 1$), the Mn-O-Mn bond angle would be equal to 180°. For T<1, in addition to contraction of bond distances the octahedra tilt and rotate to reduce the excess space around the R (or A) site and the bond angle will become less than 180°. In other words, the Mn-O-Mn bond angle depends on the average ionic radius of R (or A) site.

2.2 Temperature dependencies

Doped cubic manganites exhibit three characteristic temperatures: the Curie temperature T_C, the resistivity peak temperature T_P, and T_{MI} at which the metal-insulator transition (MIT) occurs [20].

Curie temperature T_C is a temperature at which magnetic materials undergo a sharp change in their magnetic properties; manganites at T_C change from ferromagnetic (FM) metal at low temperatures to a paramagnetic (PM) insulator at high temperatures.

Temperature profile of manganite resistivity (ρ vs T) exhibits a sharp maximum at a T_ρ, above which exhibits a semiconductor-like temperature dependence ($d\rho/dT<0$) (see Fig. 2.3).

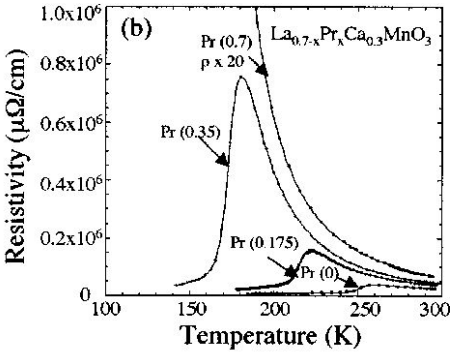

Figure 2.3: Resistivity measurements of bulk ceramic samples [21].

Experimental measurements show that that T_P usually is very close to T_C. As T_P is usually treated as being identical to T_{MI}, upon heating, the MIT and FM-to-PM transitions seem to occur simultaneously.

T_C of perovskite manganite materials correlate with Goldschmidt's tolerance factor T: maximum T_C, which is interesting for technological applications, occurs around $T = 0.93$. T_C also is linked to crystal system (Rhombohedral or Orthorhombic) and mean Mn-O-Mn bond angle see table 2.1(mean Mn-O-Mn bond angle is represented by local oxygen displacement). T_C is highest for manganites with Rhombohedral crystal system and high tolerance factor.

Table 2.1: T_C dependence on $\mathrm{La_{0.72-x}R_xA_{0.3}MnO_3}$ structural characteristics. Mn-O-Mn bond angle is expressed as local oxygen displacement $Q = \sqrt{\langle R_A\rangle^2 - \langle R_A^2\rangle}$ [21].

Composition	**Structure**	T	$\mathbf{T_C(K)}$	**Q (Å)**
$\mathrm{La_{0.7}Sr_{0.3}MnO_3}$	Rhombohedral	0.936	352	0.0431
$\mathrm{La_{0.525}Pr_{0.175}Sr_{0.3}MnO_3}$	Rhombohedral	0.933	330	0.0498
$\mathrm{La_{0.35}Pr_{0.35}Sr_{0.3}MnO_3}$	Rhombohedral	0.931	320	0.0527
$\mathrm{Pr_{0.7}Sr_{0.3}MnO_3}$	Orthorhombic	0.926	260	0.0600
$\mathrm{La_{0.7}Ca_{0.3}MnO_3}$	Orthorhombic	0.922	255	0.0226
$\mathrm{Pr_{0.7}Ca_{0.3}MnO_3}$	Orthorhombic	0.912	...	0.0005

There is also a certain T value, at which the crystal changes the phase from

O'-orthorhombic ($\mathrm{c/a} < \sqrt{2}$) phase to an O-orthorhombic ($\mathrm{c/a} > \sqrt{2}$). This change of the phase influences resistivity depencence on temperature of the material: for material in the O'-orthorhombic phase the resistivity decreases continuously with rise of temperature (without clearly expressed T_P, see plotted line for $\mathrm{Pr_{0.7}Ca_{0.3}MnO_3}$ in Fig. 2.2) through T_C for $\mathrm{Pr_{0.7}Ca_{0.3}MnO_3}$, which is in the O'-orthorhombic phase.

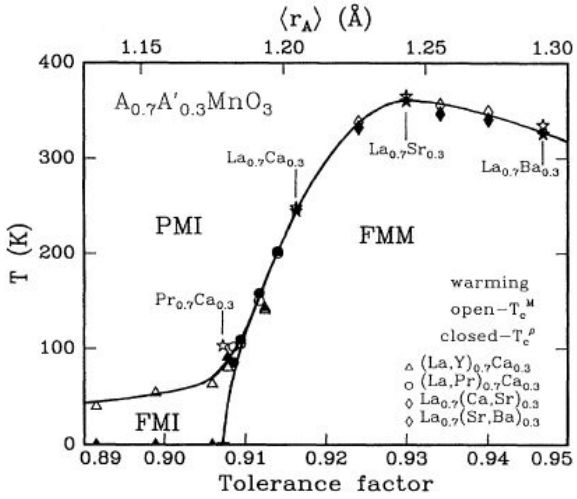

Figure 2.4: Phase diagram of perovskite manganites. The switching to ferromagnetism $\mathrm{T_C^M}$ is defined by minimum in $d(M/H)/dT$ (open symbols); it correlates well with resistivity maximum $\mathrm{T_C^\rho}$ (patterned symbols) [16, 22].

The detailed investigation done by Schiffer et al. [23] and Hwang et al. [16, 22] shows that with change of the material in tolerance factor there is a change in switching between magnetic and electric regimes of doped perovskite manganites: from a paramagnetic insulator at high-temperature to a low- temperature ferromagnetic metal at large tolerance factor, and to a low-temperature charge-ordered ferromagnetic insulator at small tolerance factor. The change is plotted as a phase diagram in the Fig. 2.4.

Observed Curie temperature for thin films often significantly deviates from T_C of the bulk materials. May be, the Curie temperature is thickness dependent: the T_C shifts to lower temperatures compared to the bulk when the spin–spin correlation length exceeds the film thickness [24].

2.3 Jahn-Teller effect and band structure

Any configuration of atoms or ions, in which there is a degenerate ground state is unstable and is inclined to adjust to the configuration with lower symmetry when this lower symmetry configuration removes degeneracy at the same reducing overall energy level of the system. The range of phenomena arising from degeneracy are called Jahn-Teller effect [25]. Analyzing Jahn-Teller effect for a crystal impurity center, it can be assumed, that the ground state (as defined by Hund's rules) of symmetric phase is two fold degenerate. The lowering of the symmetry causes deformation δ of the surrounding structure, splitting of electronic levels and decrease elastic energy by the value $\sim \delta^2$. The symmetric configuration is always unstable because of degeneracy; degeneracy is eliminated by lowering the symmetry of the crystal structure. The physical mechanism of these processes is in the link between electrons in degenerate level and deformation of the surroundings.

In simplified way, the energy of the system can be written as:

$$E(\delta) = \frac{C}{2}\delta^2 \pm g\delta \tag{2.1}$$

where δ is a measure of the deformation, C is the modulus of elasticity, g is the measure of the interaction of the electronic subsystem with environment deformation δ. The second term in $g\delta$ in equation 2.1 defines the change of electronic level energy. The equilibrium configuration of the system is at $\delta_{\pm} = \pm g/C$, which is found minimizing 2.1. In absence of distortions (δ=0) the nuclear wave function can be written as

$$\Phi_{1,2}(R, r) = \phi(R)\psi_{1,2}(r) \tag{2.2}$$

where $\psi_{1,2}(r)$ is the electronic wave function - superposition of two degenerate states and $\phi(R)$ is the nuclear wave function.

The electron- lattice interaction deforms the lattice by $\delta_{\pm} = \pm g/C$ and removes degeneracy. Figure 2.5 shows δ dependence for deformations: the energy minimums correspond to the vibron functions Φ_1 and Φ_2, the exited states and $\phi_1\psi_{21}$ correspond to energy $\overline{E}$. The Jahn-Teller energy $E_{JT} = -\frac{g^2}{2C}$.

The electronic configuration of Mn atom is $1s^2 2s^2 2p^6 3s^2 3p^6 3d^5 4s^2$; the d-shell is incomplete [26] and 3d electron level has five-fold orbital degeneracy. When bound in the $R_{1-x}A_xMnO_3$ lattice, Mn ions are in octahedral coordination, and the five-fold orbital degeneracy of the 3d levels of Mn is split by the octahedral

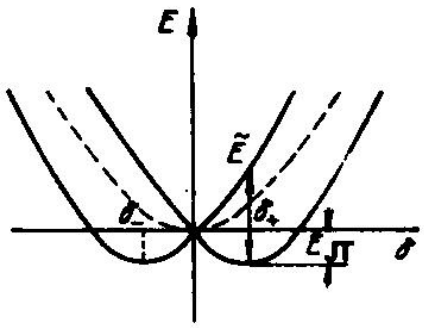

Figure 2.5: Schematic representation of the relation between deformation and energy for twofold degeneracy. E_{JT} is the decrease in energy level due to Jahn-Teller effect.

crystal field into the lower-lying triply degenerate t_{2g} states and the higherlying doubly degenerate e_g states (see figure 2.6).

According to the Hund's first rule (defining that total spin angular momentum for all electrons S is to be maximized) the d-electrons have the same spin orientation. An Mn^{3+} ion has an electronic configuration $3d^4$ with three electrons at the t_{2g} levels and one electron at the e_g level (S =2). A Mn^{4+} ion with the $3d^3$ electron configuration has three t_{2g} electrons and no electron at the e_g level (S = 3/2). The degeneracy of the t_{2g} and e_g levels are further removed by the Jahn–Teller distortion: a crystal field with symmetry lower than octahedral (which takes place, for example, when the oxygen octahedron is axially elongated) lifts the degeneracy of the t_{2g} and e_g levels, as shown on the right side of figure 2.6 . The energy of the Mn^{4+} ion with no e_g electrons does not change, while the energy of Mn^{3+} ion with e_g occupied state decreases due to the Jahn–Teller effect caused distortion at a cost of the lattice energy. Owing to the fact, that Mn^{3+} ions have a great tendency to the Jahn–Teller distortion of their octahedral environment, in the manganites with high concentration of Mn^{3+} ions cooperative Jahn–Teller distortions take placel, which leads to decrease of the lattice symmetry. For example, the $LaMnO_3$ compound with Mn^{3+} has the orthorhombically distorted perovskite lattice.

LSMO band structure

The band structure of perovskite manganites depends on A site (see Figure 2.1) substitution. which causes various structural distortion. For example, A-site cations smaller than La ion reduce Mn-O-Mn bond angle in the Mn-O octahedral matrix; this influences band gap and electron affinity, as was shown by

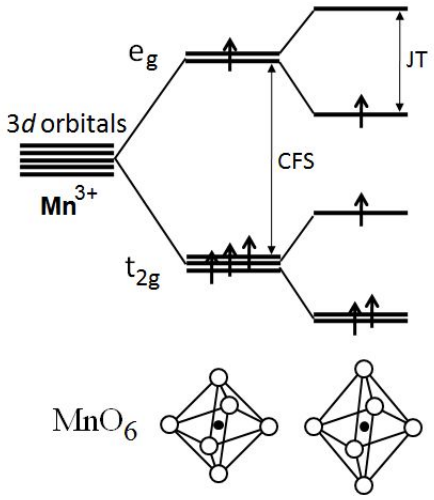

Figure 2.6: Crystal-field splitting of the five-fold degenerate atomic 3d levels into lower triply degenerate t_{2g} and higher doubly degenerate e_g levels (split in the middle). The Jahn–Teller (JT) distortion of the MnO_6 octahedron further lifts each degeneracy. Splitting of the t_{2g} and e_g levels and distortion of the MnO_6 octahedron caused by Jahn– Teller effect is shown on the right side [26].

Lee et al. [27] (see the table 2.2) for $La_{0.7}Sr_{0.3}MnO_3$, $La_{0.6}Gd_{0.1}Sr_{0.3}MnO_3$ and $La_{0.4}Gd_{0.3}Sr_{0.3}MnO_3$, where part of La ions (atomic covalent radii 139 pm) are substituted by smaller Gd ions(atomic covalent radii 132 pm). The decreased bond angle leads to band narrowing and band gap widening. Also, in contrast to ferromagnetic metals, where spin-up and spin-down bands are both occupied, in FM phase of manganites, these bands are separated by 1eV or more. The upper band is empty; this leads to a half-metallic behavior with conduction band of the ferromagnet being fully polarized [5]. The band structure of LSMO is shown in figure 2.7.

Table 2.2: Measured band structure of $La_{0.7}Sr0.3MnO_3$, $La_{0.6}Gd_{0.1}Sr0.3MnO_3$ and $La_{0.4}Gd_{0.3}Sr0.3MnO_3$ films [27]. E_G - band gap, E_{EA} - electron affinity.

Compound	E_G	E_{EA}
$La_{0.7}Sr0.3MnO_3$	0.63 eV	4.46 eV
$La_{0.6}Gd_{0.1}Sr0.3MnO_3$	0.82 eV	4.37 eV
$La_{0.4}Gd_{0.3}Sr0.3MnO_3$	0.95 eV	4.26 eV

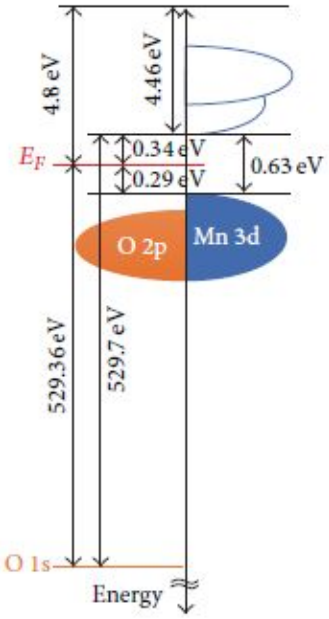

Figure 2.7: LSMO band structure [27].

Magnetic polarons Magnetic polarons are magnetic nano systems of electrons and ions in diluted magnetic semiconductors, formed by exchange interaction of a carrier (ion) spin with spins of localized electrons. The result is ferromagnetic alignment of the spins of localized electrons in vicinity of the carrier and can be treated as a magnetic molecule with large magnetic moment [28]. The evidence of conduction by polarons in paramagentic regime (aboveT_C) in doped LMO manganites $(La_{1-x}A_x)_{2/3}Ca_{1/3}MnO_3$ (with A standing for Y or Tb) have been first proven by Teresa et al [29]. Their experiments have shown spontaneous formation of small (approximately 12 $\AA$) magnetic clusters above T_C. Upon application of magnetic field these clusters clusters decreased in number while grow in size.

2.4 Charge transfer mechanisms

Charge transfer in perovskite manganites is very complex, there are four types of charge transfer mechanisms for perovskite manganites described in scientific literature: percolation, coulomb, super-exchange and double exchange.

Superexchange and Double exchange

Super exchange and double exchange charge transfer mechanisms have been proposed by C. Zener in 1951. Although these mechanisms have similarities, there are also significant differences.

Superexchange spin coupling mechanism first time have been suggested by Anderson [30–32] as mechanism of coupling between two magnetic Mn^{2+} ions with one d-state electron on each, separated by an O^{2-} ion with two electrons in p state. It was emphasized, that the p-state electrons from O^{2-} ion can transfer into an s or d-state electron on Mn^{2+} ion; such transfer is much more likely with ions on opposite sides of O^{2-} ion, making superexchange with Mn-O-Mn bond angle of 180° much more likely than with 90° angle. For superexchange to happen two Mn atoms with the same valence (number of electrons) shall have antiferromagnetic alignment of spins.

Double exchange. In it's original definition with Na-Cl-Na example, double exchange is described by Zener ([33]) in the example of electron transfer from one Na^{+} ion to the next closest Na^{+} ion as the transfer of an electron from the left Na^{+} ion to the central Cl^{-} ion with simultaneous transfer of an electron from the central Cl^{-} ion to the right Na^{+} ion. In Mn-O-Mn case, the electron is transferred from Mn^{3+} ion to Mn^{4+} ion via central O^{2-} ion. This double exchange occurs only when the spins of Mn ions respective d-shells point in the same direction; such mechanism at the same time leads to electrical conduction and to ferromagnetism.

Applying semiclassical approximations to the Zener model (treating classically Mn core (t_{2g}) electrons and quantumm mechanically - mobile e_g electrons) Anderson and Hasegawa [34] separated the case J»b, where b is the transfer integral for the transfer of single electron from one Mn ion to another without change of spin and J is intra-atomic exchange integral. They have found that the transfer integral between two ions depends on $\cos(\theta)/2$, where θ is the angle between the spins of two Mn ions.

Percolation

CMR perovskite manganites materials demonstrate an insulator–metal transition from a high-temperature insulating phase to a low-temperature metallic phase. This transition takes place in around a peak region at T_P in the resistivity versus temperature curve. Along with this phase transition, at the Curie temperature T_C, occurs a magnetic transition from a high-temperature paramagnetic phase to a low-temperature ferromagnetic (FM) phase. In half-metallic band structure electrons can propagate only within boundaries of magnetic domains with magnetization parallel to the electron spin [35]. Percola-

tion threshold of magnetic domains takes place at metal–insulator transition temperature; T_C majority and minority carriers percolate leading to a drastic decrease in resistivity [1]. This transition have been recorded with magnetic force microscope [36] providing direct observation of the formation of percolative networks the samples while cooling and disappearing of these networks when warming.

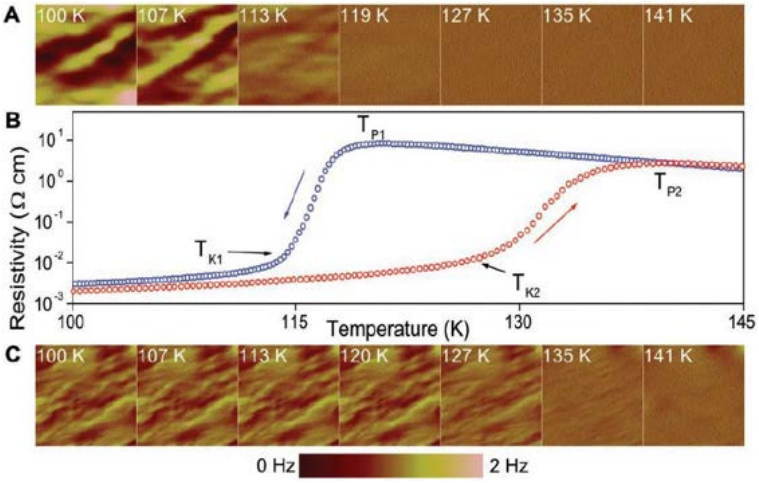

Figure 2.8: The temperature- dependent MFM image sequence (A) for cooling and (C) for warming, and the resistivity (B) of the $La_{0.33}Pr_{0.34}Ca_{0.33}MnO_3$ thin film over a thermal cycle. The blue series represent cooling and the red series represent warming. Scanned areas are 6 μm by 6 μm for all cooling images and 7.5 μm by 7.5 μm for all warming images [36].

Magnetoresistance

Magnetoresistance MR is defined as change in resistance of a material at application of magnetic field [37]:

$$MR = \frac{R(B) - R(0)}{R(0)} \times 100\% \tag{2.3}$$

where $R(0)$ is resistance at 0 magnetic flux density, B is magnetic flux density and $R(B)$ is resistance at magnetic flux density with strength of B. Manganites exhibit negative magnetoresistance.

Resistivity and CMR

In the paramagnetic phase the electrical resistivity of manganites with strong double exchange exhibits strong temperatue dependece. The most widely used

$\rho(T)$ laws to fit experimental data are simple thermal activation law; hoping of adiabatic polarons and Mott variable range hopping (VRH) model $\rho = \rho_\infty exp[(T_0/T)^{1/4}]$. The VRH model is based on the localization of he charge carriers by the magnetic disorder [5, 38]. At low temperatures the spontaneous alignment of Mn spins below Curie temperature allows delocalizationof the e_g electrons, resulting in low resistivity FM phase. The alignment of Mn spins can be induced at $T >= T_C$ and reinforced at $T <= T_C$ by external magnetic field. These manganites have large negative magnetoresitance (colossal magnetoresitance, CMR) with peak around T_C. One of the highest CMR ratios $R(0)/R(6T) > 10_3$ was reported by Jin et. al. in for a thin film of $La_{0.67}Ca_{0.33}MnO_3$ with $T_C \approx 80K$ [39]. The temperature, where the colossal magnetoresistance (CMR) response of manganites is at it's maximum is denoted by T_M [40].

2.5 Epitaxial vs polycrystaline

Soon after the interest in the perovskite manganites was renewed a negative magnetoresistance was observed in polycrystalline manganites films, [41, 42] as well as in artificial grain boundary structures of manganites [43, 44] induced when the film was grown on bicrystal substrate. The size and proportions of the vertical nanostructures play a critical role in defining the properties of manganite thin films through the vertical interfacial and grain boundary effects.

There are huge differences in resistance and magnetoresitance of epitaxial and polycrystalline LSMO films [45] (Fig. 2.9). If produced with the same composition, the resistivity ρ of polycrystalline films is much higher than for epitaxial LSMO films (by about an order of magnitude) caused primarily by scattering in disordered structures of grain boundaries. The polycrystalline films exhibit much larger drop in resistance at the same applied magnetic field ($MR \sim 15\%$). Anisotropy of $\rho(H)$ ($\Delta\rho$ for parallel $I \parallel H$ and perpendicular $I \perp H$ current directions) is small for polycrystalline films compared to $\rho(H)$ for epitaxial films. This implies that the mechanism of anisotropic magnetoresistance (AMR) is not significant in polycrystalline films.

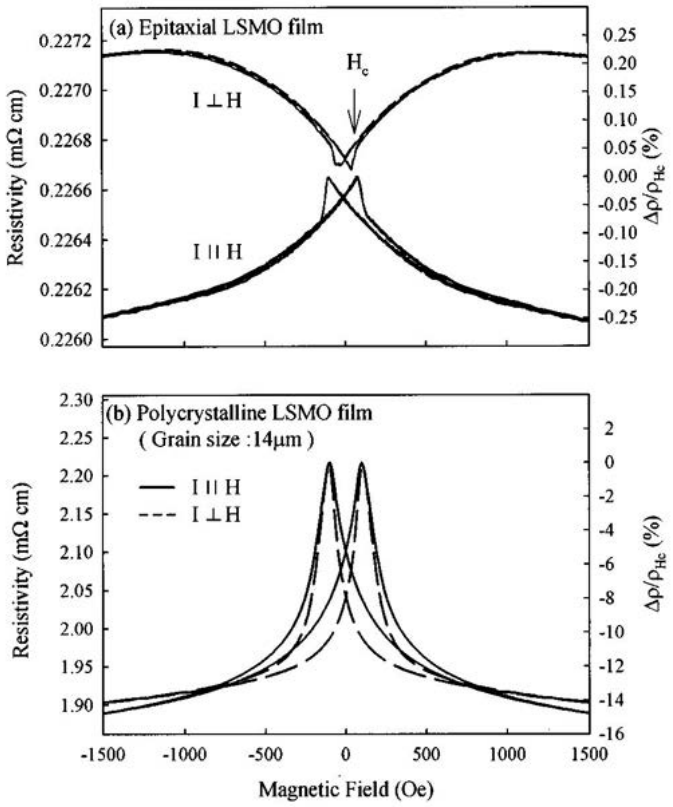

Figure 2.9: Resistivity as a function of magnetic field H,measured at 4.2 K, for epitaxial LSMO film (a) and polycrystalline LSMO films with 14 mm average grain size(b) [45]. The MR data are displayed as $\Delta\rho/\rho = [\rho(H) - \rho(H_C)]/\rho(H_C)$.

2.6 Methods for growing polycrystaline manganite films

There are several distinctive methods for growing polycrystalline manganite films. These methods differ in their technological complexity hence the cost and result in different polycrystalline structure.

Probably the earliest method was growing of manganite films was using pulsed laser deposition [41]. Thin films with thickness of about 1000 $\mathring{A}$, were grown on (100)-oriented single-crystal and polycrystalline $SrTiO_3$ substrates from

manganite targets with subsequent postannealing of the films in O_2 atmosphere to reduce the resistivity and raise the T_C to values close to room temperature [46]. This have resulted in the LCMO film replicating polycrystalline nature of the underlying substrate with an average grain size of about 3 μm. Epitaxial LSMO grains have grown on individual $SrTiO_3$ grains with grain boundaries between them (Fig. 2.10).

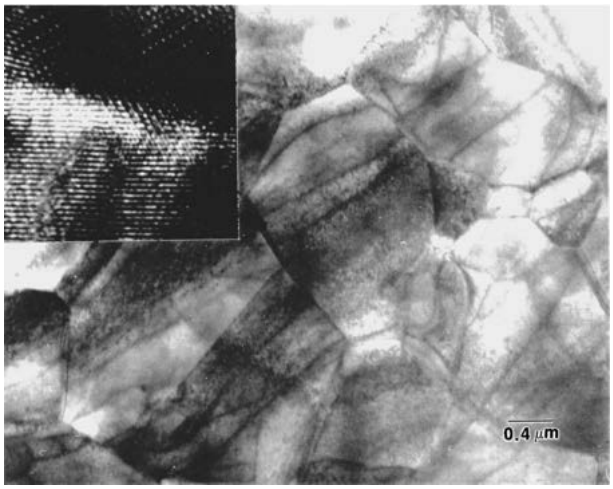

Figure 2.10: TEM image of the plan-view to the LCMO film grown on 3 μm average grain-size polycrystalline $SrTiO_3$ substrate shows a well-defined grain morphology reflecting the underlying grain structure of the substrate. The inset shows high-resolution TEM image of a grain-boundary region [41].

The most technologically complicated method for growing nanostructured manganites is growing thin film with vertical nanorods by high magnetic field assisted pulsed laser deposition. A high magnetic field assisted pulsed laser deposition (HMF-PLD) system have been used for in-situ growth of thin films under a high (up to 10 Tesla) homogenious magnetic field [47] (Fig.2.11). For the LCMO films grown under different magnetic fields, when the applied magnetic field was higher than a critical value, the vertically aligned nanorod structures have deloped starting from the applied critical magnetic field of 4–5 T. Above 5 T, vertically aligned nanorod structures were formed and the dimension size of the nanorods was gradually reduced with further increasing the magnetic field.

For further discussion it is important to note, that the formation of nanorods, which in turn affects conductivity of the film, depends on the strength of the

magnetic field applied during deposition. Growth at in the absence of the magnetic field have resulted in continuous planar 220 nm thick film (see fig 2.12. At 4 Tesla magnetic field, the film grows thicker (about 320 nm) with transitional morfological structure structure. At 5 Tesla magnetic field the film shows vertically aligned nanorod structures with an average dimension size of 50 nm. Differently, the film grown at 8 Tesla shows a two-layer structure: a continuous thin planar epitaxial layer about 30 nm thick adjacent to the substrate, and above it - a nanorod layer with a uniformly sized about 480 nm height rods.

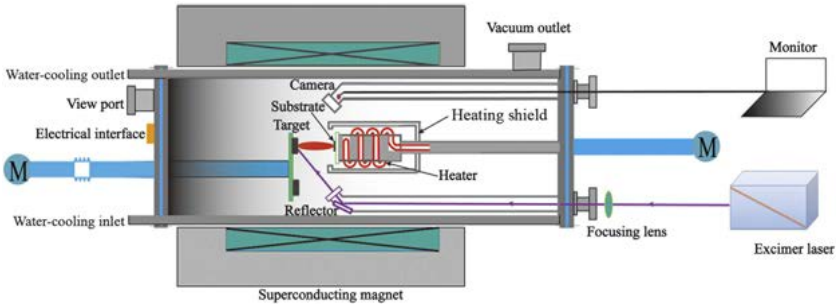

Figure 2.11: Schematic illustration of the high magnetic field assisted pulsed laser deposition system [47].

Another interesting method for growing LSMO nanostructures has been described by Chong el al [48]. First, the high-density array of Si nano tips was made from an n-type Si wafer using the electron cyclotron resonance (ECR) plasma-enhanced chemical vapor deposition technique [49]. The wafers with nano tip structures were used as a templates for depositing the $La_{0.7}Sr_{0.3}MnO_3$ (LSMO) rods with pulsed laser as shown in Fig. 2.13(a). The deposition conditions are at $725°C$ for 20 min under 50 mTorr oxygen pressure, followed by an in situ annealing at $400°C$ for 30 min. The resulting polycrystalline LSMO-coated Si nano tips form vertically aligned, highly dense and uniform morphology with the average rod diameter abound 40 nm and the height of about 100 nm.

Metal organic chemical vapour deposition (MOCVD) technique is used for thin film epitaxial and polycrystalline LSMO film growth [50, 51]. The principal scheme of the MOCVD reactor is shown in Fig.3.1. During deposition, the injectors inject microdoses (of a few microlitres) of an organic solution containing a dissolved mixture of organometallic precursors into heated reactor chamber. After flash evaporation of the injected organic solution with precursors, the vapour mixes with mixture of Ar and O_2 gas and is transported to

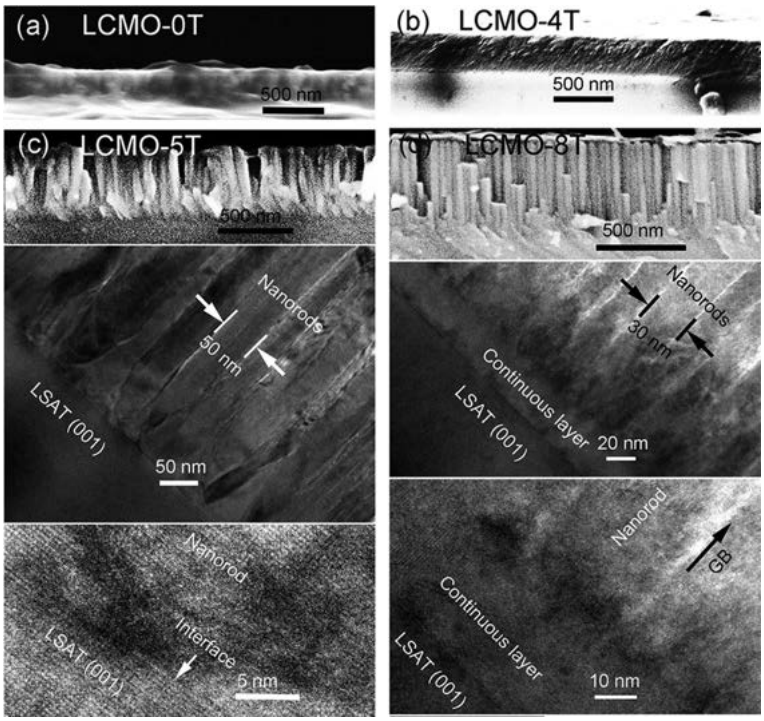

Figure 2.12: (a) Cross-sectional FESEM image of the LCMO-0T film; (b) the cross-sectional FESEM image of the LCMO-4T film; the cross-sectional FESEM, TEM and high resolution TEM images of (c) the LCMO-5T and (d) LCMO-8T films, respectively [47].

the heated substrate and deposited in the form of thin film. The thickness of the obtained films ranges from 4 nm up to few hundred nm. After deposition the films are cooled to room temperature in oxygen atmosphere.

Deposition of polycrystalline manganite thin films can be done by sol-gel technique [26]. The obtained layers are usually polycrystalline with the magneto-transport properties dominated by tunneling of spin-polarized carriers between grain boundaries and showing strong grain size dependence [52].

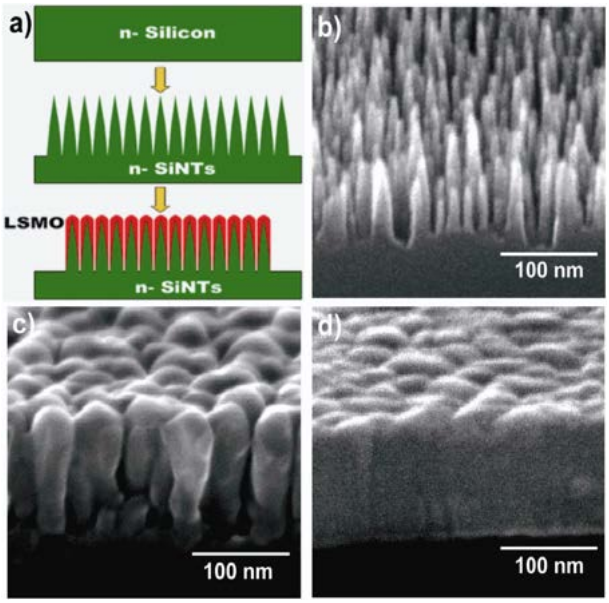

Figure 2.13: Process of fabrication of the LSMO/SiNTs heterojunction (a). SEM images of the uncoated Si nanotip array (b) and LSMO-coated Si nanotips(c). For comparison, SEM image of LSMO film grown on planar Si wafer is shown in (d) [49].

2.7 Charge transfer mechanisms in polycrystalline manganite films

Percolation

The phase diagram is not homogeneous even through single Mn oxides crystals [53–55], and it cannot be homogeneous through the films of polycrystalline manganites. For such materials where phase separation between Ferromagentic, antiferromagnetic, Insulator regions exist, the resistivity behaviour can be explained with percolation theory [55].The effective resistance of the film can be understood as the result of percolative network. The CMR effest can be explained as magnetic field aligning of spins of Mn ions and expanding number and size of ferromagnetic regions thus resulting in decreased resistivity of the bulk material. The percolation magnetoresistance theory can be extended for description conductivity of the films constructed of nanorods. As can be seen form Fig. 2.15, if nanorods are stemming from the substrate, in the absence of

magnetic field, they can be represented as network of resistors (nanorods and grain boundaries). If there is a continuous shunt layer directly on the substrate, it reduces the quality of the CMR phenomena of the LSMO material.

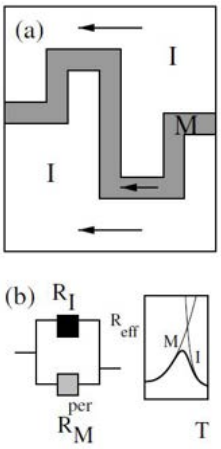

Figure 2.14: (a) Behaviour of Mixed-phase state material near percolation. Arrows indicate conduction through insulating or metallic regions depending on T . (b) Two-resistors model for Mn oxides, where effective resistance R_{Eff} vs T (schematic) arises from the parallel connection of metallic (percolative) R_{Per} M and insulating R_I resistances. [55]

Tunneling through isolating layer

The tunneling through isolating layer was originally discovered in 1975 by Michel Jullière (University of Rennes, France) [56] in Fe/Ge-O/Co-junctions at 4.2 K. He experimented with electrodes having parallel and antiparallel magnetizations and has found, that up to 14% of the conductance attributed to tunelling through the oxide layer is related to the spin polarizations of the conduction electrons. Later Stearns has provided theoretical explanation, linking electron spin-polarization and their proportionality to bulk moments to the fact that these electrons are itinerant d-like electrons" [57].

Later Maekawa and Gafvert [58] have shown, that in the Ferromagnetic metals the tunneling resistance depends on the magnetization process and that the tunneling probability depends on the spin-dependent densities of states in electrodes. Relative conductance through the barrier can be defined as:

$$\frac{\Delta G}{G} = \frac{2(G_{\uparrow\uparrow} - G_{\uparrow\downarrow})}{G_{\uparrow\uparrow} + G_{\uparrow\downarrow}} \tag{2.4}$$

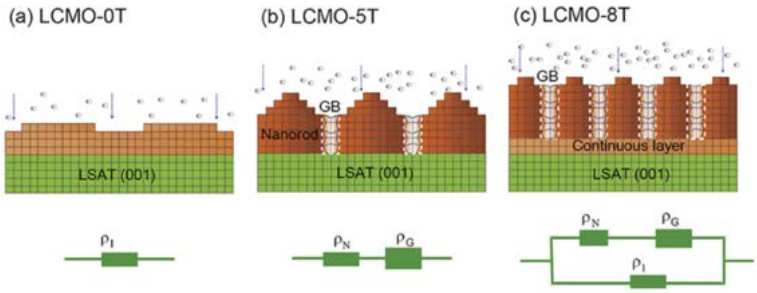

Figure 2.15: Schematic representation of different nanostructures in the LCMO thin films deposited under different high magnetic fields and a corresponding circuit approximation model. (a) The LCMO-0T planar film structure, (b) the LCMO-5T nanorod structure, (c) the LCMO-8T two-layer film structure. The red and brown colors represent LCMO planar film and nanorod, the gradient coloured parts represent grain boundary between the nanorods [49].

where $G_{\uparrow\uparrow} = \alpha(\rho_+^A\rho_+^B + \rho_-^A\rho_-^B)$ is conductance at 0 bias voaltage when magnetic moments of two ferromagnetic electrodes A and B are parallel and $G_{\uparrow\downarrow} = \alpha(\rho_+^A\rho_-^B + \rho_-^A\rho_+^B)$ is conductance at 0 bias voltage when magnetic moments of the electrodes A and B are antiparallel. $\rho_+^{A,B}$ and $\rho_-^{A,B}$ are the tunneling densities of states of the majority and minority spin electrons of metal electrodes A(or B) at the Fermi surface. Maekawa has also shown, that the hysteresis tunnel junctions is sensitive to temperature; it is observed only below 4.2 K. Later developments have shown, that Julliere model shall be expanded to include other phenomena.

In 1994 Myazaki and Tezuka [59] have reported a giant magnetoresistance ratio of 30% at 4.2 K and 18% at 300 K in an Fe/Al_20_3/Fe junction, originating from magnetic tunneling. They have expanded Maekawa and Gafvert theory of tunneling mechanism and have shown, that tunneling conductivity depends on the angle Θ of magnetizations of electrodes as $G = G_0(1 + \epsilon cos\Theta)$ and temperature. Their work have experimentally proven Slonczewski [60] back in 1999 made theoretical predictions. Their work has matched, what Qi et al. havepointed out - namely that Julliere model shall also take into account product of Fermi wave vectors of two electrodes [61].

Glazman and Matveev have developed a theory, that grain boundaries of manganites exhibit multi-step tunneling [62] and there is a significant inelastic tunneling current via localized defect states within the grain boundary barrier. Spin polarization may be not conserved in the inelastic channel so the inelastic tunneling current does not contribute to the magnetoresistance. So, Julliere

two-current model, which assumes that the two spin species of electrons tunnel elastically, is to be extended and a three-current model shall be introduced to account for the inelastic, spin-independent tunneling current.

The three current model of the grain boundary tunneling magnetoresistance in manganites [63]then includes dependencies on bias voltage and temperature:

$$\frac{\Delta R}{R}(V,T) = \frac{I^e_{ap}}{I^e_{ap} + I^i}(V,T)\left(\frac{I^e_p}{I^e_{ap}} - 1\right) \tag{2.5}$$

where $\Delta R/R = (R_{\uparrow\uparrow} - R_{\uparrow\downarrow})/R_{\uparrow\uparrow}$, "$ap$" denotes "antiparallel", "p" denotes "parallel, "e" denotes "eleastic" and "i" denotes "inelastic". The term $\left(\frac{I^e_p}{I^e_{ap}} - 1\right)$ in equation 2.5 represents $\frac{\Delta R}{R}$ from Julliere model.

Direct tunelling

Inoue and Maekawa have shown, that the origin of the magnetoresistance in granular magnetoresistive films can be explained in terms of the tunneling matrix element dependence on the relative orientation of magnetic moments of grains[64]. The conductance of the grain boundary is given as

$$G = G_0\left(1 + P^2 m^2\right) e^{-2\sqrt{2\kappa C/kT}} \tag{2.6}$$

where

$$P = \frac{D_\uparrow - D_\downarrow}{D_\uparrow + D_\downarrow} \tag{2.7}$$

and

$$\kappa = \sqrt{2m^*(V - E_F)/\hbar^2} \tag{2.8}$$

Here G_0 is conductance at 0 magnetic field, $D_\uparrow$ and $D_\downarrow$ are densities of states at Fermi energy E_F for electrons with spins up and spins down, and s, m_*, and V are, respectively, the thickness of the barrier, the effective mass of electrons, and barrier height. The tunneling through FM/I/FM junctions occurs via paths that have largest exponential factor.

Mott model Mott variable-range hopping model, used to describe carrier transport in a disordered semiconductor or in amorphous solids [65] is a suitable model to describe magnetoresistive effects in perovskite manganites [66]. Conductivity then is described by:

$$\sigma = e^2 R^2 \nu_{Ph} N(E_F) \exp\left(-2R/L - W/k_B T\right) \tag{2.9}$$

where R is the mean hopping distance, L is the radius of the carrier localization, and W the splitting between energy levels related to a hopping process. $\nu_{Ph} = 10^{13}$ Hz is the phonon frequency and $N(E_F) = (m^*/\hbar^2\pi^2 n)^{1/3}$ is density of states, approximated by the free electron model [66]. n is the carrier concentration per chemical unit cell; it depends on the doping ratio with. m^* is the effective carrier mass.

2.8 Anisotropy of polycrystalline LSMO films

The response of the sensor to magnetic induction depending on sensor orientation in the magnetic field - anisotropy - is one of the key contributors to magnetic field sensor measurement error. The Magnetoresistance Anisotropy MRA is defined as

$$MRA = \frac{MR_{\parallel} - MR_{\perp}}{MR_{\parallel}} \times 100\% \tag{2.10}$$

where $MR_{\parallel}$ is magnetoresistance of the sensor (or the film sample) with magnetic flux density B parallel to the film plane and $MR_{\perp}$ is magnetoresistance B perpendicular to the film plane.

In low magnetic field MRA of LSMO films can reach from 7% to 31% (see difference between $MR_{\parallel}$ and $MR_{\perp}$ values in Fig. 2.16), but in high magnetic field the MRA falls to about 3% [3].

Belevtsev et al. have indicated two main sources of MR anisotropy in ferromagnetic films, namely: (1) the existence of preferential directions of magnetization (due to strains stemming from the lattice film–substrate mismatch or other sources), and (2) dependence of resistance on the angle between current and magnetization. As the resistivity ρ of manganites in the ferromagnetic state is a function of magnetization, the conductivity increases with enhancement of ferromagnetic order resulting in the huge negative MR in manganites. The magnitude of the MR depends on the ability of the external magnetic field to increase the magnetization. In good crystals at low temperature ($T \ll T_C$) almost all spins are already aligned by the exchange interaction so the ability to increase the magnetization by the magnetic field is minimal [67]. In polycrystalline manganites crystallites represent "good crystals", the rest is disordered grain boundary material.

Parallell and perpendicular to the magnetic field magnetoresistance of polycrystalline films approximation with Brillouin function have confirmed, that

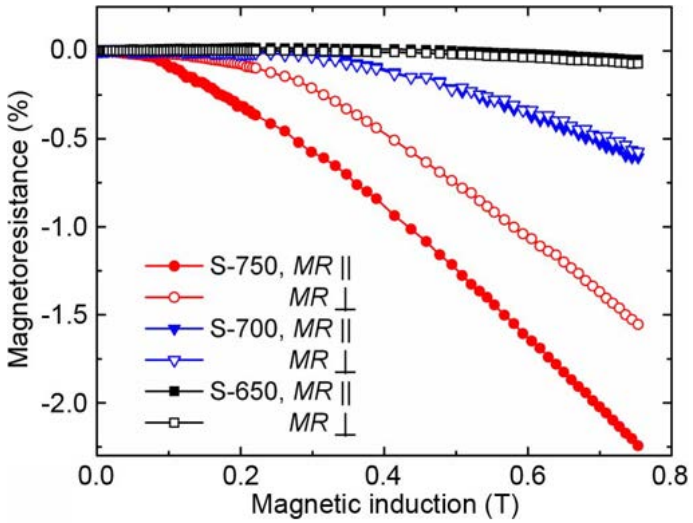

Figure 2.16: Magnetoresistance of the LSMO films at parallel ($MR_{\parallel}$) and perpendicular ($MR_{\perp}$) orientation in the magnetic field. Films were grown at 650°C, 700°C and 750°C deposition temperatures [3].

MRA at low magnetic fields is mostly related to the magnitude of the demagnetization field caused by the geometry while MRA in high magnetic fields is mostly attributed to magnetisation of grain boundaries [68].

***MRA* and the error of the Magnetic Flux Density measurement**

The relation between the MRA of the sensor film and the error of the measured Magnetic Flux Density error has been investigated by Žurauskienė et al. [3]; the results of the investigation are summarized in the Figure 2.17.

Due to anisotropy MRA of the LSMO film sample, the drop of the voltage on the ballast resistor (which is connected in series with the LSMO film sample, see the Figure 3.7) is the same for the range of values of magnetic flux density B - maximum value B_{max} when LSMO film sample is placed in $B \perp$ configuration (see the Figure 3.6) and minimum B_{min} value when LSMO film sample is placed in $B \parallel$ orientation. Then the relative error of the B value calculated from LSMO film sample response

$$\delta = \frac{\Delta B}{B_{av}} \times 100\% \tag{2.11}$$

where $B_{av} = (B_{\parallel} + B\perp)/2$ and $\Delta B = |B_{\perp} - B_{\parallel}|$. Then at room temperature in

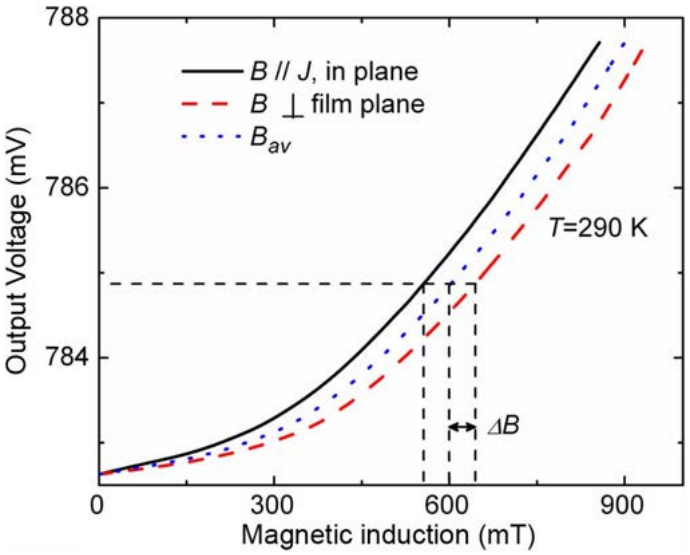

Figure 2.17: LSMO film sample response to magnetic flux density when magnetic field was applied in film plane ($B \parallel$ to the current J) and perpendicular to the LSMO film sample plane ($B \perp$) and average of the $B \parallel$ and $B \perp$ values B_{AV} at the same level of the output voltage [3].

magnetic field above 0.5 Tesla relative error of the polycrystalline LSMO sensor is $\leqslant 10\%$ [3].

2.9 Magnetic Pulse Welding

Magnetic Pulse Welding (MPW) has been chosen for the practical application of LSMO thin films, because MPW process is based on high (in the range of 20 - 40 Tesla) pulsed magnetic fields.

Magnetic Pulse Welding is a collision welding process, which uses a high velocity impact to join two metals. This method allows for the joining of similar and dissimilar metals without the input of external heat and without any critical formation of their intermetallic phases[70, 71]. Sheets, profiles, and tubes can be processed. During the MPW process in tubular configuration, the parts being welded (the flyer tube and the fixed inner parent) are positioned inside a tool coil, see the Figure 2.18. During the fast discharge of the capacitor banks via the coil, a magnetic field is generated around the coil, which leads to eddy

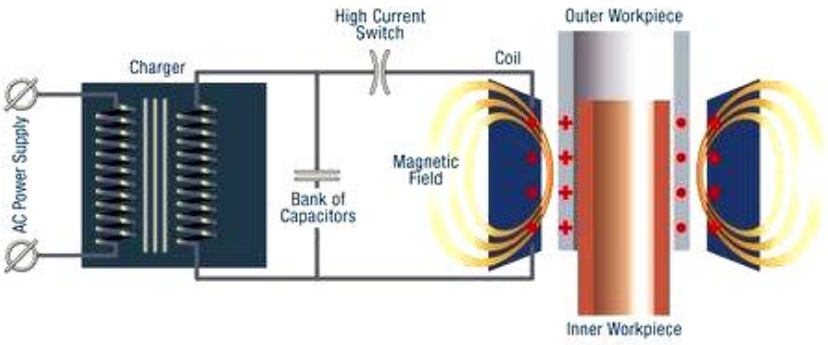

Figure 2.18: Magnetic Pulse Welding Circuit [69].

currents in the electrically conductive flyer part positioned in close vicinity to the coil. To concentrate the magnetic field, e.g. in a smaller joining zone, field shapers are used, which are positioned between the coil and the flyer tube. The eddy currents induced in the flyer create an opposite magnetic field and a repulsive Lorentz force. This force causes the flyer to quickly accelerate plastically and to impact with the inner parent at an extremely high velocity resulting in a metallic bond. It should be noted that in the gap between the shaper and flyer, the two fields have the same direction and the total field is the sum of the field generated by the field shaper and the eddy current.

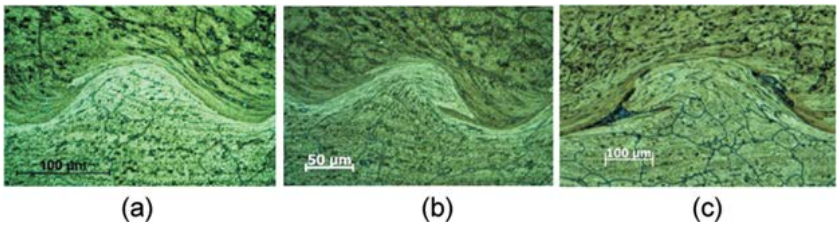

Figure 2.19: Wavy morphology of MPW weld seam showing confined shearing, jetting, irregularly shaped interface and onset of defects. (a) wave formation with upward kinematics, (b) downward kinematics and (c) wavy interface with onset of defects [72].

The possibility to weld dissimilar materials - steel and aluminum, copper and aluminum, etc. is the exceptional advantage of MPW. The weld seam has distinctive wavy morphology shown in the Figure 2.19. Welding with different parameters can lead to various quality seam: high quality seam shown in the

Figure 2.19 a and b, to the weld with onset of defects (see the Figure 2.19 c), which can lead to a failure of car or airplane part or forming without welding. To ensure a stable impact welding process and to optimize the used energy, the impact conditions need to be carefully controlled [73].

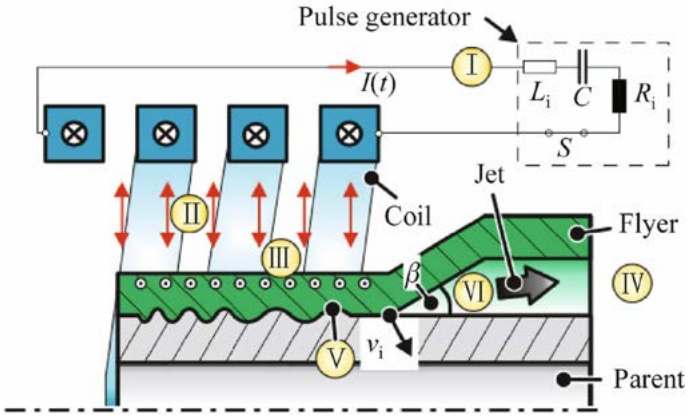

Figure 2.20: Measuring points for capturing of: I current, II magnetic field, III flyer movement and strain, IV optical access for imaging, V plastic deformation, temperature, pressure and contact assessment, VI jet residues and temperature, collision angle β and collision velocity ν_i [11].

Ongoing research is focused finding welding parameters, mainly the collision angle β and the impact velocity ν_i (see Figure 2.20) that would guarantee quality weld - a complicated task, because different alloys, different diameters and wall thicknesses of tubes create wast number of degrees of freedom to be considered. The newest measurement methods are based on optical and mechanical measuring technologies taking advantage of the hypervelocity impact flash, the impact pressure and the deformation necessary for the weld formation. Still, for example, impact velocity ν_i that can be only simulated in cannon-experiments and other mechanical apparatuses; these modeled impact conditions have to be transferred to the impact welding process. Furthermore, the correlation between the impact conditions and the weld properties requires suitable analysis methods [11].

Analyzed state the art MPW analysis methods either need complicated equipment (to be used in laboratory conditions), either are based on numerical simulations or (and) include destructive testing. Due to physical limitations of pick-up coils used for magnetic pulse measurement, magnetic pulse cannot be measured with during welding process, but using solid rod instead of flyer

and stationary workpiece. So determining impact velocity ν_i, which is a function of gap between welded parts (i.e. travel distance) and time before impact (acceleration time) in actual MPW process is still an open issue.

Chapter 3

Preparation of the Samples and Experimental Setup

3.1 Preparation and Characterisation of the Samples

3.1.1 PI MOCVD Thin Film Deposition Technique

Pulse injection (PI) metal organic chemical vapour deposition (MOCVD) technique has been chosen for the deposition $La_{1-x}Sr_xMn_yO_3$ (LSMO) films on several types of substrates. The PI MOCVD technique [74, 75] and has been developed and patented by Vilnius University Faculty of Chemistry and Geosciences.

The PI MOCVD reactor (see Fig. 3.1) consists of a vertical hot wall chamber with sample holder, horizontal tube with evaporators, Ar and O_2 supply and vacuum pump. The sample holder can house up to 2 inch (50 mm) substrate wafers. Each of the three evaporators can hold an injector for injection of microdoses (of a few mm^3) of an organic solution with a dissolved mixture of organometallic precursors. After computer controlled flash evaporation of precursors, the flow of Ar and O_2 gases transports the the precursors to the heated substrate. The precision of deposition is assured by high speed and precision electromagnetic valve operating in pulse mode. This guarantees precision and reproducibility of precursor delivery, ensuring the reproducibility of the whole CVD process. Film composition, growth rate and conditions can be controlled by pressure in the reservoirs with the solutions, concentration of each solution,

pulse duration, injection frequency.

For the film growth precursors were made by dissolving La(thd)3, Sr(thd)2, and Mn(thd)3 (thd stands for 2,2,6,6-tetramethyl-3,5-heptandionate) in toluene. Micro-doses of approximately 3 mg of the organic solution organometallic precursors were injected at 2 Hz frequency.

Substrates

The substrates have been chosen that facilitate the growth of nanostructured films with nanosized crystallites. Four types of materials have been used as substrates to experiment with different types of crystallites: glass-ceramic; polycrystalline Al_2O_3, SiO_2 Thermal Oxide and Quartz:

- For glass-ceramics substrate polycrystalline Lucalox (99.9% $Al_2O_3 + 0.1\%$ MgO) has been used. Glass-ceramics is produced by controlled crystallization - during nucleation process various metal oxides are added [76] . The resulting material has no porosity, the fine-grained crystalline phase crystallites are randomly oriented and uniformly distributed in a volume of amorphous matrix. The substrate produced from this material has a very low or even negative thermal expansion coefficient, high thermal stability, high mechanical strength, chemical durability.
- For polycrystalline Al_2O_3 Ceramic Substrate of SUPERSTRATE 996 with purity 99.6%, grain size < 2.0 μm, thickness 0.5 mm, surface roughness < 25 nm has been used. The high purity and small grain size allow the material to be smoother with less surface defects.
- Thermal Oxide Wafer: 1000 nm SiO_2 Layer on Si (100), surface roughness, R_a: < 5 $\mathring{A}$.
- Quartz substrate has been chosen because of two reasons: lattice mismatch and economic reasons. Quartz lattice constants are $a \approx$4.9033 $\mathring{A}$, $b \approx$5.3939 $\mathring{A}$ [77], while LSMO lattice constants are $a \approx$5.697$\mathring{A}$, $b \approx$7.709$\mathring{A}$ and $c \approx$5.547$\mathring{A}$ [78]. The differences in lattices constants shall be sufficient to facilitate polycrystalline growth of LSMO. Relatively low cost of quartz substrate is attractive from production scaling perspective. The chosen material was single crystal SiO_2, orientation- AT-cut, thickness 0.5mm with surface roughness < 5 $\mathring{A}$.

Deposition of the thin films with PI MOCVD

The film growing conditions have been adjusted to achieve different predefined thickness of thin films. The first group of films was grown at a constant deposition temperature of 750 °C and changing the deposition time thus producing

the films with different thicknesses d. The thicknesses of the films were estimated with a profilometer and with a transmission electron microscope (TEM). The films from this group films had the following thicknesses: 25; 75; 170; 360, 400; and 900 nm. The film growth rates of 12.5 nm/min for the 25 nm thick film and 18–20 nm/min for other thickness samples are considered to be relatively high.

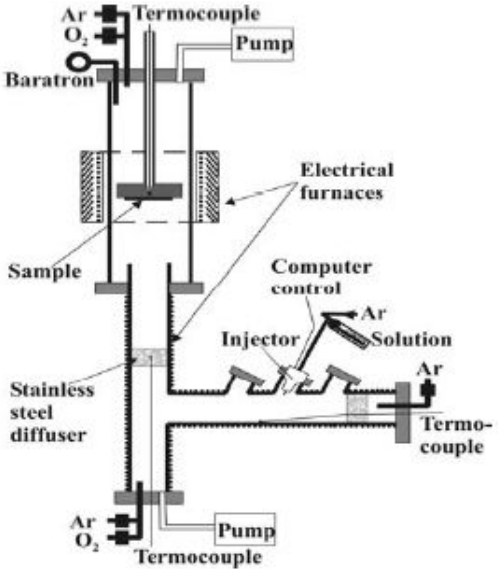

Figure 3.1: Principle of MOCVD reactor [51]

After measurement of temperature T_m of resistivity maximum ρ_m (see Fig. 3.2) the 400 nm thickness samples were identified as having characteristics most suitable for sensors at room temperature (T_m=235 K and ρ_m= 1 Ωcm) and second group of samples was grown to this thickness.

The growth tactics for the second group of the films was to maintain constant thicknesses of d = 400 nm while changing the deposition temperature T_{dep} from 600°C up to 775°C in steps of 25°C. The growth rate of the film was relatively steady (≈20–22 nm/min), indicating, that the films were deposited in a controlled diffusion regime.

The samples were investigated for T_m and ρ_m parameters and optimum deposition temperature of 750 °C has been identified (T_m=235 K and ρ_m= 1Ωcm).

The third group of samples was grown at 750°C identified at the previous step on substrates with different surface morphology, polycrystalline Al_2O_3,

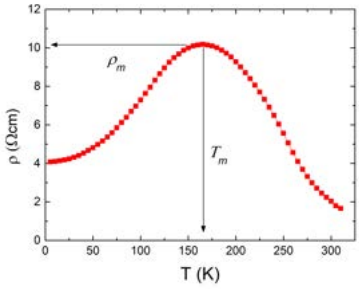

Figure 3.2: Typical resistivity dependence on temperature for the LSMO samples. The highest resistivity ρ_m is achieved at the temperature T_m.

Amorphous Si/SiO_2-1000 and monocrystalline Quartz. The films were grown to 360 nm and to 60 nm thickness (control group).

Finally, the fourth group of samples was grown to 400 nm thickness at 750 °C temperature and changing Mn content in the film (effectively, adjusting $\frac{Mn}{La+Sr}$ ratio).

After the completion of the growth process, all the films were at the deposition temperature for 10 min annealed in a pure O_2 atmosphere and then slowly (at a rate of $\approx$ 4.7 °C/min) cooled to the temperature of 350 °C.

Deposition of the thin films by radio-frequency magnetron sputtering

The $La_{0.66}Sr_{0.34}MnO_3$ (LSMO) thin films were deposited at 750°C by radio-frequency (RF) magnetron sputtering onto commercially available (001) oriented single crystal cubic yttria-stabilized zirconia (YSZ) substrates with 9 wt.% of Y_2O_3. Ceramic $La_{0.66}Sr_{0.34}MnO_3$ target used for film deposition has been prepared by a conventional solid state reaction method using appropriate ratios of high-purity powdered La_2O_3, $SrCO_3$, and MnO_2. The oxide compound was synthesized by heating the pressed powder mixture in air at 1200°C for 4 h. Then the product was ground and pressed into a 250 mm diameter disk, sintered at 1200°C for 2 h and annealed finally at 1000°C for 10 h. Sputtering was performed using Ar-O_2 gas mixture with (1:1) molar ratio and partial oxygen pressure of about 15 Pa. The films deposition rate was $\approx$1.5 nm/min. After film deposition, the chamber was filled with oxygen at atmospheric pressure and the films were held at 600°C for 1 h to be saturated by oxygen. Finally, under the same oxygen pressure, the films were cooled down to the room temperature at the rate of $\approx$15 °C /min.

3.1.2 Characterization of Surface Morphology and Microstructure

Analysis of Chemical Composition

For investigation of the chemical composition, samples of the LSMO films were dissolved in HNO_3 acid. The solution samples were then analyzed by inductively coupled plasma high-resolution mass spectrometry (ICP-MS) method with *Thermo Scientific Element 2* equipment.

For high accuracy, three samples from each film specimen were analyzed and average values of x and y of $La_{1-x}Sr_xMn_yO_{3\pm\delta}$ were determined. This way the chemical composition was calculated with accuracy better than 1%.

Surface Morphology and Crystal Structure The morphology of the films surface was investigated with scanning electron microscope (SEM) *Hitachi SU70* with attached energy-dispersive X-ray spectrometer (EDS). The crystal structure of the films was analyzed with X-ray diffraction (XRD) *SmartLab* diffractometer, reflection high-energy electron diffraction (RHEED) (*EMR-100* electron diffraction camera) and selected-area electron diffraction (SAED).

The detailed microstructure was characterized in cross-section of the samples with the transmission electron microscope (TEM) *Tecnai G2 F20 X-TWIN*. For TEM imaging, samples were selectively coated with Pt protection layer (using mask), cut with Ga^+ ion beam and polished. The thickness of the films was evaluated from TEM images of the films.

Evaluation of Dimensions of the Crystallites

ImageJ open source Java image processing program has been used for statistical evaluation of dimensions of the crystallites. Since crystallites have different shapes, the diameter d of the crystallites is calculated from the area of the crystallites: $d = \sqrt{\frac{4S}{\pi}}$, where S is the area of the crystallite. In this Dissertation the *average diameter of the crystallites* and the *most probable diameter of the crystallites* are interchangeable terms meaning *most probable diameter of the crystallites*.

3.1.3 Deposition of the electrodes and wiring

Ag contact pads were deposited on the LSMO film over very thin (3-5 nm) intermediate Cr adhesion layer (see Figures 3.3 and 3.4). For resistance measurements, 50 to $150\,\mu\mathrm{m}$ diameter Ag wires have been soldered to deposited contact pads. Indium solder was used because of ductility at cryogenic temperatures and intermediate melting temperature [79].

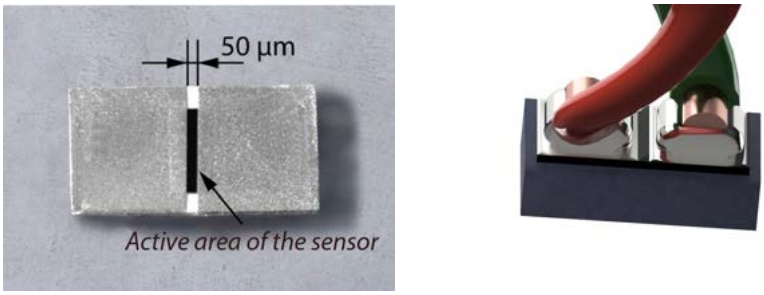

(a) (b)

Figure 3.3: (a) Photo of the prepared sample, (b) 3D model of the sensor.

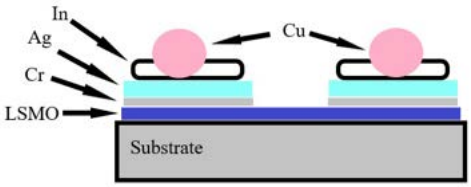

Figure 3.4: Schematic profile of the sample with deposited contact and wires.

For measurements in the pulsed magnetic field in order to minimize the current induced in the connecting wires by high dB/dt of magnetic pulses, the twisted pair wires were used to connect the LSMO sample to the measuring equipment. Still, it shall be noted that twisted pair cables cannot completely eliminate induced EMF, because magnetic flux density depends on the distance from the source of the magnetic field (see Figure 3.5). The active surface of the LSMO sample and the soldered area with contacts were covered by chemically stable lacquer.

3.2 Measurement Equipment and Methods

This section describes measurement equipment and methods used for the investigation of LSMO films.

The Figure 3.6 explains definitions of sample orientation in the magnetic field during magnetoresistance measurements: $B_\perp$ - is the orientation when the magnetic flux is perpendicular to the sample (or sensor) plane, magnetic flux

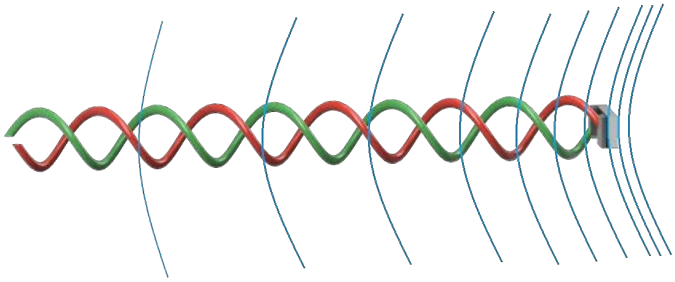

Figure 3.5: LSMO sample (or sensor) with twisted pair wires in inhomogeneous magnetic field.

can be parallel to the sample plane $B_{\parallel}$ in two cases - magnetic flux perpendicular to the current ($B \perp J$) and magnetic flux parallel to the current ($B \parallel J$).

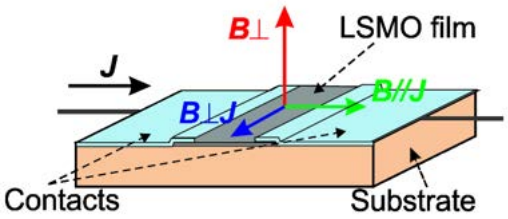

Figure 3.6: Set up for $MR_{\parallel}$ and $MR_{\perp}$ measurement and MRA calculation [80].

3.2.1 Measurements in a wide temperature range

Resistivity and magnetoresistance dependence on temperature in the temperature range from 5 to 300 K was investigated in a closed cycle helium gas cryo-cooler.

Setup for measurements of conductivity (resistivity) of films in permanent magnetic field up to 0.8 T in the temperature range 5-320 K consists of closed cycle helium gas cryo-cooler and electromagnet with programmable power supply (Agilent Technologies N5769A) for magnetic field cycling. The copper holder with samples and thermal sensor inside 30 mm diameter vacuumed chamber was placed between the poles of the electromagnet.

The samples were positioned on the copper sample holder with one of two types of adhesives: *FASTIK* general purpose glue and *Apiezon N Grease*. The

latter is silicone-free cryogenic high vacuum grease, which can withstand frequent cycling between cryogenic temperatures as low as 5K and 303 K [81]. *Apiezon N Grease* is very convenient for experiments because it is easy to position and remove samples at room temperature, while the grease solidifies to craze-free form at low temperatures.

Resistance of the samples has been measured with *Lakeshore* Resistance Bridge, data has been recorded with „LabView“ customized program.

3.2.2 Measurement of Resistance in High Magnetic Fields

Magnetoresistance measurements of LSMO films in high magnetic fields has been done using pulsed magnetic field generator based on capacitor bank discharge through a non-destructive induction coil [80].

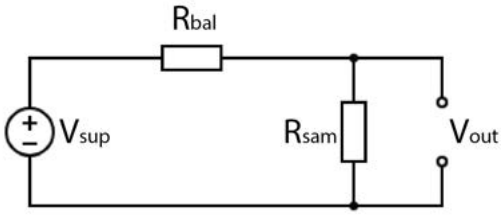

Figure 3.7: Circuit for sample connection for resistace and magnetoresistance measurement experiments. R_{sam} - resistance of the sample, R_{bal} - resistance of the ballast resistor, V_{sup} - supply voltage, V_{out} - output voltage across the sample (or the sensor).

Magnetoresistance anisotropy MRA was calculated from $MR_{\perp}$ and $MR_{\parallel}$ data using formula 2.10. The resistance has been measured using the circuit shown in the Figure 3.7 and calculated from Equation 3.1.

High magnetic pulse forming circuit

The high magnetic pulse forming circuit (or the high magnetic field pulse generator) was used for magnetoresistance measurements in high magnetic fields. The generator consists of following principal parts [82] (Figure 3.8):

1. High voltage DC power supply unit for charging capacitors;
2. High voltage capacitor bank;
3. High power switch with crowbar circuit;

4. Reinforced inductor;
5. Voltage measurement Unit;
6. Remote control unit;
7. Magnetic field meter.

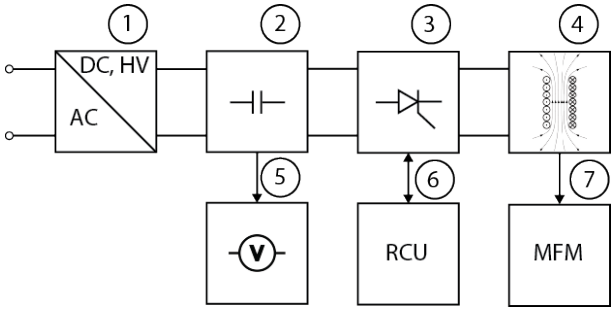

Figure 3.8: High magnetic pulse generator block diagram.

The high voltage DC power supply unit 1 is set to generate DC voltage equal or slightly above required capacitor charging voltage, typically 7-10 kV, then the capacitors are charged to required discharge voltage while monitoring voltage on Voltage measurement Unit 5. The discharge of the capacitors is triggered with Remote control unit 6 (mainly for the safety of experimentators), which short-circuits the High power switch 3. The capacitors are discharged through the Reinforced inductor 4 (inside which manganite samples or workpieces are placed) creating the current of kilo amps range and generating high magnetic field pulses in the order of 5-40 Tesla. Magnetic pulse inside the inductor is measured with reference Magnetic field meter 7.

For example, the magnetic field generator with 5.4 mF 4 kV capacitor bank generates up to 40 kA current through the inductor, which generates up to 40 T magnetic field pulses.

LSMO samples were connected to the measurement equipment using the circuit shown in the Figure 3.7. A 6.2 kΩ ballast resistor R_{bal} was connected in series to the sample. The sample resistance R_{sam} was calculated from Equation 3.1:

$$R_{sam} = \frac{V_{out} R_{bal}}{V_{sup} - V_{out}} \tag{3.1}$$

Here, V_{sup} was the power supply voltage and V_{out} was the measured sample output voltage. The measurements are controlled by personal computer with „LabView“ software based programs: one for automated measurement of resistance dependence on temperature; the other one for measurement of resistance dependence on magnetic field.

3.2.3 LSMO film application in Magnetic Pulse Welding

The setup for Magnetic Pulse Welding testing was installed at the Institute of Forming Technology and Lightweight Components of TU Dortmund University. It consisted of a pulse power generator (*Poynting SMU 0612 FS*), a compression coil (*Poynting SMU-K97-8/90*, 8 windings coil with an inner radius of 48.5 mm and a length of 91.6 mm), a field shaper outer axial length of 110 mm and a length of the concentration zone of 15 mm was used to adapt the solenoid compression coil to the outer diameter of the tubular specimens, and workpieces (parent rods and flyer tubes) [83]. The principal parts of welding equipment are shown in the Figure 3.9.

The flyer tubes (the tubes, that are compressed on to the parent part by magnetic pulse) were made of EN AW-6060 aluminum with an outer diameter of 40 mm and a wall thickness of $d = 1.5$ mm. Before the experiment, the tubes were annealed at 300 °C for 2 hours. Cylindrical parent parts made of steel C 45 were positioned inside the flyer tube with a radial standoff of $h = 1.5$ mm. The current I(t) flowing through the compression coil was recorded with a Rogowski coil (CWR 3000 B type, *Power Electronic Measurements Ltd.*) connected to a digital oscilloscope (*LeCroy Waverunner 104 MXi*).

The weld quality was examined by a peel testing method - a standard test method for the determination of the joint strength of adhesive joints, often used for the analysis of Magnetic Pulse Welding (MPW) specimens [11]. For the analysis, after welding, small kerfs were cut into the aluminum flyer and the resulting strips were peeled off from the parent. A separation of the whole aluminum strip indicates a poor welding seam; failure in the weaker part of the base material outside the weld is a sign of a sound weld.

The magnetic field dynamics between the field shaper and the flyer during electromagnetic compression and MPW was measured with CMR-B-scalar sensor probe connected to a high-pulsed magnetic field measurement system measurement module, developed at the State research institute Center for Physical Sciences and Technology, Vilnius, Lithuania, and described in more details in Stankevič et al. [4]. The probe was made as a flexible, 3 mm in diameter and

1 m long screened cable with a $1 \times 0.5 \times 0.25\,\mathrm{mm}^3$ CMR-B-scalar sensor at its tip.

During the experiments, the pulse power generator discharge energy E was set to values between 2.0 and 5.0 kJ.

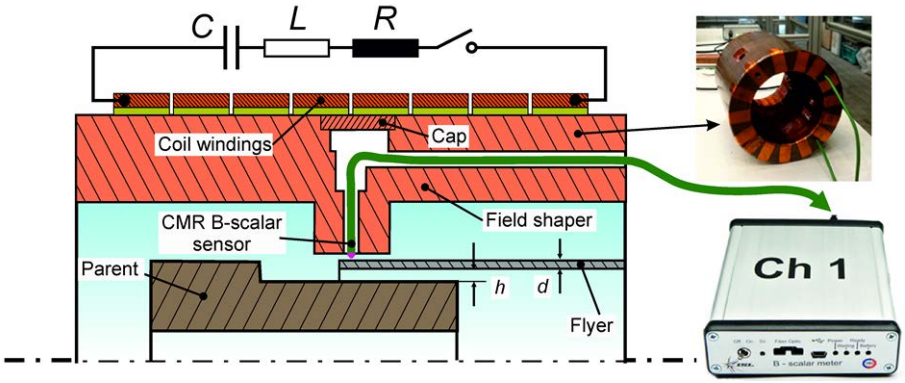

Figure 3.9: Set-up for magnetic pulse measurement in Magnetic Pulse Welding system for round object. Left- simplified principle circuit and schematic cross section of the set-up inside the coil; top right- the field shaper with the CMR sensor; bottom right - magnetic field measurement unit [4].

Chapter 4

Results

Room temperature CMR-B-scalar sensors, made from nanostructured $La_{1-x}Sr_xMnO_3$ (LSMO) films are well suited for high speed recording of the absolute magnitude of the magnetic flux density of high magnetic field pulses due to expressed the colossal magnetoresistance effect [84, 85]. However, during applications like Magnetic Pulse Welding, due to metal compression, some heat is dissipated and the temperature in the vicinity of the sensor can rise above room temperature. Therefore this application requires improvement in the magnetoresitive characteristics of the CMR-B-scalar sensors at higher temperatures.

This work has been started from LSMO deposition on Glass Ceramics substrates to develop base understanding about relation between (A) film materials and growth conditions and (B) electric and magnetic properties of the films.

4.1 LSMO on Glass Ceramics

4.1.1 Thin films thickness variation

The first task has been to check, how the structure and parameters of the films depend on the thickness of the film. The best method for achieving different thicknesses was adjustment of the film deposition time, keeping other conditions constant.

The first group of films with composition $La_{0.83}Sr_{0.17}Mn_yO_{3\pm\delta}$ (where $y =$

1), grown at 750 °C constant temperature and varying the deposition time produced the samples with thicknesses d of 25; 75; 170; 280; 360, 400; and 900 nm (see the Table 4.1). The lowest growth rate of 12.5 nm/min was for the 25 nm thick film. The growth rate has slightly increased to 18–20 nm/min for thicker films; it has taken approximately 22 minutes to grow 400 nm film and 47 minutes to grow 900 nm film samples.

Table 4.1: Main characteristics of the sample Set 1, composition $La_{0.83}Sr_{0.17}Mn_yO_{3\pm\delta}$ (where $y = 1$), glass-ceramic substrate, deposition temperature 750 °C.

Sample	T_m**, K**	ρ_m**,** Ω **cm**	**d, nm**
1-1	130	135	25
1-2	172	12	75
1-3	220	3.4	170
1-4	235	1.0	400
1-5	220	1.5	900

4.1.1.1 Morphology and structure of the deposited thin films

Morphology analysis of the films with different thickness gives insight into development of columnar crystallites (see Figure 4.1) during crystallisation process. The morphology of the thinnest 25 nm film (see Figure 4.1, a) was not expressing structure with crystallites, indicating rather amorphous film, but the thicker (d = 75 nm, see 4.1, b) film showed the pronounced surface grain structure: the film was densely packed with crystalltes without pinholes, resulting in a homogeneous film over the sample area. The grains of the film had polygonal shapes with an average lateral width D_{avg} of about 55 nm. Further increase in the film thickness (170 nm) was accompanied by an increase in the roughness of the surface morphology. The lateral width of the polygonal-shaped grains increased up to $\approx$ 58 nm, the larger crystallites (about 80 nm) show trigonal crystal systems (see 4.1, c). Variety of surfacing shapes is developed if columns grow with rhombohedral perovskite structure, but with random orientation: after nucleation is stopped at certain thickness, SEM images show sections of columns at different angles.

More detailed study of the microstructures of the films were done by analyzing TEM images. The low-magnification crossectional TEM images of the thinnest 25 nm thick films are shown in Figure 4.2 a and b. There seems to be difference in crystal structure of the two 25 nm segments, taken from the same sample:

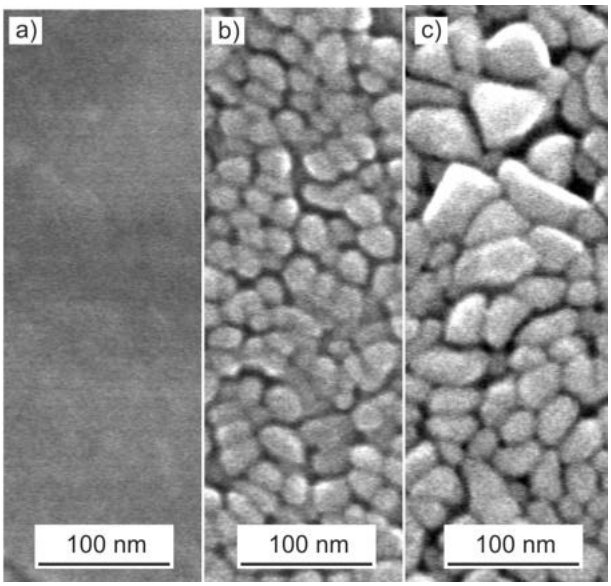

Figure 4.1: SEM surface images of LSMO films grown at 750 °C temperature on glass-ceramics substrate. Thicknesses of the films: a - $d = 25$ nm, b - $d = 75$ nm, c - $d = 170$ nm.

(a) segment resembles amorphous layer, whereas (b) segment shows granular structure.

Further clarifications is provided by selected-area electron diffraction (SAED in TEM) and reflection high-energy electron diffraction (RHEED) analysis (RHEED method provides integrated information about the crystal structure of the film surface, while SAED provides information about the local film structure). The diffraction patterns of the $d = 25$ nm thickness films (see Figure 4.3) show blurred, low intensity rings, indicating presence of an amorphous film containing a small number of randomly oriented crystallites, but having no overall texture or any preferred crystallite alignment of the polycrystalline structure. The SAED picture from the region (see the inset of the Figure 4.3) showing the amorphous rings accompanied by very weak intensity patterns supports this conclusion.

Crossectional TEM images of thicker, 75 and 170 nm films (Figure 4.2 c and d respectively) show the grains (crystallites) of the films taking columnar shapes with typical column widths of $d = 40 \div 65$ nm. The columns span vertically throughout the whole film thickness with their long axis oriented close to per-

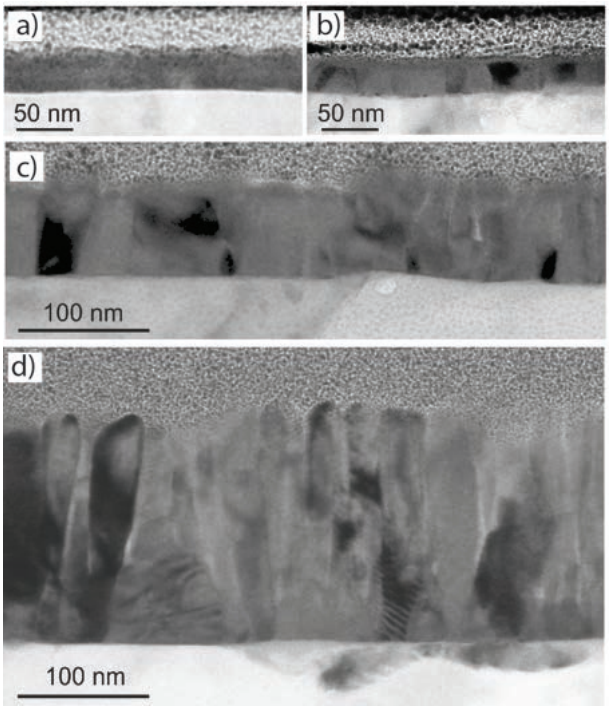

Figure 4.2: Cross-sectional bright-field TEM images of LSMO films grown at 750 °C on glassceramics substrate: thickness $d = 25$ nm (a, b), thickness $d = 75$ nm (c) and thickness $d = 170$ nm (d).

pendicular to the substrate. The columns are separated by 5–10 nm thick grain boundaries, occupying all the space between them. The contrast of the TEM images within the columns shows that some columns are not a single crystal, but rather consist of several single crystal slabs (most likely twins).

The diffraction rings in the RHEED patterns of 75 and 170 nm thick films (see Figure 4.4) become sharper with an increase in the film thickness and break into arcs, indicating the formation of out-of-plane textures. These particular samples exhibit non-ideal textures with one-degree orientation having angular dispersion of about 45° (see Figure 4.4 b). The lower-order arcs are labelled as (111) in the pseudo-cubic lattice. This kind of texture appears due to the shadowing and the anisotropy of the growth velocity of the crystallites. The SAED patterns obtained from the thicker films are presented in the bottom insets of Figure 4.4. They represent a superpositioning of the diffraction from several crystallites being at an angle in respect to the other crystallite. The

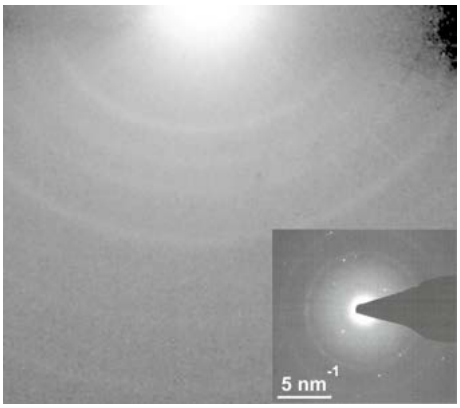

Figure 4.3: The RHEED patterns of LSMO films with $d = 25$ nm thicknesses. Insets: SAED pattern of the same film.

upper insets show the dark field images from a discrete spot (marked by dotted circle in the diffraction patterns) indicating that the two crystallites (bright) have the same orientation.

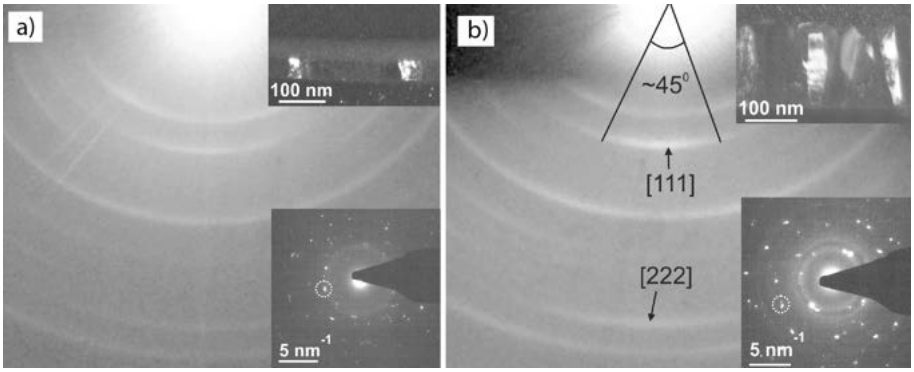

Figure 4.4: The RHEED patterns of LSMO films with $d = 75$ nm (a) and $d = 170$ nm thicknesses. Insets: SAED pattern of the same film.

The resulting patterns of 25 nm and thicker films, particularly absence of clearly expressed grains in thinnest film vs columnar structure in thicker films indicate difference in growth mechanism for different thicknesses.

Crystallization temperature has inverse exponential relation to layer thickness [86–88], so it is very likely that while thicker films develop crystallites at 750°C deposition temperature, the crystallites may not form in very thin films, be-

cause the crystallization temperature rapidly increases with decreasing layer thickness and 750 °C temperature becomes not sufficient.

The films are deposited through nucleation, grain growth, coalescence and the further film growth processes. Initially, on the substrate, grows amorphous thin layer, then an increase in the film thickness leads to the appearance of some preferred crystallographic directions, that are normally aligned to the film surface, grain growth and coalescence leads to columnar growth. It would be natural to expect, that in thicker films the thin layer (at least 10 nm) adjacent to the substrate shall be amorphous as well, which is not the case. The possible explanation can be that although the 10 nm layer is deposited in half a minute, this thin layer remains in 750°C environment for prolonged period - up to half an hour. During this time amorphous layer shrinks because atoms from this layer nucleate on the crystallites growing from above and we see columnar structures going all the way from substrate to surface of the film in the TEM images.

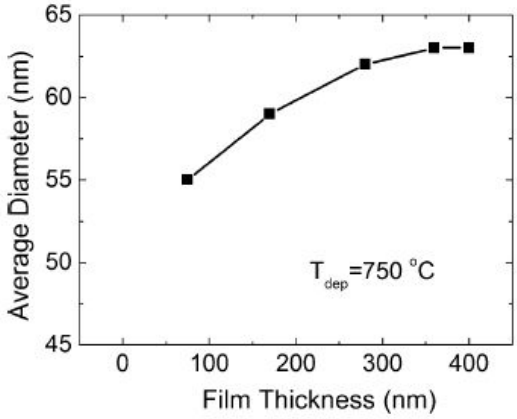

Figure 4.5: Dependence of average diameter of grains on film thickness evaluated from SEM images.

It shall be noted, that as the films were grown on glass-ceramics substrates, which have adjacent amorphous and several crystalline phases, the underlying substrate phase influences nucleation of the film. The nucleation process on the crystalline segments of the substrate is smoother than the nucleation on the amorphous segments so it could happen, that where deposition takes place on substrates with partly amorphous and partly crystalline, in ultra-thin films, this can lead to the production of partly amorphous films and partly crystalline

film as well.

Figure 4.5 summarizes the analysis of the surface morphology: with an increase in the film thickness, the average diameter of the crystallites (column width) increases. The graph shows that the grain sizes reach saturation at about 400 nm thickness, however, for the films with 900 nm thicknesses (not shown in the figure), surface areas with smaller grains were observed, resulting in decreasing average diameter (to $\approx$ 60 nm) of the crystallites and the more defective structures of the films.

The grain boundaries of the thin films seem to play very important role in transport properties of the nanostructured LSMO thin films, thererefore the chemical element distribution in the crystallite-grain boundary areas of these film was studied with the energy-dispersive X-ray (EDX) spectroscopy in the scanning transmission electron microscopy (STEM). Figure 4.6 a shows the image of the STEM of the film with thickness $d = 400$ nm grown at $T_{dep} = 750$ °C. The image contrast reflects the density and the chemical composition of the film. The profile of the EDX line scan of the La, Sr, Mn and C elements across the grain boundary is presented in Figure 4.6 b.

Across the grain boundary area, the concentration of La, Sr and Mn - the main composition elements of the film - decreases, while the concentration of the carbon increases. The film contamination with carbon is a side effect of growing films with MOCVD technique, caused by the thermal decomposition of the organic molecules of the precursors. During the growth of the film, carbon is pushed from the surface of the grains down to the intergrain region and accumulates there. This accumulation prevents free migration of the atoms between the individual columns during the growth of the film and when columns reach certain thickness (seen as saturation in the Figure 4.5), the lateral dimensions stabilize.

The substrate temperature plays an important role in this process. While the film grows, two processes take place simultaneously: decay of the organic molecules of the precursors along with formation of carbon deposition on the film and the evaporation of the carbon from the surface of the film. At higher temperatures, the latter process dominates, thus producing a better structure of the film, as seen in the Figure 4.9.

From application point of view, some content of carbon in nanostructured film plays positive role, because the carbon inside the grain boundary region keeps the grain boundary layer sufficiently thick (5–10 nm) compared to grain boundaries of the conventional polycrystalline ceramics (typically less than a few nm). As a result, the magnetoresistance of films grown by MOCVD

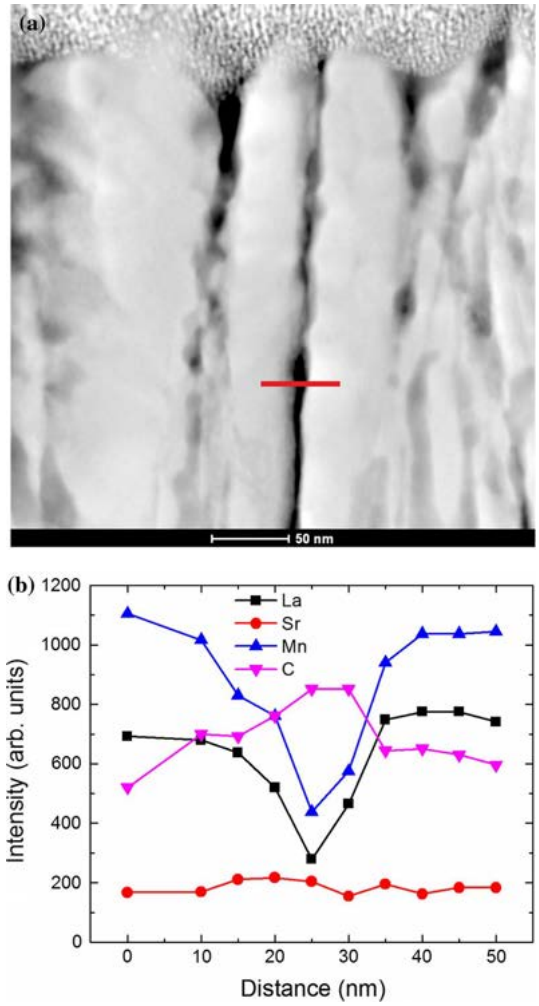

Figure 4.6: Grain boundary element analysis: (a) STEM image of film with thickness $d = 400$ nm grown at $T_{dep} = 750$ °C, (b) EDX line scan for La, Sr, Mn and C element content across the grain boundary (red line in figure a).

method saturates only in very high magnetic fields (reaching tens of Tesla) - very important feature for the development of high pulsed magnetic field sensors.

4.1.1.2 Resistivity analysis

As have been discussed earlier, growing films with different deposition times resulted in film thickness ranging from 25 nm to 900 nm. Values of maximum resistance ρ_m and maximum resistance temperatures T_m, K are shown in the Table 4.1, dependencies of resistivities ρ on ambient temperature for films with thicknesses of 25 nm; 75nm, 170 nm and 400 nm are shown in Figure 4.7.

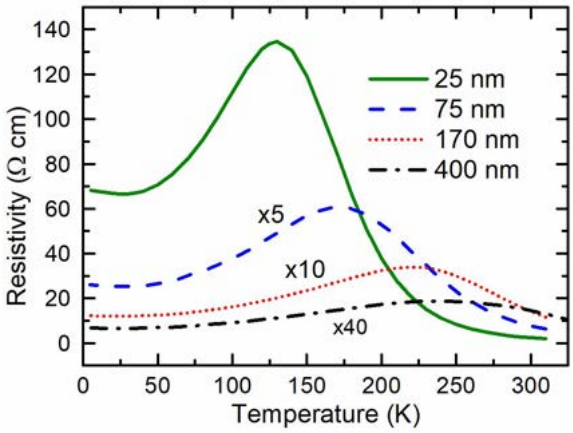

Figure 4.7: Comparison of Resistivity dependences on ambient Temperature for films with different thicknesses: 25 nm, 75 nm and 170 nm.

Figure 4.7 shows, that each of the films exhibit different phase transition from metal-like to an insulator-like temperature T_m and the electrical transport parameters of the films are significantly different: the thinner films have lower metal– insulator transition temperature T_m and higher maximal resistivity ρ_m. Both the values of T_m and ρ_m make a startling difference between polycrystalline and good quality epitaxial LSMO layers: while ρ_m of polycrystalline films range from 1Ω cm to more than hundred Ω cm and T_m below 250 K, the later exhibit the resistivity in the order of micro Ω cm [5, 89] and usual metal–insulator transition temperature T_m higher than 310 K.

The characteristics of the investigated nanostructured films depending on the crystalline microstructure of the films and the film thickness can be explained

in following way. The nanostructured film consists of randomly distributed crystallites having perfect crystalline structure and separated by grain boundaries. The grain boundaries should be considered as disordered LSMO material with inhibited electric and magnetic properties [90]. The electric circuit of such set-up can be approximated as a two-dimensional percolation network, consisting of elements with low resistivity (crystallites) and elements with high resistivity (grain boundaries). The conducting mechanism inside crystallites, like in doped monocrystalline manganites, is governed by the double-exchange mechanism between the manganese ions: Mn^{3+}–O–Mn^{4+} with closely aligned spins, while in grain boundaries the double-exchange mechanism is complicated due to misalignment of spins, caused by severe distortion and defects of crystal cells. The combined resistivity of the polycrystalline films percolation network is therefore mostly determined by the high resistivity of the grain boundary material and relative amount of this material between crystallites [1, 91]. Depending on the level of disorder of the grain boundaries, the resistivity of the films can span over a wide range.

The highest resistivity and lowest T_m of the 25 nm film is explained by morphology: SEM image (see Figure 4.1) and TEM images (see Figure 4.2 a, b) show, that the film mostly consists of disordered, presumably amorphous material, which has much higher resistivity than crystalline material (above 15 Ω cm [92]).

Relatively high resistivity of the 75 nm film is explained by small crystallites (rather than clearly expressed columns as in thicker films, see Figure 4.2 c) and abundance of high resistivity disordered material around crystallites.

As the thicker film has larger crystallites and less grain boundary material this is reflected in lower resistivity profiles (see Figure 4.7- 170 nm and 400 nm graphs). When the columns get thicker (see Figure 4.2 d) and there is more monocrystalline material with higher conductivity bound in volume (see lower inset in Figure 4.4 b), resistivity of the film decreases and their T_m shifts to higher temperatures.

The lowest resistivity (ρ_m = 1.0 Ωcm) and the highest transition temperature ($T_m \approx$ 235 K) were exhibited by the 400-nm-thick film with the highest average crystallite dimensions (63 nm) (Figure 4.7). The resistivity ρ_m =1.5 Ω cm of the thickest investigated film (900 nm), was higher than that of 400 nm film and the $T_m \approx$ 220 K was lower than for the 400-nm-thick film, most likely due to the larger disorder, which had been introduced during the growth of this thick film.

4.1.1.3 Magnetoresistance analysis

The magnetoresistance dependence on temperature of these films when the magnetic flux density is 20 T are presented in Figure 4.8. Since the MR of manganite films is negative, for easier comparison with the $\rho_m(\mathrm{T})$ characteristics the absolute values of the MR are presented. The maximal MR values are achieved at temperatures close and above the metal–insulator transition temperature T_m. The picture is a typical example of nanostructured films exhibiting significant magnetoresistance values in a wide temperature range down to low temperatures, contrary to epitaxial films, which exhibit high MR values only at temperatures close to T_m [5, 89]. This phenomena is related to ferromagnetic ordering at $T < T_m$. For perfect structure crystallites or epitaxial films, the paramagnetic–ferromagnetic phase transition interval is narrow and the resistivity change in this region starting from ρ_m is very sharp. Therefore, at low temperatures, the epitaxial manganite film or the crystallite in the polycrystalline material is in its ferromagnetic phase. Thus, saturation of the magnetization can be reached at relatively low magnetic field. Since grain boundaries in polycrystalline films act as disordered magnetic material with reduced magnetization and phase transition temperatures, magnetization saturation of nanostructured LSMO films can be reached only at high magnetic fields.

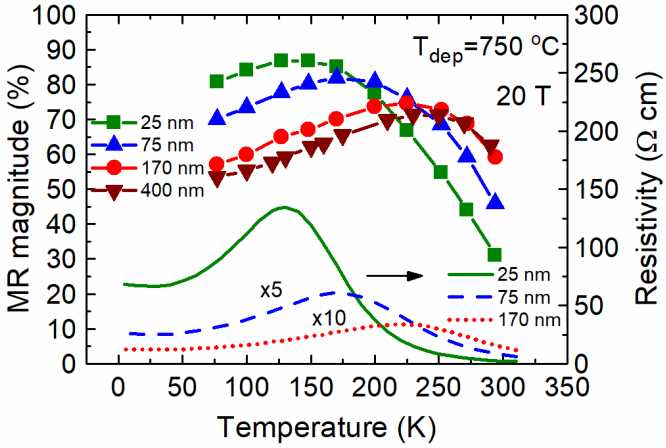

Figure 4.8: Resistivity (right scale) and magnetoresistance (left scale) dependences on temperature for different thicknesses films.

Because of high disorder, the phase transition temperature of the grain boundary material is much lower than that of crystallites and the magnetoresistance of combined system (grain boundaries and crystallites) remains significant down to cryogenic temperatures. For the same reason the maximal MR values at lower temperatures are obtained for mostly disordered films, i.e. for the thinnest (25 nm) amorphous films. The thicker films exhibit higher MR values at high temperatures ($\approx$ 290 K). This is linked to the higher metal–insulator transition temperature, because in the paramagnetic phase far from the T_m, the MR significantly decreases.

The table 4.1 shows summary of the parameters of samples from the first group. Characteristics most suitable for the sensors at room and above room temperature were exhibited by the 400 nm thick sample (sample 1-4: the resistivity maximum of ρ_m= 1 Ωcm at the highest temperature of T_m=235 K). The samples with significantly higher or significantly lower thicknesses have exhibited characteristics less suitable for the purpose, so later ≈400 nm thick samples were grown.

4.1.2 LSMO films grown on glass-ceramic substrates at different deposition temperatures

The purpose of the growth and analysis of the second group of samples was to investigate how the structure of the samples, electric and magnetoresistive properties are influenced by film deposition temperature. Following the conclusions drawn from the first group of samples, samples were grown on the Glass Ceramics substrate to approximately 400 nm thickness. Several lots were grown at different fixed deposition temperatures T_{dep} ranging from 600 °C up to 775 °C in steps of 25 °C.

4.1.2.1 Morphology and structure of the deposited thin films

Resulting samples have varying surface morphology and the substantially different crystalline structure. Figure 4.9 shows TEM and SEM images of the films grown at 600 °C (a, b), 650 °C (c, d), 700 °C (e, f) and 750 °C (g, h). The cross-sectional TEM images of the grown films demonstrate columnar structure with typical column widths of 30–60 nm.

For the films grown at the lowest 600 °C temperature, the microstructure is columnar, but columns are fractured, the film is porous with both inter- and intracolumnar voids outlining a pronounced dendrite-like pattern. Moreover,

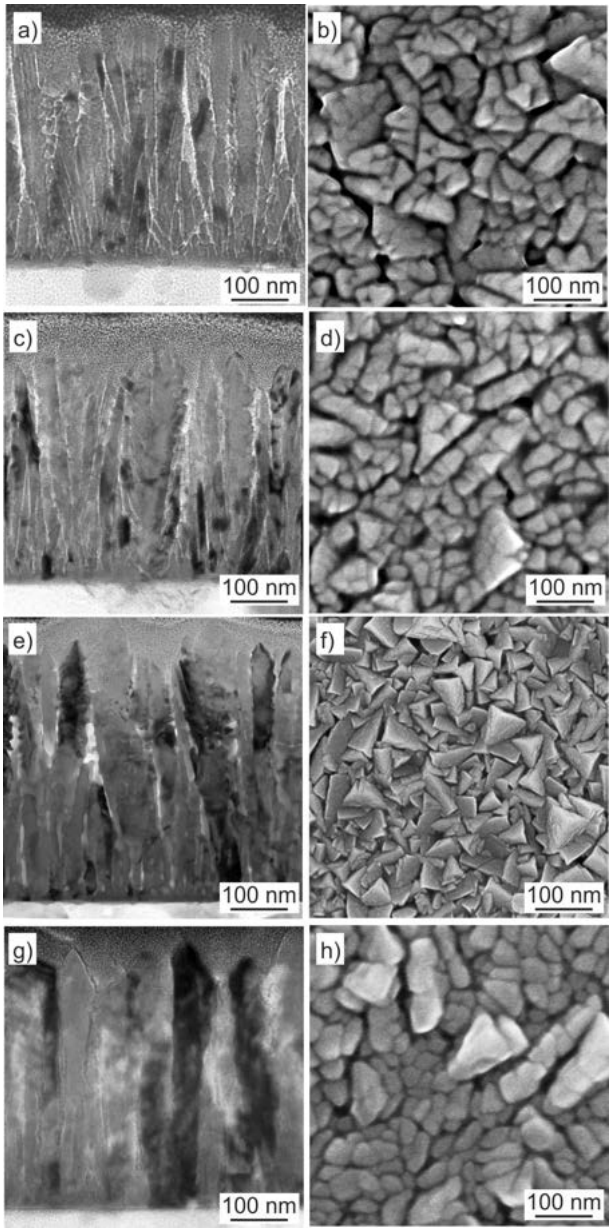

Figure 4.9: Cross-sectional TEM images (a, c, e, g) and SEM surface images (b, d, f, h) of the films grown grown at 600 °C (a,b), 650 °C (c, d), 700 °C (e, f) and 750 °C (g, h) on glass-ceramics substrates.

a mixture of columns and separate crystallites is observed in these films, especially in the regions close to the substrate and the lowest 5 nm layer shows very dissolved pattern, suggesting the beginnings of growth was in the amorphous phase. This is in line with earlier explanation, related to 25 nm thick film- that for very thin films crystallization temperature is substantially higher, the crystallization process can start only when the film grows to some temperature related critical thickness and even keeping the sample in 600 °C temperature for half an hour was not enough for columns to protrude down to the substrate.

The fractured nature of columns in the TEM images reveals that the columns are not single crystalline but rather consist of several single crystal slabs. These slabs form micro-steps, which are seen on the top of the columnar crystals (see Figure 4.9 b).

The images of the film grown at 650 °C (see Figure 4.9 c, d) show very similar patterns to the films grown at 600 °C temperature with only slight improvement in fracturing of the columns and longer protrusion of the columns down to the substrate indicating that crystallization process was somewhat more advanced.

The increase in the growth temperature leads to better columnar structures of the films and to the larger lateral and vertical dimensions of the crystallites (see Figure 4.9 e-h). Shorter traces of Pt layer (deposited on the film before cutting for TEM imaging) protruding into the crystal structure indicate, that the films are denser and inter - crystallite volumes are better filled with disordered material. The best structure with shallowest cavities is of the film deposited at 750 °C (see Figure 4.9 g).

The sizes of the grains increase in size with increase in deposition temperature, approximately 1.5 times from 600 °C to 750 °C with some saturation at higher temperatures (see Figure 4.10). The decrease in the crystallite dimensions at the highest temperature is probably related to a change of the crystallite shape: at 775 °C, the trigonal crystallites were no longer observed in the SEM images, only the smaller irreguarly shaped grains were present.

The growth of the films by varying deposition temperature T_{dep} from 600°C up to 775°C (in steps of 25°C) has confirmed, that the best parameters (maximum resistivity temperature) are achieved at 750 °C deposition temperature (see Table 4.2).

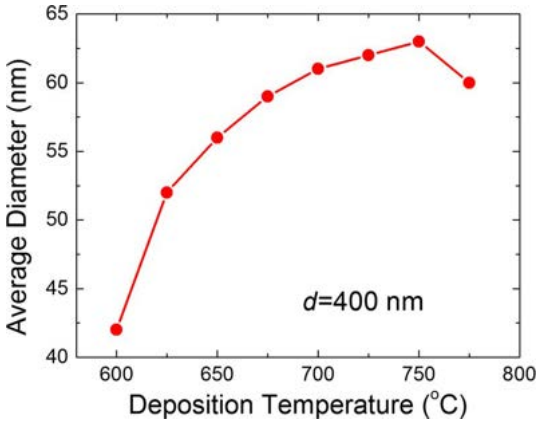

Figure 4.10: Dependence of average diameter of grains on film deposition temperature evaluated from SEM images.

Table 4.2: Main characteristics of the sample Set 2, composition $La_{0.83}Sr_{0.17}Mn_yO_{3\pm\delta}$, $y = 1$, glass-ceramic substrate, thickness $d = 400nm$.

Sample	T_{dep}**, °C**	T_m**, K**	ρ_m**, Ω cm**
2-2	650	150	152
2-3	700	225	4.4
2-4	750	235	1.0

4.1.2.2 Resistivity and magnetoresistance

Figure 4.11 presents the resistivity of the 400-nm-thick manganite films grown at 650, 700 and 750 °C deposition temperatures. The resistivity of the film deposited at 650 °C strikingly resembles resistivity of 25 nm film (only with 15% higher T_m and ρ_m) reflecting very high disorder of the film: small column-like crystallites (see Figure 4.9 c, d) and large volume of disordered grain boundary material. The manganite film grown at 600 °C (not shown in the figure) had very high resistivity and did not exhibit metal–insulator transition in the measured temperature range (measurement limit was up to 9 kΩcm at 50 K). The parameters of the film grown at 700 °C are very close to parameters of the 170 nm thickness film, the film grown at 750 °C deposition temperature has been discussed earlier.

Figure 4.12 presents the magnetoresistance of the films. The films grown at deposition temperature T_{dep} = 650 °C and having most disordered structure with smaller crystallites have the highest MR values at $T < T_m$. The films

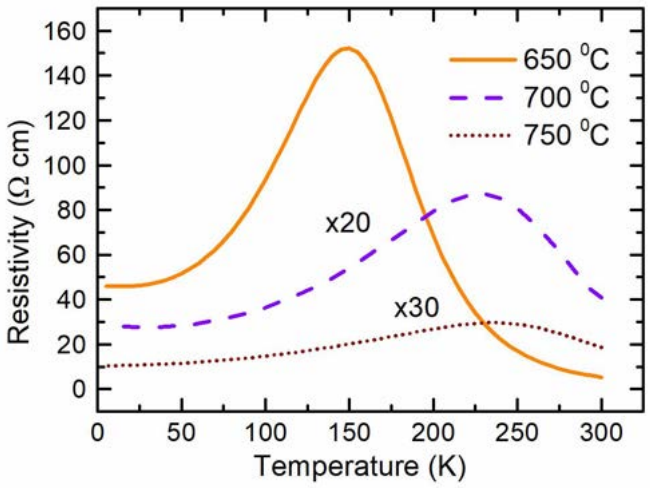

Figure 4.11: Resistivity (at 20 Tesla magnetic flux density) dependencies on temperature for films grown at different temperatures.

grown at higher T_{dep} and thus having less disordered structure show higher MR values at room temperatures ($\approx$ 290 K).

The table 4.2 shows summary of the parameters of samples from the second group. The best parameters are exhibited by the sample 2-4 grown at T_{dep} = 750 °C (the same as the sample 1-4); reduction or increase of deposition temperature has did not provide better characteristics. The subsequent sets of samples were grown to have ≈400 nm thicknesses at T_{dep} = 750 °C deposition temperature.

4.1.2.3 Magnetoresistance dependence on magnetic flux density

The dependencies of the MR on magnetic flux density are presented in Figure 4.13 when magnetic field is parallel to the film plane and the electrical current direction. The symbols show the experimental data.

The highest MR values at room temperature (T = 290 K) were obtained for films exhibiting the highest metal–insulator transition temperatures (films grown at T_{dep} = 750 °C and having thicknesses d>280 nm). Quite steep curves at 20 Tesla indicate, that, differently from structurally perfect LSMO materials with saturation of the magnetoresistance at ≈ 10–15 Tesla, magnetoresistance of the analyzed nanostructured LSMO films does not saturate even at 20 Tesla.

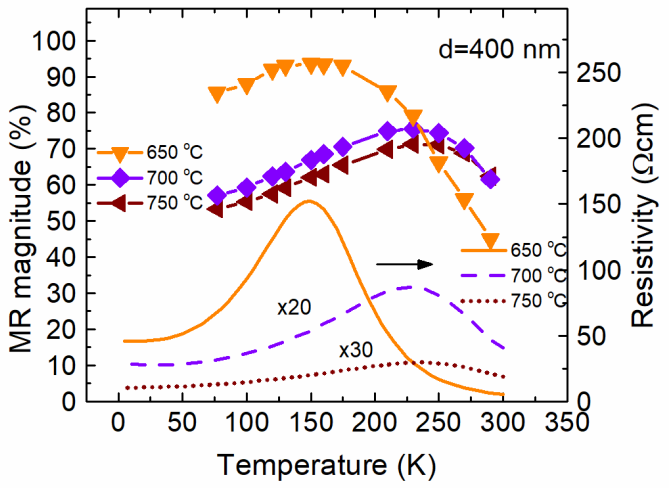

Figure 4.12: Resistivity and magnetoresistance dependencies on temperature for films grown at different temperatures at 20 Tesla magnetic flux density.

This is related to the effort needed to align Mn magnetic moments in Mn^{3+}-O-Mn^{4+} link: in disordered material, like grain boundaries, much higher magnetic field is needed for alignment of the magnetic moments than in epitaxial film.

Wagner et al. have demonstrated that the magnetoresistance of epitaxial films can be described using a modified Mott's hopping model [93]. According to this model, the MR in the ferromagnetic (FM) state shall to scale with the Brillouin function, $\mathcal{B}$, while in the Paramagnetic (PM) state it shall scale with $\mathcal{B}^2$. To adapt the model for nanostructured polycrystalline films, contributions of the crystallites and the grain boundaries as magnetic materials with reduced magnetization shall be taken into account [90]. As perpendicular to the substrate columnar crystallites are vertically separated by grain boundary "walls", electronically this system can be approximated as serial connection of crystallites (C) and grain boundaries (GB). Then the total magnetoresistance of the sample can be analyzed as a the sum of the two contributors, crystallites (C) and grain boundaries (GB). In the Ferromagnetic state magnetoresistance can be defined as:

$$MR = f \times A_C \times \mathcal{B}(x_C) + (1-f) \times A_{GB} \times \mathcal{B}(x_{GB}) + LFMR \qquad (4.1)$$

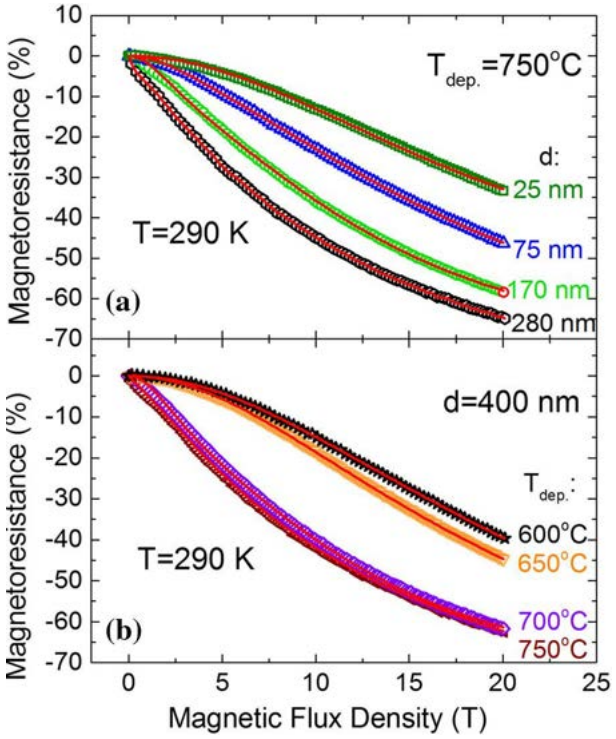

Figure 4.13: Magnetoresistance dependences on magnetic flux density.

and in the Paramagnetic state can be defined as:

$$MR = f \times A_C \times \mathcal{B}^2(x_C) + (1-f) \times A_{GB} \times \mathcal{B}^2(x_{GB}) \tag{4.2}$$

where f is the fraction of the crystallite-material , $(1-f)$ is the fraction of the grain boundary, $\mathcal{B}(x)$ is the Brillouin function, $x_{C(GB)} = g \times \mu_B \times J_{C(GB)} \times B/k_B T$ is the ratio of the magnetic and thermal energy, g is the Lande factor, $\mu_B$is the Bohr magneton, k_B the Boltzman constant, B the magnetic flux density, and T is the temperature. The magnetoresistance amplitudes A_C and A_{GB} as well as the spin–orbit quantum numbers J_C and J_{GB} are the fitting parameters. Low field magnetoresistance $(LFMR)$ is obtained from low-field measurements when the magnetic field is aligned parallel to the film plane.

For room temperature ($\approx$ 290 K) range, the MR was approximated with 4.2, because the films were in the Paramagnetic state.

For amorphous film (25 nm), good fitting results were obtained with fraction of crystalline material $f = 0$, meaning, that such thin film can be regarded as homogeneous amorphous (highly disordered) magnetic material. For thicker films, both contributors were taken into account.

The Curie temperature T_C of epitaxial films is close to T_m. Similar situation can be expected for crystallites (although the could be some mismatch because of ratios between dimensions of the crystallites, interfaces to grain boundaries), but grain boundaries are more disordered than even crystallites with distorted cells. Therefore, much lower temperature is required for transition from Paramagnetic to Ferromagnetic state of the grain boundary material. Combination of crystallites and grain boundary material drives metal–insulator transition temperature T_m of nanocrystalline LSMO down below Curie temperature T_C (which is above 290 K) and at room temperature mixture of states are present.

In the Figure 4.13 the thin solid (red) curves represent the fitting results both for the magnetoresistance of the films with different thicknesses (a) and the films grown at different temperatures (b).

For the thickest films, exhibiting the highest metal–insulator transition temperatures (T_{dep} = 750 °C, d = 280 and 400 nm), best fitting result was obtained by combining contributions of the paramagnetic 4.2 and the ferromagnetic 4.1 states (see Figure 4.13 solid line over symbols). This is an indication that in the metal–insulator transition temperature range the film has a mix of regions with Ferromagnetic and Paramagnetic states owing to the fact that highly ordered crystallites have different phase transition temperature (Curie temperature T_C) than disordered grain boundaries.

As an example, the fitting parameters for the LSMO films at T = 290 K (Figure 4.13) were in the following ranges: $f \times A_C = -(10 - 30)\%$, $(1 - f) \times A_{GB} = -(55 - 75)\%$, $J_C = 16 - 55$, $J_{GB} = 9 - 14$. The obtained J values were higher than the magnetic moment of single Mn ion - the indication that the crystallites and the grain boundaries in these films behave like a superparamagnet of magnetically aligned polarons [94, 95].

Besides analytical use, the above fitting parameters have a practical application in calibration of for B-scalar CMR sensors, manufactured from analyzed LSMO films: in cases when strength of the magnetic field generated in test laboratory is lower than the expected application of the sensor, the calibration curves can be extrapolated using Equations 4.1 and 4.2 to provide high accuracy calibration data for extended magnetic field strength range.

4.1.3 Magnetoresistance anisotropy

Magnetoresistance anisotropy along with magnetoresistance of the films dependencies on the thicknesses of the films in 0.7 Tesla magnetic field are presented in the Figure 4.14. The $MR_{\parallel}$ values obtained when the magnetic field was applied in-plane parallel or perpendicular to the current direction were very close. At low magnetic fields The $MRA$is mostly related to the magnitude of the demagnetization field caused by the geometry, in LSMO sample case "easy axis" is the axis that is much longer than the thickness of the film - i.e. in-plane direction between the contacts or across (see the Figure 3.6). The $MR_{\parallel}$ increases with the thickness of the films until 400 nm thickness, because diameters of the film crystallites increase with increase in thickness - thus contributing to the shape effect.

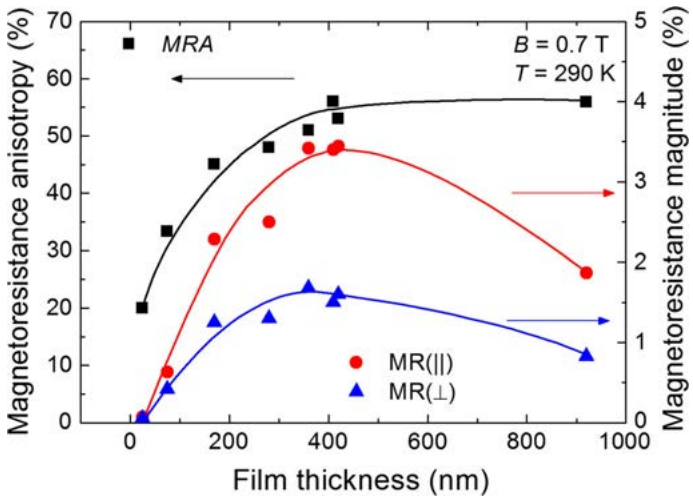

Figure 4.14: Magnetoresistance (right scale) and magnetoresistance anisotropy dependencies on the thicknesses of the films in low magnetic field (0.7 Tesla).

Since MRA value mainly depends on $MR_{\parallel}$, in selection of the film for production of the sensor, the trade-off between film sensitivity and accuracy in low magnetic field shall be evaluated: films which are most sensitive, especially in in-plane orientation (400 nm thick), at the same time have highest MRA.

The MRA decreases with increase in the magnetic field - down to about 1% at 20 Tesla - negligible error level in practical magnetic field measurement applications.

4.1.3.1 Summary

Thin $La_{1-x}Sr_xMnO_3$ manganite films deposited with the pulsed injection MOCVD technique onto glass-ceramics substrates exhibit macroscopic homogeneous structures, with characteristics strongly dependant on the deposition temperature and the film thickness.

- The $La_{1-x}Sr_xMnO_3$ films with thicknesses less than ≈25 nm consist mainly of the amorphous phase, while polycrystalline column- shaped microstructures are typical feature of the thicker films. These had average column widths of 40–65 nm, were spread throughout the whole thickness of the films, and were separated by 5–10 nm thick grain boundaries.
- The study of film's growth conditions influence on the colossal magnetoresistance effect in pulsed magnetic fields of up to 20 T shows the possibility to tune the characteristics of $La_{1-x}Sr_xMnO_3$ films to application requirements. For example thin films (thickness ≈25 nm) grown at 750°C or thick films (thickness ≈400 nm) grown at 600°C have a high magnetoresistance in the low temperature range (< 200 K). Meanwhile thick films grown at 750°C have high magnetoresistance at temperature above 250 K.
- The anisotropy of magnetoresistance of films also could be tuned by changing of growth conditions.

Thereby, the magnetoresistance and the anisotropy properties of the thin $La_{1-x}Sr_xMnO_3$ films can be tuned along a wide range by adjusting the fabrication conditions. This makes possible the development of magnetic field sensors with predetermined parameters. For room temperature application the nanostructured $La_{1-x}Sr_xMnO_3$ films grown at 750°C temperature and having thickness higher than 280 nm are preferable.

4.2 Films grown by varying Mn content on the Polycrystalline Al_2O_3 substrate

The purpose of the growth and analysis of the third group of samples was to investigate how the structure of the samples, electric and magnetoresistive properties are influenced by alteration of film composition: change of Mn content in the film. By adjusting deposition conditions, Mn content (Mn/(La+Sr) ratio) has been varied between 1.05 and 1.15.

This time the deposition was done on the Polycrystalline Al_2O_3, which has polycrystalline structure and is composed of good structural quality crystallites of approx. 2 μm dimensions. Following the conclusions drawn from the analysis of the first and the second groups of samples, the ≈400 nm thick samples were grown at 750 °C deposition temperature.

4.2.1 Morphology and structure of the deposited thin films

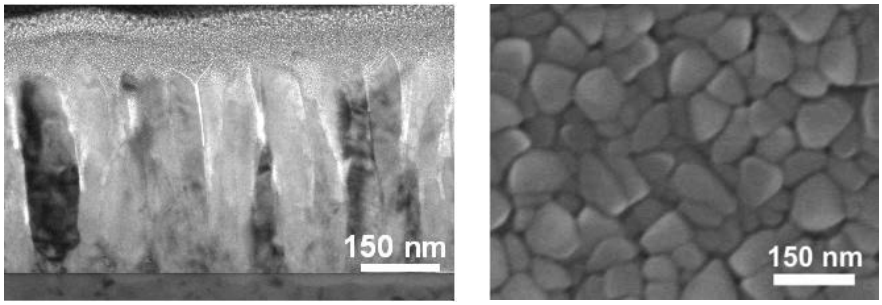

(a) (b)

Figure 4.15: TEM (a) and SEM (b) images of the films grown by varying Mn content increased by 15 %.

The morphology of the films from the third group, 400 nm thick grown at 750 °C temperature on the Polycrystalline Al_2O_3 substrate with Mn content (expressed by Mn/(La+Sr) ratio) set to 1.05 to 1.10 or 1.15 was similar to the morphology of 360 nm thick films grown at 750 °C. The film with Mn/(La+Sr)=1.15 has the grain structure of their surface densely packed without pinholes (see Figure 4.15 b) creating homogeneous film with quite complete coverage. The grains of the film had polygonal shapes with the average grain size ≈ 80 nm. The TEM images (see Figure 4.15 a) indicated the presence of column-shaped crystallites oriented perpendicular to the substrate and spread through the entire thickness of the films.

The D_{avg}=80 nm diameter of the crystallites of the third sample group (see Table 4.3), is on the larger end and supports the tendency of crytallite diameter increase with increase in film thickness.

Table 4.3: Main characteristics of the sample Set 3, composition $La_{0.83}Sr_{0.17}Mn_yO_{3\pm\delta}$, deposition temperature 750 °C, deposited on the Polycrystalline Al_2O_3 substrate.

Sample	T_m, K	ρ_m , Ωcm	d, nm	Mn/(La+Sr), y	D_{avg} , nm
3-1	240	0,475	400	1.05	80
3-2	250	0,37	400	1.10	80
3-3	270	0,25	400	1.15	80

4.2.2 Resistivity and Magnetoresistance analysis

The dependencies of resistivity versus temperature of the films with different Mn content are presented in Figure 4.16. The increase in Mn content (in Mn/(La+Sr) ratio from 1.05 to 1.10 and to 1.15) in LSMO films resulted in an increase of the metal–insulator transition temperature T_m from 240 K to 270 K and the simultaneous decrease in resistivity from 0.475 Ωcm to 0.25 Ωcm (dropping by substantial 47% in the same interval).

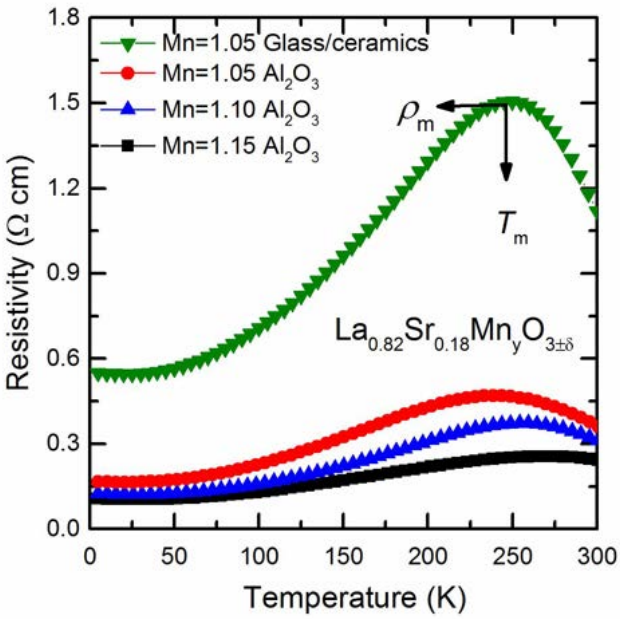

Figure 4.16: Resistivity dependence on temperature for the films grown with different Mn content.

The above changes can be explained in the following way. The doped colossal magnetoresistive (CMR) manganites have Mn ions with different valence, and the interplay between shares of Mn^{4+} and Mn^{3+} ions is responsible for magnetic interactions and related transport properties. Usually the Mn^{4+} / Mn^{3+} ratio is adjusted by varying the concentration of divalent Sr, Ca, or Ba doping ions [6, 96–98] and by forming structural defects, like Mn or La vacancies [99–104]. However similar effect can be achieved by facilitating relative Mn excess [99, 100] by creating La deficiency. Then some cell, which misses La^{3+} strips additional electron from Mn^{3+} and Mn^{4+} / Mn^{3+} ratio is increased. In other words, additional doping of $La_{0.82}Sr_{0.18}Mn_yO_3$ films with La vacancies leads to the optimal ratio of Mn^{4+} / Mn^{3+}, decrease in resistivity and increase in phase transition temperature.

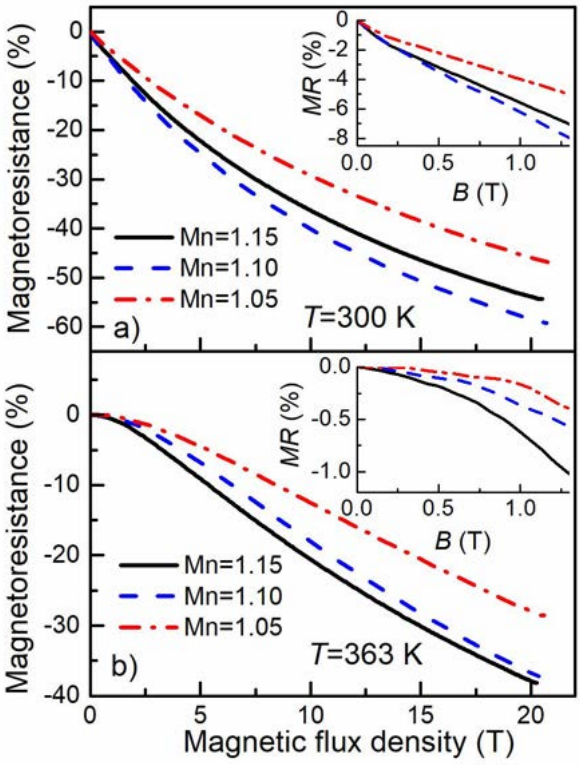

Figure 4.17: Magnetoresistance dependencies on magnetic flux density at temperature (a) 300 K and (b) 363 K for films having different Mn/(La + Sr) ratio. Insets present enlarged low-field region of these dependencies.

The magnetoresistance of the films was measured up to magnetic flux density B = 20 T at temperatures 77–363 K. The magnetoresistance magnitude dependences on magnetic flux density of these films at two ambient temperatures 300 and 363 K are presented in Figures 4.17 and 4.18. The films with close stoichiometric composition of Mn (1.05) have lowest magnetoresistance values. The increase in Mn concentration leads to the increase of magnetoresistance. At temperature T = 300 K the highest MR has the film grown with Mn excess of 10%, while at 363 K temperature the highest MR values are obtained for the film with Mn excess of 15%.

It has to be mentioned that the highest MR values for the latter film were observed at temperatures higher than 320 K. Moreover, it can be seen from the enlarged low-field regions (see insets in Figure 4.17) that at the highest measured temperature (363 K) the films with Mn concentration of 1.05 and 1.10 have very low sensitivity at magnetic flux density lower than 1 T (MR was only about 0.16% and 0.35% at 1 T, respectively), while for film with Mn excess of 15% the MR was 0.65% for the same magnetic field magnitude. Similar values were obtained by low-field measurements using the electromagnet. In strong magnetic fields of B = 20 T the MR values for the films with Mn excess of 10% and 15% achieved almost the same values.

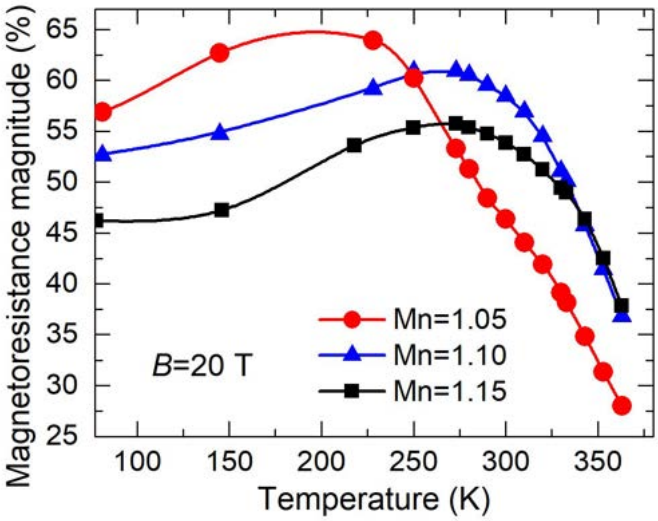

Figure 4.18: Magnetoresistance dependence on temperature for the films grown with varying Mn content. Measurements done at magnetic flux density B=20 Tesla.

The table 4.3 shows summary of the parameters of samples from the third group. The parameters best suited for room and above room sensor application are exhibited by the sample 3-3 grown on the Al_2O_3 substrate at T_{dep} = 750 °C with Mn content 1.15. There is a clear tendency that with the increase in Mn content T_m increases.

4.2.3 Summary

The study of the influence of Mn content in nanostructured $La_{1-x}Sr_xM_ynO_3$ films show that the electrical transport and magnetic properties of the the films strongly depend on Mn excess.

- The increase of the ratio Mn/(La + Sr) > 1, leads to the shift of the metal – insulator transition temperature T_m to higher temperatures and to decrease of the resistivity maximum ρ_m. For example, increase of Mn content from 1.05 up to 1.15 shifts the T_m by approximately 30°C. Although in this case, the magnetoresistance values decrease in the low temperature range (lower than T_m), at higher temperatures (above 320 K) the highest MR was obtained for films having the highest Mn excess of 1.15. The obtained results can be explained by the self-doping of La–Sr–Mn–O by La vacancies, which leads to more pronounced ferromagnetism in La–Sr–Mn–O and to the optimal ratio of Mn^{3+}/Mn^{4+}.
- The magnetic field sensors, fabricated from films with Mn excess of 15%, reveal higher sensitivity to the magnetic field in high temperature range. It was concluded, that increase of Mn content in La–Sr–Mn–O films allows to use them for the development of high pulsed magnetic field sensors operating at temperatures up to 360 K.

4.3 Films grown on different substrates

The purpose of the growth and analysis of the fourth group of samples was to investigate how the structure of the samples, electric and magnetoresistive properties are influenced by underlying substrate. The chosen substrates were monocrystalline AT-cut quartz, polycrystalline Al_2O_3 and amorphous Si/SiO_2-1000. Based on the tendency, that increase in Mn content drives up the temperature the maximum resistivity T_m, the MOCVD precursors were balanced to achieve ≈20% Mn content. Other conditions, deposition time to achieve close

to 400 nm film thickness and 750°C deposition temperature were, the same as in previous set of samples.

4.3.0.1 Morphology and structure of the deposited thin films

SEM images of the of 360 nm thick LSMO films (see Figure 4.19) depict surface morphology differences among the films grown on different substrates and the histogram in the Figure 4.20 shows quantitative distribution of the sizes of the crystallites. The crystallites grown on Quartz are the largest, with most probable width of 70 nm, and substantial share of crystallites reach almost 200 nm in width; majority of the crystallites formed in triangular shape while some formed polygonal-shape grains. The crystallites on polycrystalline Al_2O_3 substrate have most homogeneous dimensions with 14% of crystallites being 60 nm wide. The shares of trigonal and irregular crystal structure crystallites are about equal. Clusterization of the crystallites on Al_2O_3 substrate grains with preferential orientation is a distinctive feature of this film - see cluster of smaller trigonal crystallites in the bottom right part of the SEM image. The dimensions of crystallites on Si/SiO_2-1000 substrate are less homogeneous (with 12% of crystallites being 60 nm wide), but there irregular shaped crystallites dominate over trigonal system crystallites. The crystallite shape and size distribution over the picture area is random.

TEM images of the films show more differences between the films (see Figure 4.21). The first distinctive features in films on Quartz (40 nm thick) and Si/SiO_2-1000 (20 nm) substrates are intermediate thin gray layers between substrates and columns. Interestingly, there are dark spots in the intermediate region of the films grown on Quartz substrate- the high-resolution TEM images and Fast Fourier transformation (FFT) patterns (see Figure 4.22 a, c) show that these dark spots have crystalline structure surrounded by the amorphous medium.

Contrary, the light spots in the intermediate region of the films grown on Si/SiO_2-1000 consist only of the amorphous phase (see the high-resolution TEM images and Fast Fourier transformation patterns in Figure 4.22 b, d). Another distinctive feature of the film on Si/SiO_2-1000 substrate is presence of small crystallites clusters on the top of the gray layer (marked by dotted lines in Figure 4.21 c), these crystallites coalesce into larger size columns closer to the surface of the film.

The film grown on Al_2O_3 substrate has crystallite columns stemming right from the substrate throughout the whole film thickness with their long axis

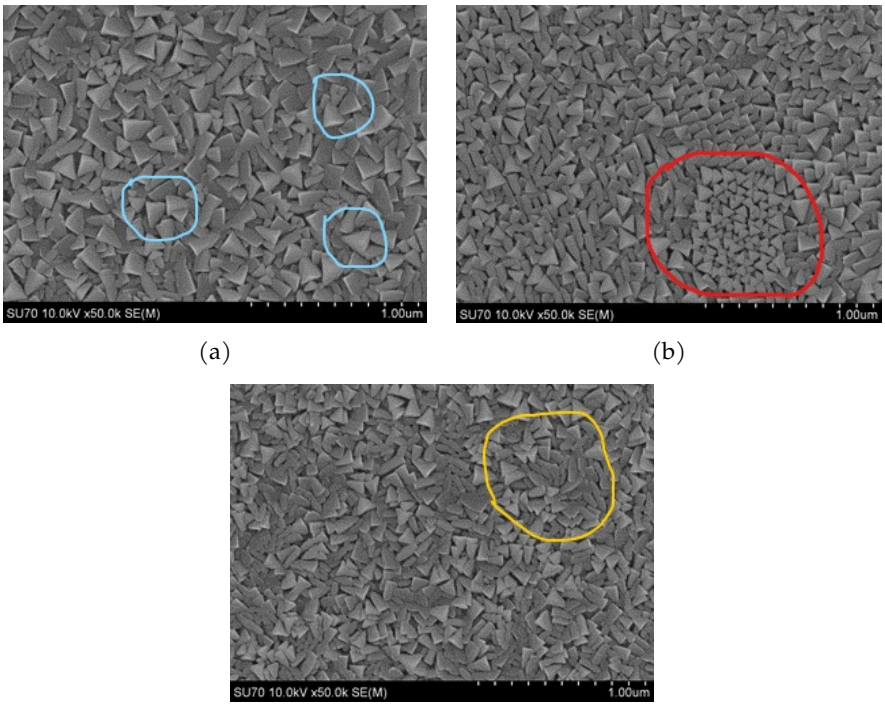

(a) (b)

(c)

Figure 4.19: SEM surface images of 360 nm thick LSMO films grown on different substrates: Quartz (a), polycrystalline Al_2O_3 (b) and Si/SiO_2-1000 substrates. Majory of the crystallites on Quartz show trigonal crystal systems (marked by blue line). The cluster of trigonal crystallites on polycrystalline Al_2O_3 (marked with red line) indicate growth on one Al_2O_3 grain. The large share of the crystallites with irregular shapes on the Si/SiO_2-1000 substrate (yellow line) indicate frequent twinning of the crystallites.

arranged perpendicular to the substrate. The columns on the Quartz substrate grow above intermediate layer while the columns on Si/SiO_2-1000 substrate start either above intermediate layer or reveal themselves above small crystallites clusters. The typical columns widths in all films are about and 20-50 nm at the bottom and 50–70 nm at the top.

SEM pictures of 60 nm thick films give insight about the growth of 360 nm films (see Figure 4.23): images of films on Quartz and on Si/SiO_2-1000 show 50-70 nm wide crystallites scattered among by much smaller (average size 25 nm) structures; these big crystallites can be related to the biggest columns of

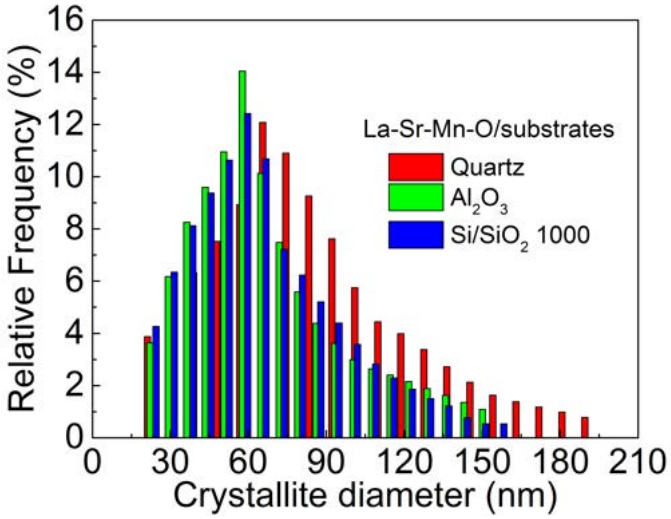

Figure 4.20: Distribution of crystallite dimensions for films on different substrates.

360 thick films (see SEM and TEM images). The density of big crystallites in thin film on Quartz is much higher- this than lead to higher share of large crystallites on 360 nm film. Contrary, the film on Al_2O_3 substrate consists of almost equally sized crystallites with average width of $\approx$ 35 nm and signs of clusterization islands.

The clusterization of crystallites on Al_2O_3 substrate is related to grains of the substrate (average grain size is 2 μm), varying crystal orientation between the Al_2O_3 grains dictates different orientation of nucleating LSMO cells and facilitates the growth of crystallites in clusters. This defines further growth of the film, some small grains growth in size faster and overshadow others leading to columnar growth with larger radius crystallites seen on thick films. On the contrary, films on amorphous Si/SiO_2-10002 start growing with small nucleation sites, small diameter crystallites grow up to half the thickness of 360 nm film, but then coalescence of crystallites leads to development of larger complex shape crystallites seen on SEM image of 360 nm thick film and broken grain boundary lines (see Figure 4.25 b).

To evaluate mutual diffusion of elements between the substrates and the films, initial surface position of the substrates in TEM images have been determined assuming the same average film growth rate on the Quartz and Si/SiO_2-1000 substrates. The initial surface position of the Si/SiO_2-1000 coincided with light

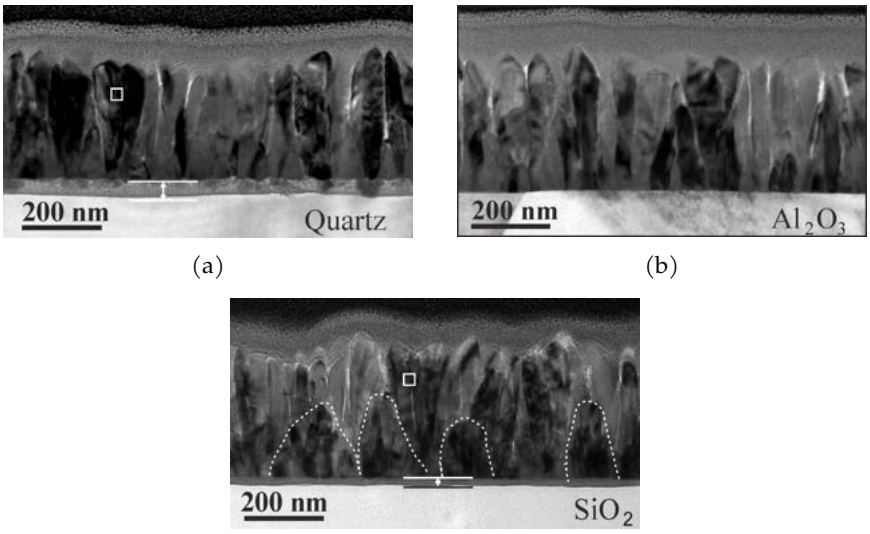

Figure 4.21: TEM images of 360 nm-thick LSMO films grown on different substrates: Quartz (a), polycrystalline Al_2O_3 (b) and $Si/SiO_2$2-1000 substrates.

spots in intermediate layer where Mn and La concentrations are at their minimums and Si concentration is at the maximum (see the Figure 4.24).

The TEM-EDS line profiles of the main chemical elements of the substrates and deposited films and cross-sectional STEM Z-contrast images of the films grown on Quartz and Si/SiO_2-1000 substrates (see the Figure 4.24) reveal the linkage between the substrates and the films.

Although the particular composition of elements somewhat differs between the samples, the tendencies of the depth profiles show diffusion of the elements of the films into the substrates.

There are several differences between diffusion layers on Quartz and Si/SiO_2-1000 substrates. First, the diffusion of the La and Mn into the substrate is deeper but with lower concentration in Quartz case. Second difference is in concentration of diffused atoms: while diffusion of Mn and La into Si/SiO_2-1000 is almost equal, the concentration Mn diffused into Quartz is double of La concentration. The third difference is thickness of intermediate layer- much thicker on Si/SiO_2-1000 substrates, probably because the small size LSMO grains on Si/SiO_2-1000 do not facilitate fast nucleation. Since grains grow faster in size on Quartz (see Figure 4.23 a), the intermediate layer on Quartz is

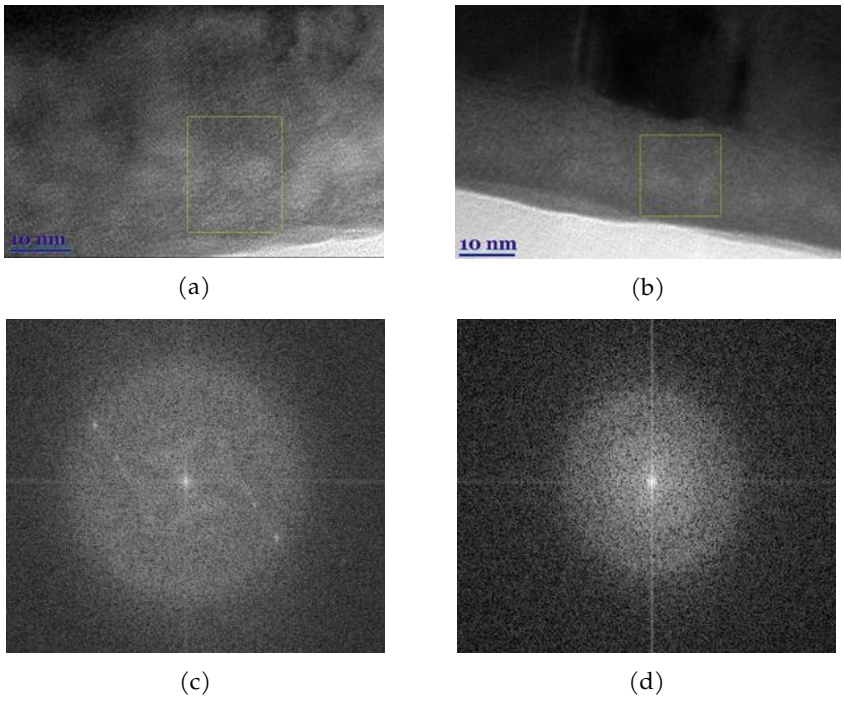

Figure 4.22: HR TEM image of an interface between the intermixed layer grown on Quartz (a) and SiO_2 (b) substrates and LSMO film, and Fast Fourier Transformation (FFT) patterns of the marked square area (c) and (d) respectively.

thicker but different: it resembles LSMO "gravel" in glass of Sr-Mn-La-O.

The TEM-EDS lines do not show evidence of Si being present in the bulk of the films, however, In-Bo Shim et al. [105] and Young-Min Kang et al. [106] have found that after annealing of LSMO film deposited on SiO_2 substrate, the Si was detected along all LSMO layer.

TEM-EDS analysis performed on LSMO film on Al_2O_3 substrate has not revealed diffusion of atoms between the film and the substrate.

Quality of the crystalline material of the crystallites and grain boundaries was evaluated from HRTEM images (see Figure 4.25) of the interfaces of two adjacent LSMO grains of the films grown on Quartz and Si/SiO_2-1000 substrates (positions of these segments are shown as squares in the Figure 4.22). In both cases there are seen narrow boundary regions separating LSMO grains with different crystalline orientation. The difference is in the shape of the line: the

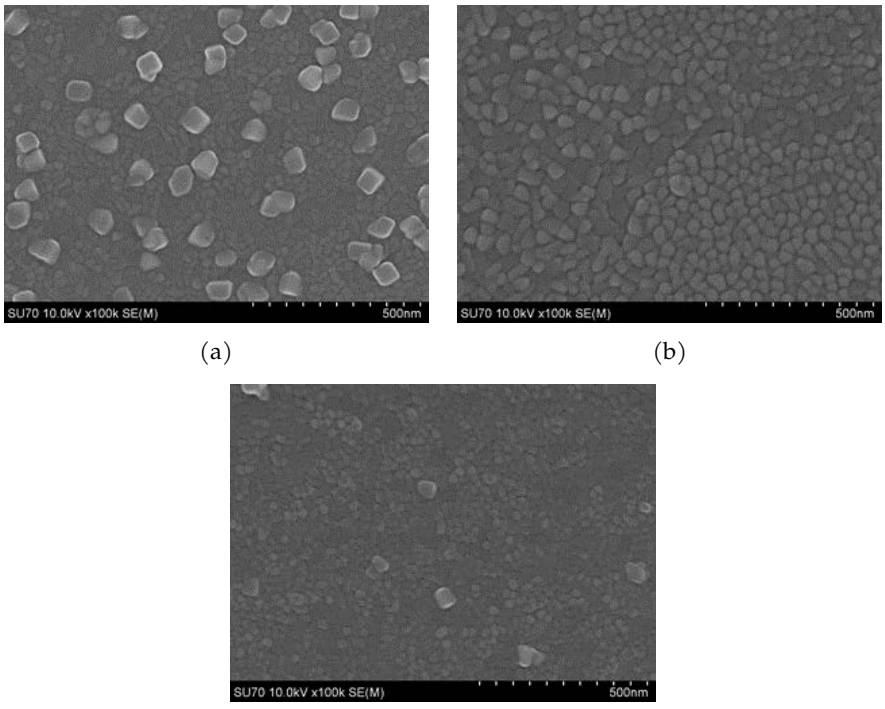

(a) (b)

(c)

Figure 4.23: SEM surface images of 60 nm-thick LSMO films grown on different substrates: Quartz (a), polycrystalline Al_2O_3 (b) and Si/SiO_2-1000 substrates.

border between the grains in the film grown on Quartz substrate is straight, about one nm wide, the two neighboring crystals are rotated only by few degrees one against another (Figure 4.25 a), while on the film grown on Si/SiO_2-1000 boundary between crystals have zigzag shape with about $2 \div 3$ nm width.

The low resolution TEM images of 60 nm thick films (Figure 4.26 a, b) show that the film on Quartz consists of monocrystalline grains with a clear faceted surface and amorphous layer, which was formed between SiO_2 and LSMO by the interfacial reaction. The thickness of this layer is about 6 nm. The "big" grains seen in the SEM images (see Figure 4.23 a) are crystals with orientation other than the rest of the film and with thickness about 80 nm. Films grown on Si/SiO_2-1000 substrate (see Figure 4.23 c) also contain separate crystals, however, width of these crystals is smaller and they do not have clear faced surface. The intermediate layer in this film is about 13 nm and contains light

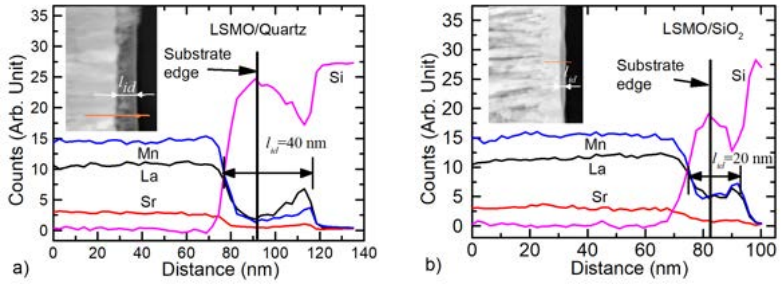

(a) (b)

Figure 4.24: TEM-EDS line profiles of the elements of the films (360 nm thickness) grown on Quartz (a) and Si/SiO_2-1000 (b) substrates. Insets – cross-sectional STEM Z-contrast image with marked scanning lines.

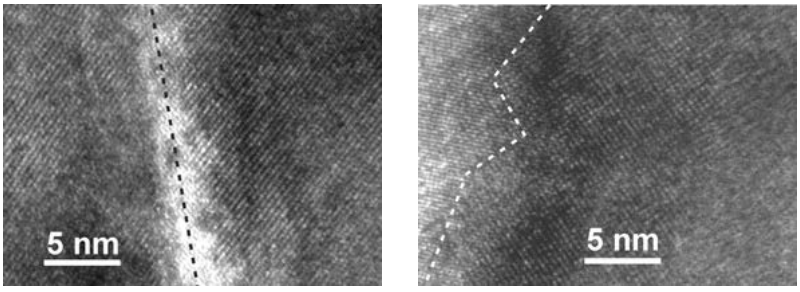

(a) (b)

Figure 4.25: TEM HR image of an interface between the two adjacent LSMO grains of films grown on Quartz (a) and Si/SiO_2-1000 (b) substrates.

spots as in 360 nm thick film.

4.3.1 Resistivity

The Figure 4.27 presents resistivity ρ of thin (60 nm) and thick (360 nm) LSMO films grown on Quartz, polycrystalline Al_2O_3 and Si/SiO_2-1000 substrates. All films exhibit a transition from metal-like to an insulator-like phase at specific temperature T_m (that are between 250 K and 285 K). However, maximum resistivities ρ_m of the films are scattered over the wide range signalling about variation in electrical transport properties of the films with different thicknesses and grown on different substrates (the T_m and ρ_m values are summarised in

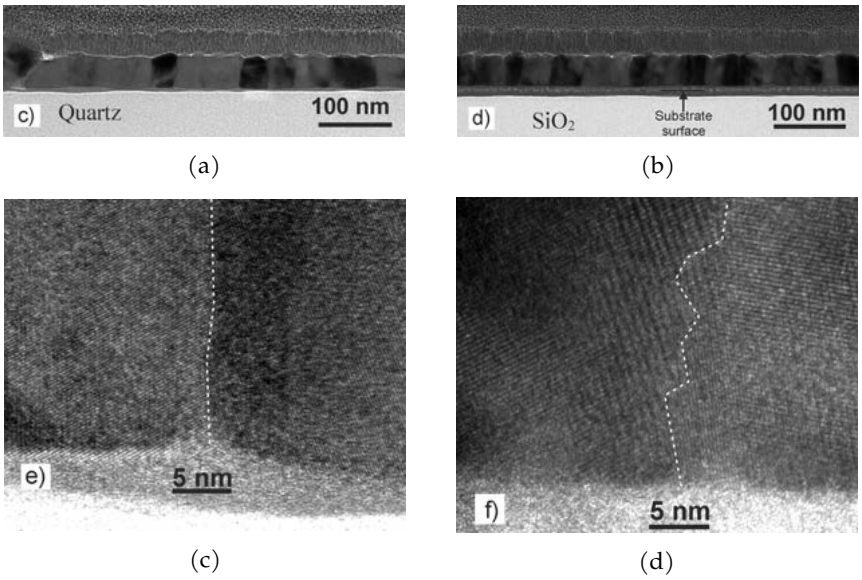

(a) (b)

(c) (d)

Figure 4.26: TEM images of films grown on Quartz (a) and Si/SiO_2-1000 (b). High-resolution SEM images of an interface between two adjacent LSMO grains ((c) - film on quartz, (d) – film on Si/SiO_2-1000). The dotted lines show the grain boundaries.

Table 4.4: Main characteristics of the sample Set 4, composition $La_{0.83}Sr_{0.12}Mn_{1.21}O_{3\pm\delta}$, substrate Polycrystalline Al_2O_3, deposition temperature 750 °C.

Sample	T_m**, K**	ρ_m**,** Ω **cm**	**d, nm**	**Substrate**	$\mathbf{D}_{avg}$**, nm**
4-1	285	0.445	360	Polycryst. Al_2O_3	58
4-2	225	1.68	60	Polycryst. Al_2O_3	35
4-3	260	1.05	360	Amorphous Si/SiO_2	60
4-4	245	1.54	60	Amorphous Si/SiO_2	25
4-5	285	0.5	360	Monocryst. Quartz	68
4-6	270	0.7	60	Monocryst. Quartz	25

Table 4.4).

First, the lower the metal-insulator transition temperature T_m and higher the maximal resistivity ρ_m of the thinner the film is related to microstructure of the films. The polycrystalline film could be imagined as a net of crystallites with perfect structure and disordered grain boundaries between them. The

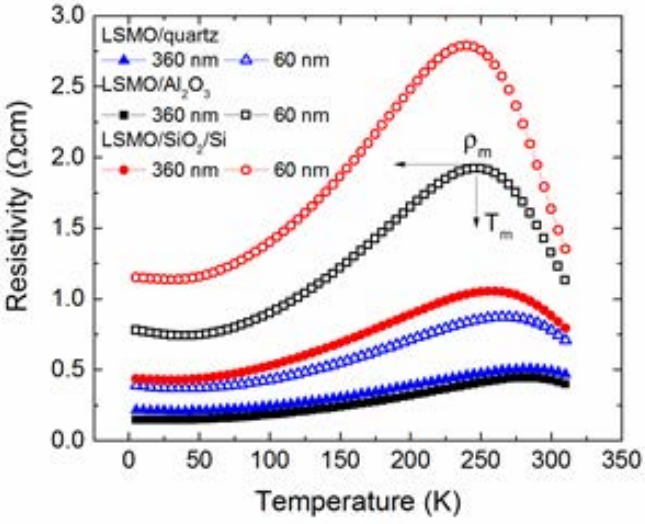

Figure 4.27: Resistivity vs. temperature dependences of LSMO films grown on Quartz, polycrystalline Al_2O_3 and Si/SiO_2-1000 substrates. The thicknesses of the films, d were 60 nm and 360 nm.

conducting mechanism in crystallites (like in monocrystalline doped manganites) is double exchange electron hoping between manganese ions: Mn^{3+}– O – Mn^{4+}, but the resistivity of whole polycrystalline films is mostly determined by the relative quantity of the grain boundary material and its properties. Depending on the level of disorder of grain boundaries and relative quantity of their material, the resistivity of the films can vary in a wide range.

The thinner films consist of smaller crystallites and have more disordered grain boundary material in the same volume as compared to thicker films. The thicker film of the same composition has larger crystallites, less grain boundary material and, consequently, lower resistivity. The films on different substrates have different ratios between resistivities of thin and thick films: for films on Al_2O_3 substrate resistivity of the thick film is 4.32 times lower than the resistivity of thin film, while for Quartz and Si/SiO_2-1000, respectively, 1.8 and 2.55. High resistivity differences mean, that there are significant structural differences occurring when the film thickness increases. The big difference in Al_2O_3 case and lowest (ρ_m =0.44 Ω cm) resistivity of thick film is explained by orderly crystallite columns with low volume of the disordered material in between in thick film compared to many small crystallites surrounded by dis-

ordered mass with misaligned magnetic moment in Mn^{3+}– O – Mn^{4+} links. Low resistivity of the thick film on Quartz is also explained by orderly columnar structure with low inter-grain content, the lowest resistivity of the thin film is attributed to grainy structure where percolation can take please between the closest grains. The highest resistivities of both films on Si/SiO_2-1000 substrate are attributed to most disorderly structures among the films grown on the three substrates (see TEM and SEM images) leading to high content of grain boundary material.

The films with thicker and more homogeneous crystallite columns (on monocrystalline Quartz), also have the highest insulator-metal transition temperature (T_m =285 K), because moderate decrease in temperature of the film is enough to contain vibrational motions of the atoms and enforce ferromagnetic ordering by aligning spins of Mn ions in Mn^{3+}– O – Mn^{4+} chains. Contrary, the lowest T_m was observed for films grown on amorphous Si/SiO_2-1000, because significant decrease in temperature is required ferromagnetic ordering of structurally disordered grain boundary regions.

Experiments with $La_{0.66}Sr_{0.34}MnO_3$ thin films deposited on single crystal cubic yttria-stabilized zirconia (YSZ) at 750°C have shown, that it is possible to move maximum resistivity temperature of LSMO closer to room temperature (see Figure 4.28) by allowing to form polycrystalline films on the crystal with different than LSMO lattice constant. However the obtained resistivity maximum temperature was only 240 K. This is too low for room temperature applications.

4.3.2 Low-field magnetoresistance

The magnetoresistance (MR) dependences on magnetic flux density B up to 0.75 T measured at different temperatures are presented in Figures 4.29 -4.31 for B parallel ($B \parallel$) and perpendicular ($B \perp$) to the film plane field configurations.

The main features of the MR are more pronounced at low temperatures. Figures 4.29 a, b and c show MR(B) dependence at 25 K. There is sharp peak of positive MR for $B \parallel$; the tip of this peak corresponds to the maximal resistance of the sample when concentrations of ions with parallel and antiparallel magnetic moments equalize. The magnetic field magnitude at the tip is gives the value of the coercive field of the sample.

Low-field magnetoresistance ($LFMR$) is an arbitrary value, because at low magnetic field magnetoresistance changes rapidly and the position of the in-

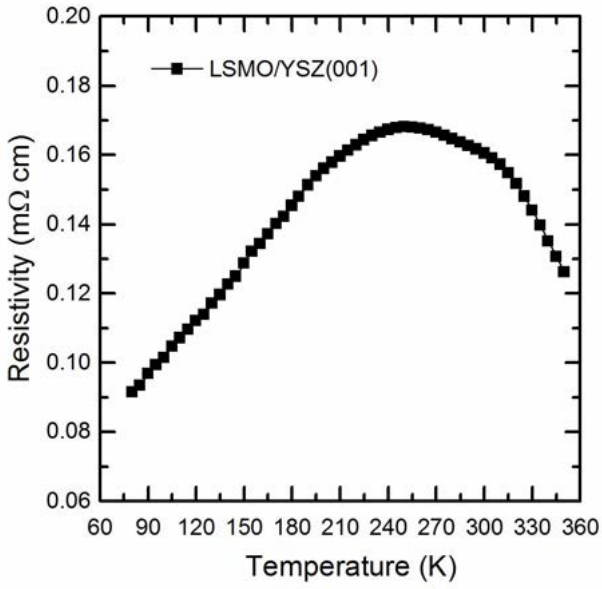

Figure 4.28: Resistivity dependence on temperature for $La_{0.66}Sr_{0.34}MnO_3$ thin films deposited on single crystal YSZ.

tersection of tangent to MR with B=0 axis (shown by arrow) very much depends on the selection of the point on MR curve. To avoid ambiguities, we have defined $LFMR$ as the value of MR at 0.7 Tesla magnetic field. The samples grown on Quartz have the highest $LFMR$ ($LFMR$=31% for 360 nm thick film and
$LFMR$=30% for 60 nm thick film) two times higher than $LFMR$ of samples on Si/SiO_2-1000 substrate ($LFMR$=15.5% for 360 nm thick film and $LFMR$=14.6% for 60 nm thick film) or on Al_2O_3 substrate ($LFMR$=15.4% for 360 nm thick film and $LFMR$=12.3% for 60 nm thick film). Hwang et al. [107] proposed to attribute the $LFMR$ in manganites to spin-polarized intergrain tunneling which usually is not observed in epitaxial films or monocrystalline manganites. The authors demonstrated that polycrystalline sample transport across grain boundaries is extremely sensitive to an applied magnetic field and is responsible for MR. Lee et al. [108] proposed that magnetoconductance MC, defined as

$$MC = 100\% \times \frac{\sigma(B) - \sigma(0)}{\sigma(0))} \tag{4.3}$$

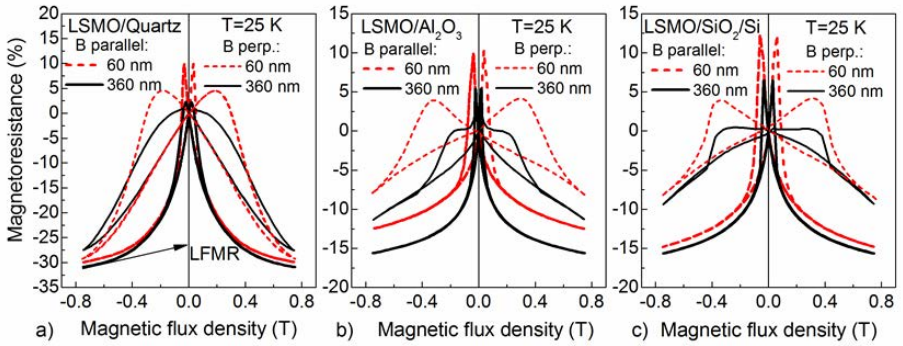

Figure 4.29: Low-field magnetoresistance dependences on magnetic flux density at 25 K temperature for 60 nm and 360 nm thick films grown on Quartz, Al_2O_3 and Si/SiO_2-1000 substrates.

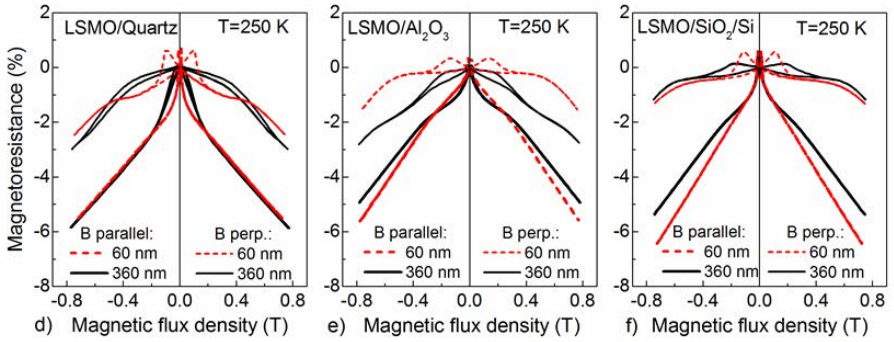

Figure 4.30: Low-field magnetoresistance dependences on magnetic flux density at 250 K temperature for 60 nm and 360 nm thick films grown on Quartz, Al_2O_3 and Si/SiO_2-1000 substrates.

where $\sigma(B)$ and $\sigma(0)$ are field and zero field conductivity, respectively) is limited by maximal value of 33.3%. However, the magnetoconductances of investigated samples on Qartz substrate, MC=44% for 360 nm film and 42% for 60 nm film (measured at 0.7 Tesla) exceed theoretical limit proposed by Lee et al.

In $B \perp$ case large (0.2 - 0.4 T) demagnetization fields can be partly attributed to geometric effect of sensor "magnet", because film thickness is much smaller than its length (distance between contacts is about 85 μm). However, demagnetization fields between samples of the same thickness but grown on different substrates differ up to 2 times. This difference can be attributed to magnetic

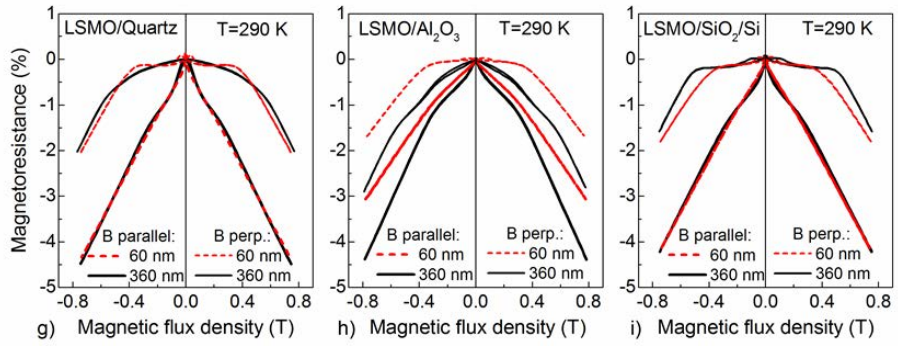

Figure 4.31: Low-field magnetoresistance dependences on magnetic flux density at 290 K temperature for 60 nm and 360 nm thick films grown on Quartz, Al_2O_3 and Si/SiO_2-1000 substrates.

domains. Since magnetic domain size in magnetic materials is in the range of 100 nm, the films with thinner crystallites (grown on Al_2O_3 and Si/SiO_2-1000 substrates, see Figure 4.20) will favor formation of high coercivity single domains, while films on Quartz with thicker crystallites will favor formation of low coercivity multi- domain configurations. As a result, demagnetization fields of the films on Quartz are much smaller than the demagnetization fields for the films with the same thickness on Al_2O_3 and Si/SiO_2-1000 substrates.

Experiments with $La_{0.66}Sr_{0.34}MnO_3$ thin films deposited on single crystal cubic yttria-stabilized zirconia (YSZ) at 750°C have shown, that these films exhibit small low field negative magnetoresistance in low magnetic fields (see Figure 4.32). These values (MR of 6-11 %) are lower in comparison with other investigated films grown on Glass-Ceramics, Quartz, Al_2O_3 and Si/SiO_2-1000 substrates.

4.3.3 High field magnetoresistance

Magnetoresistance dependences on magnetic flux density for 360 nm thick films grown on Glass-Ceramics, Quartz, Al_2O_3 and Si/SiO_2-1000 substrates are shown in Figure 4.33 (at ambient temperature T= 80 K) and in Figure 4.33 at ambient temperature T= 290 K. The figure show experimental data and approximation of the experimental data with Brillouin function.

The Figure 4.35 summarizes high field magnetoresistance measurements of the thin films from the fourth samples group.

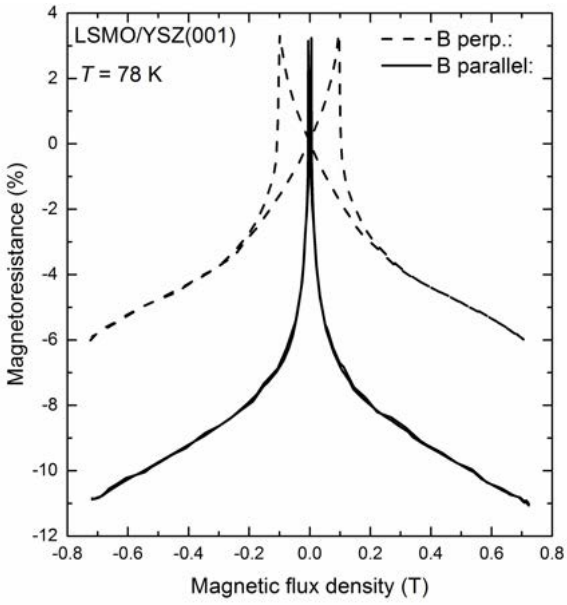

Figure 4.32: Magnetoresistance dependences on magnetic flux density for $La_{0.66}Sr_{0.34}MnO_3$ thin films deposited on single crystal YSZ.

The samples grown on Quartz exhibit highest magnetoresistance (26% .. 60%) both in low (B = 0.7 Tesla) and high (B = 20 Tesla) magnetic fields at low temperature (below 100 K) and high (but not highest) magnetoresistance ($\approx$ 60%)in high magnetic field at room temperature.The magnetoresistance in low magnetic field at room temperature is <7%. It shall be noted, that these samples have high T_m of 285 K, but at the same time the resistivity dependence on temperature is very shallow, especially for 360 nm thick sample. Such characteristics can be explained by advantageous balance between big crystallites of the film and plenty of disordered material with high Si content between them: while spins of atoms are easily aligned inside ordered crystallites, grain boundary material requires high magnetic force coupled with low temperature to align spins and change phase from paramagnetic to ferromagnetic. This conclusion is also supported by the low magnetoresistance in low magnetic field and quite high magnetoresistance in high magnetic field.

Samples on Si/SiO_2-1000 substrate exhibit highest ($> 60\%$) magnetoresistance in high ($B = 20$ Tesla) magnetic fields at room temperature, but only moderate magnetoresistance at low temperatures and low mgnetoresistance in low magnetic fields at room temperature. This can be explained by relatively small and

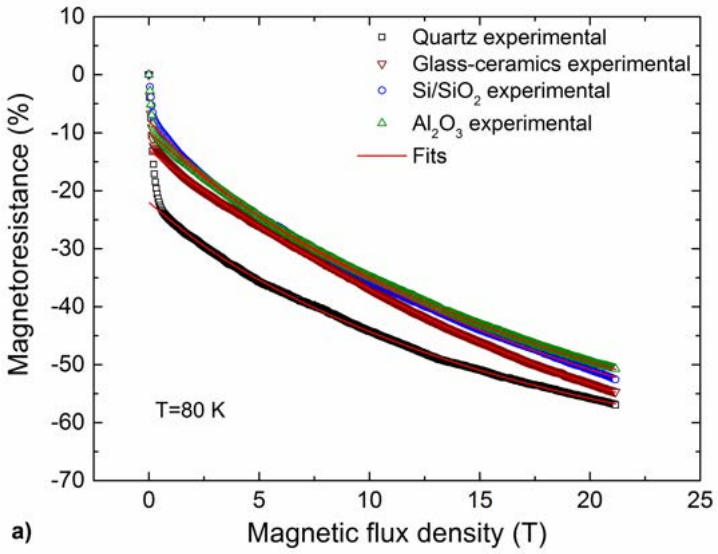

Figure 4.33: Magnetoresistance dependences on magnetic flux density at T= 80 K for 360 nm thick films grown on Glass-Ceramics, Quartz, Al_2O_3 and Si/SiO_2-1000 substrates.

hence densely packed crystallites with relatively small "high disorder" material volume in between. As mentioned above, small crystallites favour formation of single magnetic domains, which are difficult to reorient, hence there is high magnetoresistance at room temperature in high fields, but low magnetoresistance at low fields (not enough magnetic force to reorient single domain structures). In high magnetic fields, once by increase in magnetic field to a certain level magnetic moments in thin grain boundaries are aligned, magnetoresistance begins to decrease.

The magnetoresistance of the samples on Al_2O_3 substrate is very similar to magnetoresistance of the samples on Si/SiO_2-1000 substrate, with the difference that the high field magnetoresistance ($B = 20$ Tesla) is more level in wide temperature range. The later fact can be explained by absence of Si (because of different substrate) in grain boundaries and more homogeneous crystallite size distribution, making all material more homogeneous at micro level, thus facilitating more linear magnetoresistive characteristics.

The Table 4.5 and the Figure 4.36 summarize results of the Mn excess on film properties; there are included the films grown on Al_2O_3 substrate at 750°C

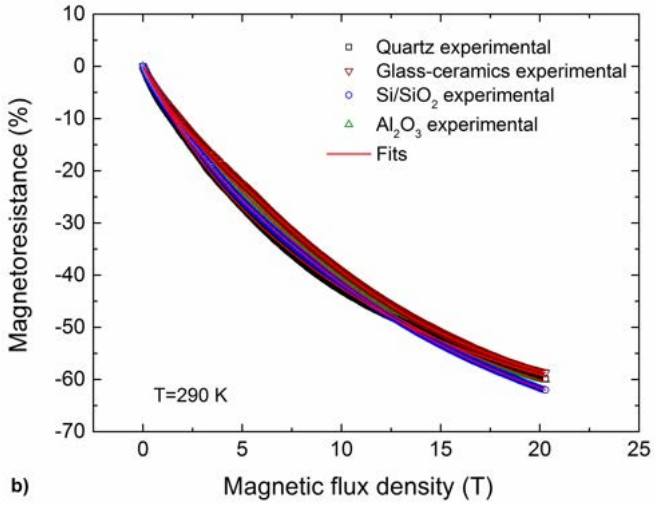

Figure 4.34: Magnetoresistance dependences on magnetic flux density at T= 290 K for 360 nm thick films grown on Glass-Ceramics, Quartz, Al_2O_3 and Si/SiO_2-1000 substrates.

temperature from Set 3 and Set 4. Correlation between Mn excess and the maximum resistivity temperature (Table 4.5) shows the tendency of the maximum resistivity temperature increases with increase in Mn content. Although the resistivity ρ_m decreases with Mn content increase from 1.05 to 1.15, it increases up to 0.445 Ωcm (sample 4-1) when Mn content is increased to 1.21. The later sample exhibits decrease in Sr content to 0.12 and decrease in most probable diameters of the crystallites to 58 nm.

Table 4.5: Summary of parameters of the films grown with Mn excess (composition $La_{0.83}Sr_xMn_yO_{3\pm\delta}$), deposition temperature 750 °C, deposited on the Polycrystalline Al_2O_3 substrate.

Sample	**Mn/(La+Sr), y**	**Sr, x**	T_m, **K**	ρ_m , Ωcm	**d, nm**	D_{avg} , **nm**
3-1	1.05	0.18	240	0.475	400	80
3-2	1.1	0.18	250	0.37	400	80
3-3	1.15	0.18	270	0.25	400	80
4-1	1.21	0.12	285	0.445	360	58

The Figure 4.36 a shows, that the samples with Mn content of 1.21 on all three

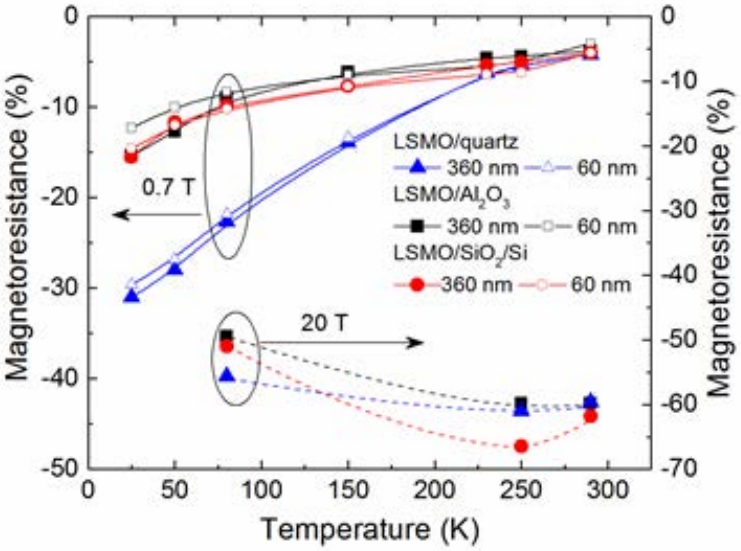

Figure 4.35: Magnetoresistance dependences on temperature at B= 0.7 Tesla (left scale) and B=20 Tesla (right scale) for 360 nm thick films grown on Quartz, Al_2O_3 and Si/SiO_2-1000 substrates.

substrates exhibit high magnetoresistance at above the room temperature and the LSMO on Al_2O_3 substrate have the best magnetoresistance in the magnetic flux density up 20 Tesla. The lines in the Figure 4.36 b point out, that all films with Mn content increased above close to stoichiometric 1.05 value (red line) exhibit substantially higher negative magnetoresistance. The best magnetoresistance at high (15-20 Tesla) magnetic flux density is exhibited by the film on Al_2O_3 substrate.

4.3.4 Magnetoresistance anisotropy

Low field magnetoresistance anisotropy figures of the 360 nm thick films grown on different substrates are shown in the Table 4.6. The sample on the polycrystalline Al_2O_3 has exhibited lowest MRA with MRA=34% at room temperature.

Magnetoresistance of $La_{0.9}Sr_{0.1}Mn_{1.21}O_3$ thin film deposited on Al_2O_3 substrate in up to 20 Tesla magnetic field at 290 K temperature is shown in the Figure 4.37. There is only slight mismatch between magnetoresistances in $B_{||}$

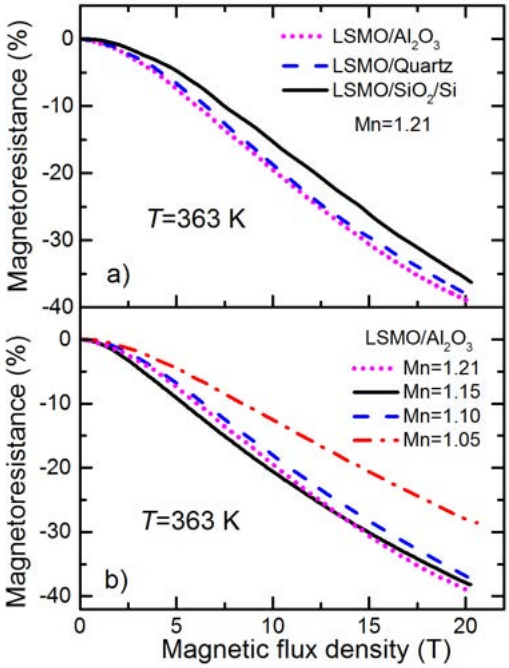

Figure 4.36: Magnetoresistance dependences on magnetic flux density at T= 363 K for 360 nm thick films grown on Quartz, Al_2O_3 and Si/SiO_2-1000 substrates with 1.21 Mn access (a), and for films grown on Al_2O_3 substrates with various Mn excess values.

and $B_\perp$ curves around 1 Tesla magnetic field, above this value the curves practically overlap. This confirms, that in high magnetic fields MRA of analyzed polycrystalline LSMO films is negligible.

4.3.5 Summary

The study of the characteristics of nanostructured $La_{1-x}Sr_xMnO_3$ films grown on different substrates shows the high influence of substrate type on the magnetoresistance of the film and its anisotropy at low magnetic field and at low temperature.

Films with thickness of 360 nm grown on monocrystalline Quartz have high low-field magnetoresistance (31 % at T=25K), while for films grown on polycrystalline Al_2O_3 and amorphous SiO_2 substrates this value was about 15.5

Table 4.6: $LFMR$ anisotropy of the 360 nm thick films grown on different substrates, measured at ambient temperatures $T = 25$ K, $T = 250$ K and $T =290$ K.

Substrate	Anisotropy, %		
	$T = 25$ K	$T = 250$ K	$T =290$ K
Quartz	14%	49%	55%
Polycrystalline Al_2O_3	28%	44%	34%
Si/SiO_2-1000	40%	77%	62%

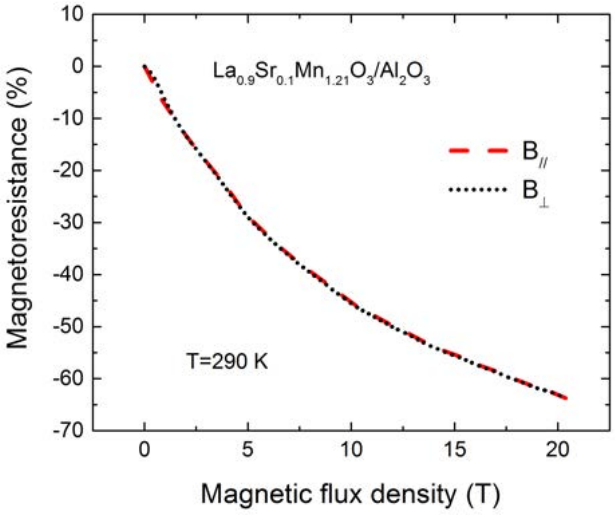

Figure 4.37: Magnetoresistance of $La_{0.9}Sr_{0.1}Mn_{1.21}O_3$ thin film deposited on Al_2O_3 substrate dependence on magnetic flux density in high magnetic field at 290 K temperature.

%. This can be caused by better structure of the films grown on Quartz with column-shaped crystallites spread through the film thickness and influence of inter-diffusive layer between the Quartz surface and the film. The high-field magnetoresistance values of nanostructured LSMO films grown on different substrates are similar. This is because the magnetoresistance of different quality crystallites obtained during deposition on different substrates has tendency of saturation in fields around 10 Tesla, therefore, higher fields (20 Tesla) affect almost grain boundaries, thus the magnetic ordering of Mn ions of these dis-

ordered regions has similar influence for all investigated films.

Increase in Mn content above stoichiometric level rises the temperature of the maximum resistivity T_m and increases magnetoresistnce of the films, especially in high magnetic field. The best negative magnetoresistance (38% at 20 Tesla magnetic flux density and 363 K ambient temperature) was exhibited by the LSMO film with Mn content of 1.21 deposited on the polycrystalline Al_2O_3 substrate.

The LSMO film with Mn content of 1.21 deposited on the polycrystalline Al_2O_3 substrate has lowest low field magnetoresistance anisotropy (34%) at room temperature and negligible magnetoresistance anisotropy in high magnetic field at room temperature.

4.4 Application of manganite based sensor for magnetic field measurements during Magnetic Pulse Welding

4.4.1 Preparation of the sensor

Selection of the CMR film for the sensor depends on the expected application. If measurements of the magnetic field would be at low (far below room) temperature, the LSMO on Quartz would be the best choice due to high magnetoresistance which does not saturate.

The Magnetic pulse welding application requires sensor, that can operate in wide range of the magnetic field - preferably form below 1 Tesla to 30 Tesla. Since the magnetic field changes during magnetic pulse - due to current and due to the movement of the parts, low anisotropy of the sensor is preferred.

The table 4.4 shows summary of the parameters of samples from the fourth group of samples.These requirements for the sensor are best fulfilled by sample 4-1 - the 360 nm thin LSMO film deposited on Al_2O_3 substrate at T_{dep} = 750 °C with Mn content 1.21.

The production of the sensor was done in following sequence:

1. Thin film deposition with PI MOCVD technology,
2. Photolitography of sensor mask,
3. Deposition of Cr adhesion layer,

4. Thermal deposition of silver (Ag) contacts,

5. Cutting of the substrate with film,

6. Soldering of cabling,

7. Passivation of the film surface,

8. Encapsulation into protective tube.

The cabled and packaged B-scalar sensor was tested in different magnetic fields (permanent, pulsed) and temperature ranges.

The Figure 4.38 shows the relative output voltage change ΔV across LSMO sensor versus magnetic flux density for two sensors with Mn concentration of 1.05 and 1.15 at two ambient temperatures. ΔV is expressed as

$$\Delta V = \frac{V_{out}(0) - V_{out}(B)}{V_{out}(0)} \tag{4.4}$$

where $V_{out}(B)$ and $V_{out}(0)$ are the output voltages with application of the magnetic field and without it, respectively.

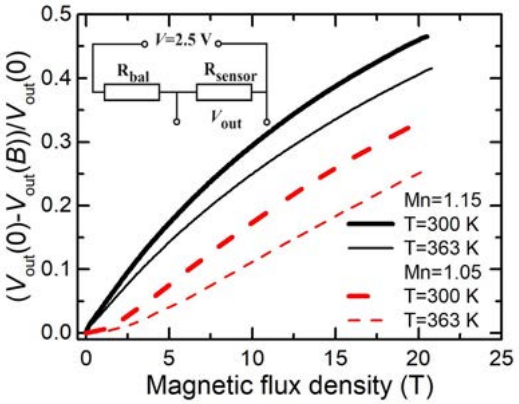

Figure 4.38: LSMO sensor's output (relative voltage change) versus magnetic flux density dependencies for sensors made with films having Mn content 1.15 and 1.05 at two temperatures: at 300 K (thick lines) and at 363 K (thin lines). Inset— electrical circuit of magnetic field sensor connection.

The sensor circuit consists of (see the Figure 4.39) the LSMO sensor, the twisted pair (TP) cable (see also the Figure 3.5) connecting the sensor to the measurement circuit, which is placed inside the magnetic field measurement unit

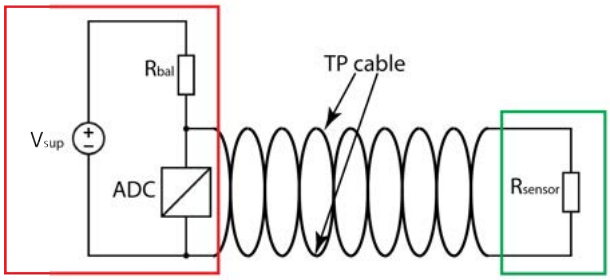

Figure 4.39: Principal parts of the sensor circuit. The part inside the green box is placed inside the induction coil and field shaper, the part in the red box is placed inside the magnetic field meter unit.

(red box in the Figure 4.39) consisting of principal parts - balance resistor R_{bal}, power source with voltage V_{sup} and analog digital converter ADC. The sensor (green box in the Figure 4.39), is placed in the narrow gap between the field shaper and the flyer, the TP cable is laid through the hole in the field shaper.

The measurement principle is based on the change in sensor resistance in the magnetic field (negative magnetoresistance). The ADC converts the voltage on the sensor R_{sensor} into digital value which is then compared with sensor calibration data (see the Figure 4.38) and magnetic flux density value B corresponding to the voltage on the sensor is recorded. Since the sensor is temperature sensitive, the voltage value at 0 Tesla magnetic flux density is used for selection of reference calibration curve.

4.4.2 Measurement of Magnetic Field Dynamics

The final part of the experimental work was testing of the sensor manufactured from the LSMO film deposited on Al_2O_3 substrate. Magnetic pulse welding application has been chosen because of several reasons:

- Magnetic Pulse Welding in industrial process, hence the sensor is tested in high innovation potential area;
- Magnetic Pulse Welding process is based on high amplitude (tens of Tesla) short duration magnetic pulses;
- There are technological challenges in measuring and monitoring transient processes taking place during compression and impact of welded

parts and application of CMR B-Scalar sensors is a novel method for solving the challenges.

The task has been split into steps:

- Measure magnetic pulses inside MPW machine's compression coil with several sets of welded parts and different magnetic pulse energies;
- Compare measurement results with theoretical simulations of the process;

The main objective of the task was to prove, that CMR B-scalar sensors can be used for in-situ monitoring magnetic pulse welding process and contribute to analysis about quality of the weld without destructive testing of the welded parts (see inset in the Figure 4.41).

Briefly, MPW process works like this: during rise magnetic pulse, magnetic pulse in the field shaper induces Eddy current in the flyer (moving part), Eddy current induces magnetic field, and the resulting magnetic field is a sum of both magnetic fields [109]. During the process, the flyer moves until meeting with the stationary part. Mechanical movements of the flyer and flap on the stationary part shall be reflected in the resulting magnetic field dynamics. Possibility to record these dynamics can provide valuable information about transient processed of magnetic pulse welding. High time resolution of the measurements will show specific "signatures" pointing to quality of welding process and helping to optimize pulse parameters and energy for efficiency improvement.

The application testing has been performed with CMR B-scalar sensors made from the 400 nm thick polycrystalline $La_{0.82}Sr_{0.12}Mn_{1.21}O_3$ film, deposited on the polycrystalline Al_2O_3 substrate. The probe was made as a flexible, 3 mm diameter and 1 m long screened cable with a $1\times0.5\times0.25$ mm^3 CMR-B-scalar sensor at its tip.

A set of experiments was performed to study the magnetic field dynamics in the gap between the field shaper and the aluminum flyer during MPW with a steel parent. In order to understand the peculiarities of the magnetic pulse shape, at first the following experiments were performed: 1) a rigid aluminum EN AW-6060 rod (outer diameter 40 mm) was used instead of a tube. 2) The free compression of the aluminum flyer tube was performed without a parent part.

The comparison of the magnetic flux density (B) oscillations during the experiments with the rigid rod and the free compression of the tube with a wall

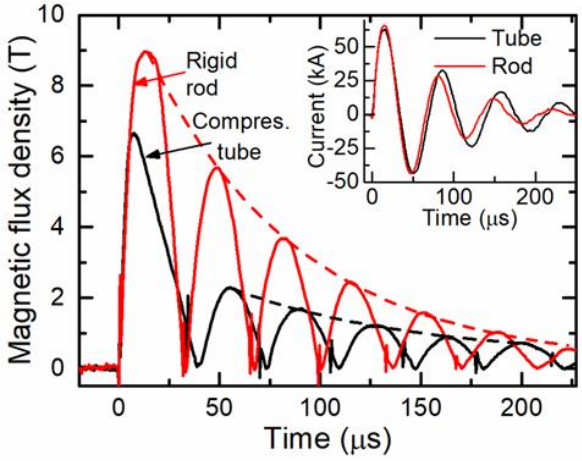

Figure 4.40: Magnetic field dynamics between the field shaper and the flyer part. Black line – 1.5 mm thickness Al tube; red line – rigid rod. Inset: the discharge current during tube compression – black line; rigid rod – red line.

thickness $d = 1.5$ mm is shown in Figure 4.40.

The process was like this: (1) the capacitor bank was charged up to $E = 4$ kJ, (2) the discharge of the capacitor through a coil created a damped alternating current in the coil. The damping effect is caused by internal resistance of the system, inducing damped and alternating magnetic field. As mentioned above, the CMR-B-scalar sensor measures the absolute value of the magnetic flux density B, so the graphs show the unipolar periodically changing magnetic field with decreasing amplitude. Further analysis is done on the unipolar magnetic field. In the first case (aluminum rod) the amplitude of all magnetic field oscillations changes according to a damping law (dashed line) with an exponential time constant $\tau = 75.5$ μs. However, in the case of tube compression, after the first half-wave pulse, the amplitude of the next half-wave is significantly decreased and the magnetic field oscillates according to the damping law with an exponential time constant $\tau = 90.7$ μs. This is due to the tube deformation during the first half-wave of the current, which causes a significant increase of the inductance of the system consisting of tube and field shaper. This conclusion is also confirmed by the decrease of the frequency of the magnetic field oscillations (see Figure 4.40).

Kleiner et al. [110] showed that when the flyer deformation starts, the total inductance of the consumer load (coil-tube) in the discharge circuit increases, which leads to the decrease of the oscillating current frequency and amplitude.

Due to the presence of the field shaper which is additionally used to the tool coil, the deformation of the tube only marginally affects the total inductance of the system (see [111]) and, consequently, the current in the coil changes only slightly (see inset in Figure 4.40). However, this leads to a significant decrease of the magnetic field amplitude in the gap between the field shaper and the compressed tube. Thus, in the system with the field shaper the only way to investigate the dynamics of the magnetic field in the gap between the shaper and the flyer is the direct measurement of the magnetic field by using magnetic sensors.

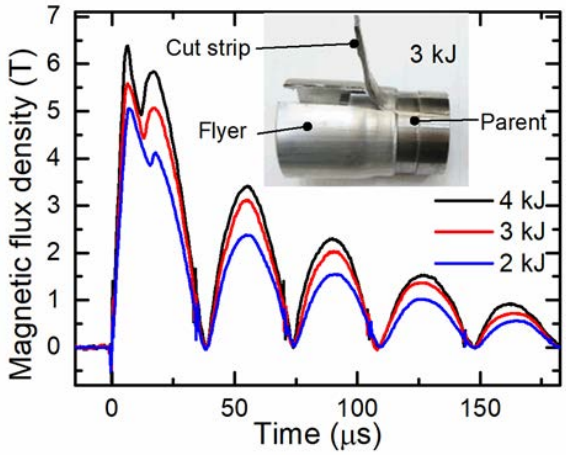

Figure 4.41: Magnetic field between the field shaper and aluminum flyer tube at different charging energies. Tube wall thickness – 1.5 mm, joining gap – 1.5 mm.

For the further study, the experiments of MPW of an aluminum flyer with a steel parent were performed at different charging energies E. The magnetic field oscillations during experiments at E = 2, 3 and 4 kJ are shown in Figure 4.41. The joining standoff between the parent and flyer was kept at 1.5 mm. One can see that the first half-wave in all welding experiments has two peaks. The first peak is similar to that observed during the free tube compression (see Figure 4.40). The amplitude of the peaks depends on the capacitor charging energy: the lower the charging energy, the lower is the amplitude of the magnetic field peak, and the maximum of these peaks is reached later. This difference, in comparison with the free compression experiments (see Figure 4.40), can be attributed to the influence of the parent. The magnetic inductance at the measuring point is the interference of the effect of the moving flyer

tube and the rigid parent. Therefore, there is the superposition of the magnetic field dynamics during free flyer compression and the experiments with a rigid workpiece. After the first peak is reached, the magnetic flux density drops to some local minimum value and then increases up to the second peak and then drops down to zero. Moreover, the minimum between these two peaks in time is achieved later and the relative value of the second peak is lower, the lower charging energy was used. After the end of the first half-wave, the next pulses are oscillating according to the damping law.

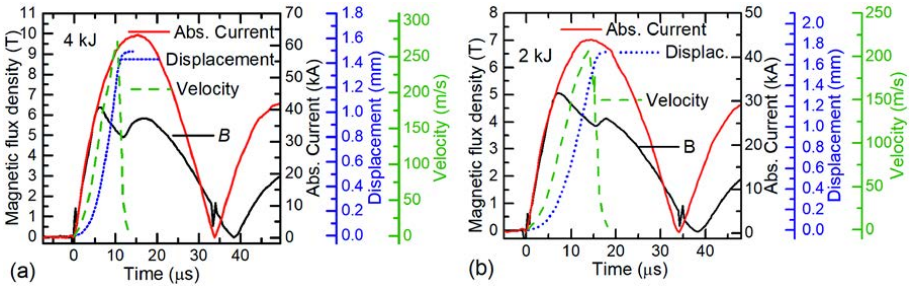

Figure 4.42: Magnetic field dynamic between the field shaper and Al tube – black line; Current of coil – red line; Displacement of the walls of tube – dotted blue line; Velocity of the tube wall – dashed green line. Tube walls thickness - 1.5 mm. Capacitor charging energy – 4 kJ (a) and 2 kJ (b). Parent material– steel.

To understand the dynamics of the magnetic flux density during the welding process, consider the processes that take place during the first half-wave of the discharge current. In the Figure 4.42 the change of the magnetic field between field shaper and flyer, the coil current, the flyer tube displacement as well as its deformation velocity are shown at charging energies of 4 kJ (Figure 4.42 a) and 2 kJ (Figure 4.42 b). The comparison of the flyer displacement over time and the magnetic flux density B waveform shows that the local minimum of B is reached at the collision of the flyer with the parent. At the instant of impact, the velocity of the flyer achieves its maximum value and then drops sharply. For $E = 4$ kJ (Figure 4.42 a), the initial collision time is 11 μs after the start of the current pulse and the maximum impact velocity of the flyer is $v_I = 272$ m/s. The total displacement of the flyer is 1.5 mm (i.e. the initial gap) and the deformation process is finished after 14 μs. One can see that the minimum of magnetic flux density is achieved when the flyer velocity decreases to vi = 120 m/s. As mentioned above, the first maximum and the subsequent decrease of magnetic field is a result of the flyer deformation caused by the magnetic

pressure. Due to action of this pressure, the flyer is accelerated until the impact with the parent. The decrease of the magnetic flux density is related with two opposing phenomena: the increase of the magnetic flux density due to the increase of the current in the field shaper and a decrease of B due to an increase of the system's inductance caused by the progressing deformation of the flyer. When the deformation velocity is decreased, the first process dominates and an overall increase of B is observed. Moreover, one can see that at the time instant of magnetic field minimum the current does not yet reach the maximum value and continues to grow, what results in the appearance of the second peak of the magnetic flux density.

The welding quality was tested by applying manual peel testing. The picture of the tested specimen after MPW at $E = 3$ kJ is shown in the inset of Figure 4.41. The cut strip of flyer material could not be separated from the parent, which indicates a good weld quality.

The same analysis can be performed for experiments at $E = 2$ kJ (see Figure 4.42 b). The main difference is that the minimum of B is reached after 15 μs. This is due to the lower flyer velocity (the impact velocity is $v_I = 205$ m/s) caused by a lower discharge current. Moreover, at the time when the flyer impacts the parent surface, the current has reached its maximum value and only a small increase of magnetic inductance takes place. The peel testing showed that at $E = 2$ kJ, an insufficient weld strength was obtained and the flyer strip could be easily peeled off the parent.

Therefore, by analyzing the waveform of the magnetic field over the time, one can qualitatively determine the quality of the MPW process taking into account the following parameters: time instant and amplitude of the first peak and time instant of the minimum. As stated before, the flyer deformation begins when a critical magnetic pressure is reached and the first maximum is a result of compensation of increasing magnetic field in the field shaper by decreasing magnetic field induced in the flyer. Therefore, as higher energy is applied to the coil, the greater speed of the flyer and the earlier time this maximum is achieved. The maximum magnetic pressure can be evaluated from this maximum value. Moreover, the position in time of the magnetic field minimum shows the time of the flyer impact with the parent. Based on the obtained data, one can determine the flyer velocity at the moment of collision with the parent. After the beginning of the deformation, the velocity of the flyer changes almost linearly. Knowing the joining gap and the time until impact, one can estimate the speed of the flyer; the later the local minimum is reached, the lower speed has the flyer during impact with the parent. Moreover, Lueg-Althoff et al. [112] showed that the time of impact of flyer with parent is a very important

parameter in the MPW process. The obtained test results can be used to monitor the welding process of materials. Of course, for various welding system setups (flyer wall thickness, flyer material, initial standoff, etc.), experimental tests must be carried out to attribute the corresponding shape of the magnetic field pulse to the welding quality.

The measurement results have been compared with numerical simulations performed at Institute of Forming Technology and Lightweight Components, TU Dortmund University, Germany. The 3D simulation models were created using the commercial software LS-DYNA. The comparison of the measured magnetic field dynamics and simulated magnetic field dynamics as well as measured coil current are presented in the Figure 4.43.

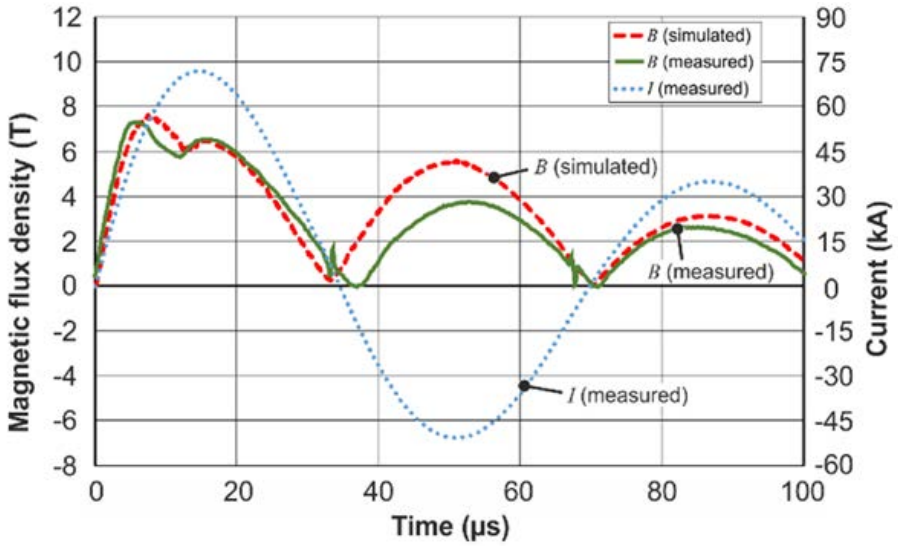

Figure 4.43: Magnetic field dynamics during the welding of an aluminum tube of wall thickness $d = 2$ mm with the steel parent. Scaled LS-DYNA simulation (scaling factor 0.3; red dashed line), measurement (green line) and current oscillations through the coil (blue dotted line).

The graph shows very good match between simulated and measured magnetic fields and means that the method of measuring the magnetic field dynamics between the tool (coil or field shaper) and the movable (flyer) workpiece during electromagnetic forming by with the CMR B-scalar sensor gives valuable information about the phenomena which take place during electromagnetic tube forming or MPW processes, e.g. at the instant of impact. The time of collision between the flyer and the parent can now be determined without the

use of elaborate measurement equipment like Photon Doppler Velocimeter or complex numerical simulations.

4.4.3 Summary

The designed CMR B-scalar magnetic field sensors based on nanostructured manganite films are capable to measure the magnetic field dynamics in the narrow gap between the field shaper and the moving workpiece during Electromagnetic Forming and Magnetic Pulse Welding (MPW) processes.

- CMR B-scalar sensors have ability to measure the magnitude of magnetic field independently of its direction - this allows for easier installation of the sensor at the measuring position, because it does not require an exact orientation with respect to the magnetic field direction.
- The CMR-B-scalar sensor is small and thus can be applied for the measuring of the magnetic field locally.
- Despite the fact that during MPW operation the temperature inside the welding tools increases above room temperature, the sensors based on LSMO thin film with Mn excess are able to accurately measure magnetic field.

Chapter 5

General Conclusions

1. Thin $La_{1-x}Sr_xMnO_3$ manganite films prepared by the pulsed injection MOCVD technique onto the glass-ceramics substrates exhibit macroscopically homogeneous structure, which strongly depends on the deposition temperature and the film thickness. Films whose thicknesses are not more than ≈25 nm consist mainly of the amorphous phase, while polycrystalline column- shaped microstructure is typical for the thicker films.

2. The study of nanostructured film's growth conditions influence on the peculiarities of the colossal magnetoresistance effect in pulsed magnetic fields up to 20 Tesla shows the possibility to tune the main parameters (resistivity, magnetoresistance and its anisotropy) of the films in a wide range of temperatures and magnetic fields and to satisfy the application requirements, thus enabling to develop magnetic field sensors with predetermined parameters. For room temperature sensors application the nanostructured La-Sr-Mn-O films grown at 750°C temperature and having thickness ≈400 nm are preferable.

3. The electrical transport and magnetic properties of nanostructured $La_{1-x}Sr_xMn_yO_3$ films strongly depend on Mn excess (y). The increase of the ratio $\frac{Mn}{La+Sr}$ from 1.05 to 1.21 leads to the shift of the metal–insulator transition temperature T_m to higher temperatures - from 240 K to 285 K. At temperatures higher than room temperature the highest MR values are obtained for films having the highest Mn excess of 1.15-1.21 (at 363 K MR ≈39%, when B=20 Tesla). The obtained results can be explained by the self-doping of La–Sr–Mn–O by La-vacancies, which lead to more

pronounced ferromagnetism in La–Sr–Mn–O and to the optimal ratio of Mn^{3+}/Mn^{4+}.

4. The choice of the substrate for deposition of the nanostructured $La_{1-x}Sr_xMn_yO_3$ manganite films has a great influence on the main parameters (resistivity, magnetoresistance and its anisotropy) of these films in ferromagnetic phase at low magnetic fields (<0.7 Tesla). Films with thickness of 360 nm grown on monocrystalline quartz have two times higher low-field magnetoresistance (31% at T=25K) in comparison with the films grown on polycrystalline Al_2O_3 and amorphous Si/SiO_2-1000 substrates ($LFMR$ ≈15.5%). This difference can be caused by more perfect structure of films grown on quartz with column-shaped crystallites spread through the whole film thickness and separated by thin grain boundary regions, and influence of interdiffusive layer formed at the quartz and manganite boundary.

5. The high-field magnetoresistance values of nanostructured LSMO films grown on different substrates are similar. This could be explained by taking into account that high field influences mainly magnetic ordering of Mn ions in disordered grain boundary regions, while magnetic ordering (magnetoresistance) of different quality crystallites obtained during deposition on different substrates, has tendency of saturation in fields around 10 Tesla. Therefore, application of higher fields (20 Tesla) have similar influence on magnetoresistance of films grown on different substrates.

6. The designed magnetic field sensors based on the nanostructured $La_{1-x}Sr_xMn_yO_3$ manganite films with Mn excess are capable to measure the magnetic field dynamics locally in narrow gap between the field shaper and the movable workpiece during electromagnetic forming and welding (MPW) processes.

Santrauka lietuvių kalba

1 Įvadas

Darbo aktualumas ir problemos formulavimas

Polikristaliniai manganitų sluoksniai turi išskirtines milžiniškos magnetovaržos (Angl. Colossal Magnetoresistance - CMR) savybes. Dėl šių išskirtinių savybių jie gali būti pritaikomi labai stiprių magnetinių laukų (dešimčių Teslų) matavimui ir naudojami specialios paskirties magnetinio lauko matuokliuose.

Iš polikristalinių nanostruktūrizuotų $La_{1-x}Sr_xMnO_3$ (LSMO) sluoksnių pagaminti jutikliai matuoja absoliutų magnetinės indukcijos dydį; dėl šios savybės pavadinti *B-skaliariniais CMR jutikliais* [113]. LSMO sluoksniai šiems jutikliams gaminami impulsiniu-injekciniu metaloorganinių junginių cheminio nusodinimo iš garų fazės (PI MOCVD) būdu. Dėl manganitų medžiagos savybių šie jutikliai nėra universalūs visiems temperatūrų ir magnetinių laukų diapazonams; konkretiems praktiniams pritaikymams reikia pagaminti sluoksnius, kurių varžos pokytis būtų pakankamai reikšmingas, kad būtų galima atlikti matavimus, pavyzdžiui, nuo 200 mTeslų iki 2 Teslų arba nuo 2 Teslų iki 40 Teslų ruožuose pageidaujamame temperatūros diapazone (pavyzdžiui, nuo 5 °C iki 50 °C).

LSMO sluoksniai yra perspektyvūs kuriant *stipraus impulsinio* magnetinio lauko matuoklius [2]. Buvo nustatyta, kad LSMO sluoksniai gali būti panaudoti keleto milisekundžių trukmės magnetinių impulsų magnetinės indukcijos absoliutinės vertės matavimams [10, 85, 114]. Pagrindiniais reikalavimais impulsinio magnetinio lauko jutikliams, sukurtiems iš manganitų sluoksnių yra reikalavimas jų jautrumui plačiame magnetinių laukų ruože (0,1 – 100 T) ir didelė sparta (dešimčių kHz dažnių ruožas). Todėl svarbu išsiaiškinti,

kaip polikristalinių manganitų sluoksnių cheminė sudėtis, auginimo temperatūra, storis, padėklo tipai ir nehomogeniška struktūra lemia magnetovaržos dydį (jutiklio jautrumą) plačiame temperatūrų ir magnetinių laukų ruože.

Tyrimų objektas

Darbo tyrimų objektas – nanostruktūrizuoti manganitų sluoksniai.

Darbo tikslas

Pagrindinis šio darbo tikslas yra ištirti galimybes derinti $La_{1-x}Sr_xMn_yO_3$ sluoksnių magnetovaržines savybes plačiuose temperatūrų ir magnetinių laukų ruožuose keičiant technologines sluoksnių auginimo sąlygas ir padėklus bei ištirti galimybę matuoti metalų magnetinio impulsinio suvirinimo magnetinio lauko dinamiką.

Darbo uždaviniai

Darbo tikslui pasiekti buvo sprendžiami tokie uždaviniai:

1. Ištirti La-Sr-MnO sluoksnių, užaugintų ant stiklo keramikos padėklų magnetovaržos priklausomybę nuo sluoksnių storio ir sluosnių auginimo temperatūros.
2. Ištirti La-Sr-MnO sluoksnių, užaugintų ant polikristalinių Al_2O_3 padėklų magnetovaržos priklausomybę nuo Mn pertekliaus.
3. Ištirti La-Sr-MnO sluoksnių magnetovaržos priklausomybę nuo auginimo padėklų.
4. Ištirti jutiklių, pagamintų iš La-Sr-MnO sluoksnių pritaikymo galimybes magnetinio impulsinio suvirinimo įrenginuose.

Darbo mokslinis naujumas

- Atliktas išsamus $La_{1-x}Sr_xMnO_3$ manganitų sluoksnių, užaugintų impulsinio - injekcinio metaloorganinių junginių cheminio nusodinimo iš garų fazės būdu (PI MOCVD) ant stiklo keramikos padėklų, magnetovaržinių savybių tyrimas plačiame temperatūrų ir magnetinių laukų

ruože ir nustatytos galimybės jas valdyti ir keisti, priklausomai nuo sluoksnių nusodinimo temperatūros ir storio. Buvo nustatyta, kad ant stiklo keramikos užauginti sluoksniai pasižymi kolonine mikrostruktūra, kuri lemia sluoksnių savitąją varžą, magnetovaržą ir jos anizotropiją.

- Gauta, kad LSMO sluoksniai, plonesni nei 25 nm, užauginti ant stiklo keramikos padėklų, sudaryti daugiausia iš amorfinės fazės, tuo tarpu storesniems sluoksniams būdinga koloninės formos kristalitų mikrostruktūra. Taip pat buvo nustatyta, kad padėklo parinkimas turi didelę įtaką nanostruktūrizuotų $La_{1-x}Sr_xMn_yO_3$ sluoksnių silpno lauko ($<$0.7 T) magnetovaržinėms savybėms feromagnetinėje fazėje, tuo tarpu paramagnetinėje fazėje padėklo įtaka magnetovaržos vertėms nežymi, o didesnis padėklo poveikis pasireiškia magnetovaržos anizotropijai dėl demagnetizacijos lauko.

- Parodyta, kad pasirinkus AT-pjūvio monokristalinio kvarco padėklą, galima pasiekti silpno lauko magnetovaržos vertes, dvigubai didesnes nei sluoksniams ant polikristalinio Al_2O_3 ir amorfinio Si/SiO_2-1000 padėklų. Buvo pademonstruota, kad Mn kiekio perteklius $La_{1-x}Sr_xMn_yO_3$ sluoksniuose leidžia padidinti jų virsmo metalas- izoliatorius temperatūrą $\approx$45 laipsniais ir padidinti magnetovaržos vertes temperatūrose, didesnėse nei kambario temperatūra.

Darbo rezultatų praktinė reikšmė

Gauti rezultatai leido panaudoti LSMO sluoksnius su Mn pertekliumi spartaus stipraus magnetinio lauko jutiklio sukūrimui, kuris pasižymi tokiomis išskirtinėmis savybėmis, kaip maži matmenys, padidėjęs veikimo temperatūros ruožas, didelis jautrumas aukštesnėje nei kambario temperatūroje ir maža anizotropija. Toks jutiklis buvo panaudotas lokaliems magnetinio lauko dinamikos matavimams sparčių elektromagnetinio metalų formavimo ir magnetinio impulsinio metalų suvirinimo procesų metu.

Disertacijos ginamieji teiginiai

1. Nanostruktūrizuotų $La_{1-x}Sr_xMnO_3$ manganitų sluoksnių, užaugintų impulsinio - injekcinio MOCVD būdu ant stiklo keramikos padėklų, metalo-puslaidininkio virsmo temperatūra T_m ir stipraus lauko maksimalios magnetovaržos vertės temperatūra gali būti valdomos plačiame temperatūrų ruože (130 K – 240 K), keičiant sluoksnių storį ir nusodinimo

temperatūrą, išlaikant tą pačią cheminę sudėtį. ≈400 nm storio sluoksniai, užauginti 750°C temperatūroje, yra tinkamiausi kambario temperatūros taikymams dėl didžiausios magnetovaržos šiame temperatūrų ruože.

2. Silpno lauko (<0.7 T) magnetovarža nanostruktūrizuotų $La_{1-x}Sr_xMnO_3$ sluoksnių feromagnetinėje fazėje žymiai padidėja, naudojant sluoksnių nusodinimui monokristalinį AT-pjūvio padėklą, palyginus su polikristaliniu Al_2O_3 ir amorfiniu Si/SiO_2-1000 padėklais, dėl susidariusio tarpdifuzinio sluoksnio manganito - padėklo riboje ir tvarkingos struktūros kristalitų, atskirtų plonomis tarpkristalitinėmis sritimis susiformavimo. Paramagnetinėje fazėje padėklo įtaka silpno lauko magnetovaržai yra nedidelė.

3. Mn pertekliaus y padidinimas nuo 1.05 iki 1.21 nanostruktūrizuotuose $La_{1-x}Sr_xMnO_3$ manganitų sluoksniuose sąlygoja jų metalo-izoliatoriaus virsmo temperatūros T_m padidėjimą ne mažiau kaip 45 laipsniais (nuo 240 K iki 285 K), dėl to padidėja magnetovaržos vertės aukštesnėse nei kambario temperatūrose.

4. Magnetinio lauko jutikliai iš nanostruktūrizuotų $La_{1-x}Sr_xMn_yO_3$ sluoksnių, su Mn pertekliumi y>0.10, užaugintų ant Al_2O_3 padėklo, pasižymi tokiomis išskirtinėmis savybėmis, kaip maži matmenys, padidėjęs veikimo temperatūros ruožas, didelis jautrumas aukštesnėje nei kambario temperatūroje ir maža anizotropija, o tai leidžia juos panaudoti lokaliems magnetinio lauko dinamikos matavimams sparčių elektromagnetinio metalų formavimo ir magnetinio impulsinio metalų suvirinimo procesų metu.

Darbo rezultatų aprobavimas

Disertacijos tema yra atspausdinti keturi moksliniai straipsniai žurnaluose, įtrauktuose į *Thomson Reuters Web of Science* duomenų bazę, ir atspausdintas vienas straipsnis tarptautinių konferencijų medžiagoje.

Disertacijoje atliktų mokslinių tyrimų rezultatai buvo pristatyti penkiose mokslinėse konferencijose užsienyje:

- 15th XMR-Symposium "Magnetoresistive Sensors and Magnetic Systems", Wetzlar, Vokietija, kovo 19-20, 2019. Kviestinis pranešimas.

- 7th Euro-Asian pulsed power conference EAPPC & BEAMS 2018, Changsha, China, September 16-20, 2018.
- Collaborative Conference on Materials Research CCMR2017, Jeju, South Korea, birželio 26-30, 2017.
- 14th Symposium „Magnetoresistive Sensors and Magnetic Systems“, Wetzlar, Vokietija, kovo 21-22, 2017.
- 6th Euro-Asian Pulsed Power Conf. / 21th Intern. Conf. on High-Power Particle Beams / 15th International Conference on megagauss magnetic field generation and related topics, Estoril, Portugalija, rugsėjo 18-22, 2016.

Autoriaus įnašas

Disertaciniame darbe pateikti rezultatai, jų analizė ir išvados buvo gauti autoriui bendradarbiaujant su publikacijų, pateiktų autoriaus publikacijų sąraše, bendraautoriais. Disertacijos autorius atliko La-Sr-Mn-O sluoksnių elektrinio laidumo ir magnetovaržos matavimus silpnuose ir stipriuose magnetiniuose laukuose, atliko didelės indukcijos ričių magnetinio lauko pasiskirstymo matavimus su CMR jutikliais *Pulsolution GMBH* įmonėje Šveicarijoje, kartu su kolegomis atliko magnetinio lauko dinamikos matavimus magnetinio impulsinio suvirinimo įrenginyje Dortmundo Technologijos universiteto Formavimo technologijų ir Lengvųjų Komponentų institute (Vokietija), vykdė magnetinio impulsinio suvirinimo įrenginio, naudojamo magnetinių jutiklių bandymams, konstravimą Valstybiniame mokslinių tyrimų institute Fizinių ir technologijos mokslų centre.

Disertacijos struktūra

Disertaciją sudaro įvadas, trys pagrindiniai skyriai, bendrosios išvados ir cituojamos literatūros bei autoriaus publikacijų sąrašas. Įvade pristatoma problema ir tyrimų objektas, iškeliami darbo tikslai ir uždaviniai, pateikiami darbo naujumo kriterijai ir praktinė vertė, pristatomi ginamieji teiginiai. Po įvado seka literatūros apžvalga disertacijos tematika. Apžvalgoje aptariamos bendrosios tiriamų medžiagų fizikinės savybes bei pasaulinėje literatūroje sutinkami jų aprašymo metodai. Trečiame skyriuje pristatoma tyrimo metodika bei darbe naudotų bandinių gaminimo technologijos bei pagrindinės jų savybės. Ketvirtame skyriuje aptariami rezultatai- augintų sluoksnių morfologija, savitasis

laidumas, magnetovarža bei CMR sluoksnių bandymai matuojant magnetinio lauko impulsus magnetinio impulsinio metalų suvirinimo įrenginyje. Disertacijos pabaigoje pateikiamos bendrosios išvados ir naudotos literatūros sąrašas.

2 Bandinių paruošimas ir tyrimų metodika

Nanostruktūrizuoti $La_{1-x}Sr_xMn_yO_3$ (LSMO) sluoksniai buvo užauginti Valstybiniame mokslinių tyrimų institute Fizinių ir technologijos mokslų centre. Bandiniai buvo auginti keliomis serijomis:

- Bandiniai ant stiklo keramikos padėklų auginti impulsinio-injekcinio metaloorganinių junginių cheminio nusodinimo iš garų fazės būdu (PI MOCVD) būdu:
  - Skirtingo storio sluoksniai (keičiant auginimo laiką),
  - $\approx$ 400 nm sluoksniai keičiant auginimo temperatūrą.
- Bandiniai ant polikristalinių Al_2O_3 padėklų užauginti impulsinio - injekcinio metaloorganinių junginių cheminio nusodinimo iš garų fazės (PI MOCVD) būdu, keičiant Mn koncentraciją.
- Bandiniai ant skirtingų padėklų - AT pjūvio kristalinio kvarco, polikristalinio Al_2O_3 ir amorfinio Si/SiO_2-1000 - auginti PI MOCVD būdu. Bandiniai ant YSZ padėklų auginti magnetroninio dulkinimo būdu.

Pagrindiniai užaugintų sluoksnių parametrai pateikti 2.1-2.4 lentelėse. Kristalitų skersmenys apskčiuoti naudojantis *ImageJ* Java atviro kodo programa. Dėl skirtingos kristalitų formos tekste naudojamas išvestinis dydis - kristalito skersmuo d, apskaičiuotas pagal formulę $d = \sqrt{\frac{4S}{\pi}}$, kur S - kristalito plotas SEM vaizde. Terminu *vidutinis kristalitų skersmuo* D_{vid} vadinamas labiausiai tikėtinas kristalito dydis, kuris apskaičiuotas naudojantis *ImageJ* programa.

Atlikus 1-os serijos bandinių tyrimus, sekančiai bandinių serijai buvo pasirinkta auginti $\approx$400 nm storo sluoksnius.

Atlikus 2-os serijos bandinių tyrimus, sekančiai bandinių serijai buvo pasirinkta auginti $\approx$400 nm storio sluoksnius 750°C temperatūroje.

Atlikus 3-čios serijos bandinių tyrimus, sekančiai bandinių serijai buvo pasirinkta auginti $\approx$ 400 nm storio sluoksnius 750°C temperatūroje su 21% mangano pertekliumi.

Lentelė 2.1: Pagrindiniai 1-mos serijos bandinių parametrai (bandinių sudėtis $La_{0,83}Sr_{0,17}MnO_{3\pm\delta}$, kur $y = 1$, auginti ant stiklo keramikos padėklų 750 °C temperatūroje).

Bandinys	**T$_m$, K**	**ρ_m , Ω cm**	**d, nm**
1-1	130	135	25
1-2	172	12	75
1-3	220	3,4	170
1-4	235	1,0	400
1-5	220	1,5	900

Lentelė 2.2: Pagrindiniai 2-os serijos bandinių parametrai (bandinių sudėtis $La_{0,83}Sr_{0,17}MnO_{3\pm\delta}$, $y = 1$, auginti ant stiklo keramikos padėklų iki d=400 nm storio.

Bandinys	**T$_{dep}$, °C**	**T$_m$, K**	**ρ_m , Ω cm**
2-2	650	150	152
2-3	700	225	4,4
2-4	750	235	1,0

Savitosios varžos ir varžos kitimo magnetiniame lauke matavimams ant bandinių $50\ \mu m$ atstumu, uždėjus ploną (3-5 nm storio) Cr tarpsluoksnį buvo suformuota po du Ag elektrodus, prie kurių prilituoti vytos poros laidininkai (2.1 ir 2.2 pav.).

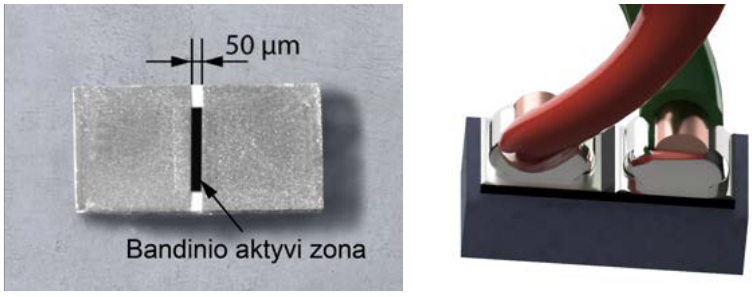

(a) (b)

Pav. 2.1: (a) Suformuoto jutiklio (bandinio) su kontaktinėmis plokštelėmis nuotrauka, (b) 3D jutiklio su prilituotais laidininkais modelis.

LSMO sluoksnių varža plačiame temperatūros ruože buvo matuojama naudojant uždaro ciklo helio kriostatą, o magnetovarža silpname lauke

Lentelė 2.3: Pagrindiniai 3-čios serijos bandinių parametrai (sudėtis $La_{0,82}Sr_{0,18}Mn_yO_{3\pm\delta}$, auginti 750 °C temperatūroje ant polikristalinių Al_2O_3 padėklų).

Bandinys	**T_m, K**	**ρ_m , Ωcm**	**d, nm**	**Mn/(La+Sr), y**	**D_{vid} , nm**
3-1	240	0,475	400	1,05	80
3-2	250	0,37	400	1,1	80
3-3	270	0,25	400	1,15	80

Lentelė 2.4: Pagrindiniai 4-tos serijos bandinių parametrai (sudėtis $La_{0,9}Sr_{0,1}Mn_{1,21}O_{3\pm\delta}$, auginti ant polikristalinio Al_2O_3 padėklų, auginimo temperatūra 750 °C).

Bandinys	**T_m, K**	**ρ_m , Ω cm**	**d, nm**	**Padėklas**	**D_{vid}, nm**
4-1	285	0,445	360	polikrist. Al_2O_3	58
4-2	225	1,68	60	polikrist. Al_2O_3	35
4-3	260	1,05	360	amorfinis Si/SiO_2	60
4-4	245	1,54	60	amorfinis Si/SiO_2	25
4-5	285	0,5	360	monokrist. kvarcas	68
4-6	270	0,7	60	monokrist. kvarcas	25

plačiame temperatūros ruože buvo matuojama papildomai naudojant nuolatinio magnetinio lauko generatorių (elektromagnetą). Siekiant tuo pačiu įvertinti magnetovaržos anizotropiją, matavimai atlikti bandinius orientuojant dviem kryptimis magnetinio lauko atžvilgiu: magnetiniu lauku statmenu bandinio plokštumai ir magnetiniu lauku nukreiptu išilgai bandinio plokštumos. Magnetovarža buvo skaičiuojama pagal formulę:

$$MR = \frac{R(B) - R(0)}{R(0)} \times 100\%, \tag{2.1}$$

kur $R(B)$ - bandinio varža magnetiniame lauke, o $R(0)$ – bandinio varža be magnetinio lauko.

Manganitų sluoksnių magnetovaržos tyrimams stipriame magnetiniame lauke buvo naudojamas stiprių impulsinių magnetinių laukų generatorius sudarytas iš (2.3 pav.): 1) aukštos pastovios įtampos šaltinio skirto kondensatorių įkrovimui, 2) aukštos įtampos kondensatorių baterijos, 3) didelės galios tiristorinio jungiklio, 4) šarvu sustiprintos indukcinės ritės, 5) įtampos matavimo bloko, 6) nuotolinio valdymo bloko, 7) magnetinio lauko matuoklio [82].

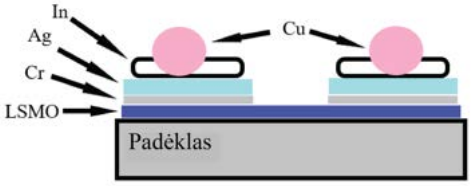

Pav. 2.2: Suformuoto jutiklio (bandinio) su kontaktinėmis plokštelėmis ir prilituotais laidininkais schematinis skerspjūvis.

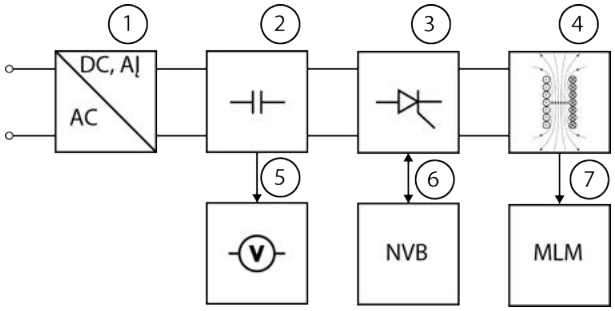

Pav. 2.3: Stiprių magnetinių laukų generatoriaus blokinė schema.

Matavimai magnetinio impulsinio metalų suvirinimo metu buvo atlikti Dortmundo Formavimo Technologijų ir Lengvųjų Komponentų Institute (Institute of Forming Technology and Lightweight Components of TU Dortmund University).

Esminiai sistemos komponentai buvo: didelės galios impulsų generatorius (*Poynting* SMU 0612 FS), indukcinė suspaudimo ritė (*Poynting* SMU-K97-8/90 8 vijų ritė, vidinis skersmuo 48,5 mm, ilgis 91,6 mm), magnetinio lauko formuotuvas - koncentratorius (išorinis ilgis 110 mm koncentravimo zonos ilgis 15 mm ir bandiniai - strypai ir vamzdžiai [83]. Principinė magnetinio impulsinio suvirinimo eksperimento komponentų jungimo schema ir schematinis ritės su joje sumontuotais elementais pjūvis parodyti 2.4 pav.

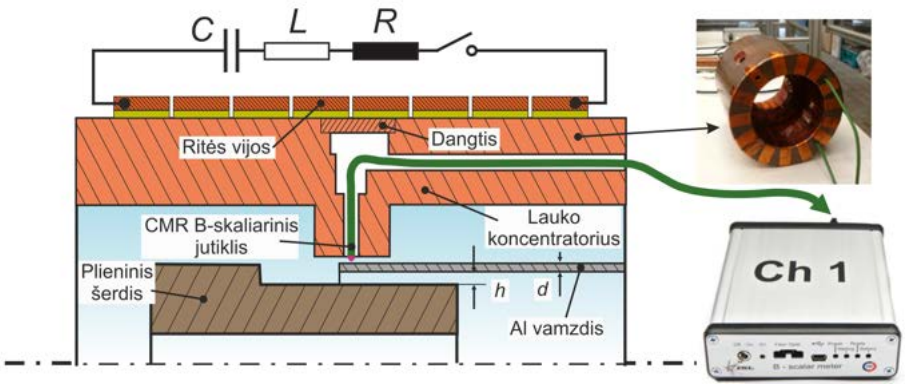

Pav. 2.4: Kairėje: principinė magnetinio impulsinio suvirinimo eksperimento komponentų jungimo schema suvirinant apvalius komponentus. Dešinėje viršuje - lauko formuotuvas su CMR jutikliu, dešinėje apačioje - magnetinio lauko matuoklis [4].

3 Tyrimų rezultatai

3.1 Ant stiklo keramikos auginti LSMO sluoksniai

3.1.1 Tyrimai

Sluoksnių mikrostruktūros tyrimas buvo atliktas analizuojant sluoksnių TEM ir SEM vaizdus. Ploniausių 25 nm storio sluoksnių mažo didinimo skersiniai TEM vaizdai parodyti 3.1 a ir b pav. Dviejų 25 nm segmentų, paimtų iš to paties sluoksio, kristalų struktūra skiriasi: (a) segmentas primena amorfinį sluoksnį, o (b) segmentas rodo granuliuotą struktūrą. Storesnių, 75 ir 170 nm sluoksnių skersiniai TEM vaizdai (pav. 3.1 atitinkamai c ir d) rodo kolonos formos kristalitus, kurių plotis (skersmuo) d yra 40 iki 65 nm. Kolonos vertikaliai driekiasi per visą sluoksnio storį, jų ilgoji ašis orientuota beveik statmenai padėklui. Kristalitus skiria 5–10 nm storio tarpkritalitinės sritys, užimančios visą tarpą tarp jų. Kolonų TEM vaizdų kontrastas rodo, kad kai kurie kristalitai yra ne vientisi, o susideda iš kelių kristalitų (suaugusių dvynių).

Auginimo skirtingose temperatūrose metu gauti bandiniai turi skirtingas paviršių morfologijas ir smarkiai besiskiriančias kristalines struktūras. Pav. 3.2 rodomi sluoksnių, užaugintų 600°C (a, b), 650°C (c, d), 700°C (e, f) ir 750°C (g, h) TEM ir SEM vaizdai. Sluoksnių skerspjūvio TEM vaizdai rodo koloninę struktūrą su būdingu 30–60 nm kristalitų diametru.

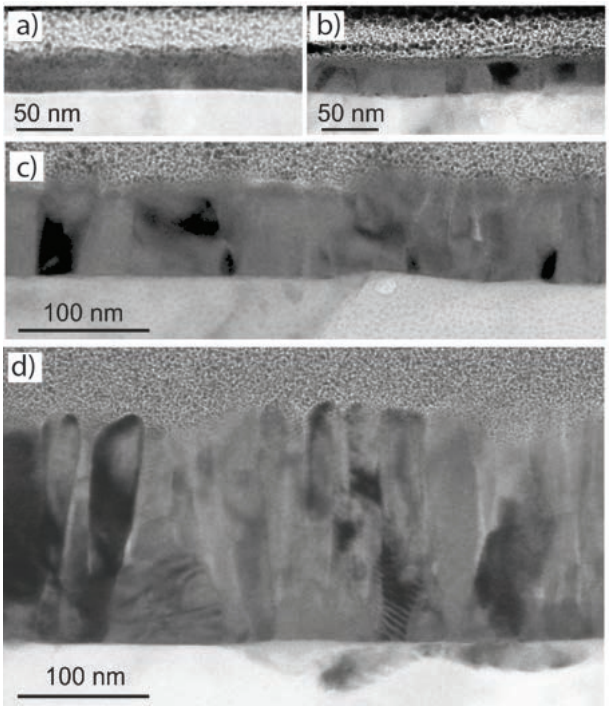

Pav. 3.1: Praėjusių elektronų šviesaus lauko LSMO sluoksnių augintų 750 °C temperatūroje ant stiklo keramikos vaizdai: storis $d = 25$ nm (a, b), $d = 75$ nm (c) $d = 170$ nm (d).

Sluoksnių, užaugintų žemiausioje 600°C temperatūroje, mikrostruktūra yra koloninė, tačiau kolonos yra sulaužytos, sluoksnis yra akytas. Be to, šiuose sluoksniuose pastebimos kolonų ir atskirų smulkesnių kristalitų samplaikos, ypač arčiau padėklo esančiuose srityse, o artimiausio padėklui 5 nm tarpinio sluoksnio vaizdas išplaukęs - parodantis, kad sluoksnio augimas prasidėjo amorfine faze. Tai atitinka empirinius stebėjimus, kad sluoksnio kristalizacijos temperatūra atvirkščiai proporcinga sluoksnio storio eksponentinei funkcijai [86–88], o konkrečioje temperatūroje kristalizacijos procesas gali prasidėti tik kai sluoksnio storis pasiekia tam tikrą su auginimo temperatūra susijusią kritinę ribą. Tirtu atveju sluoksio kaitinimo 600 °C temperatūroje pusę valandos nepakako, kad besikristalizuojančių kolonų apačia pasiektų padėklą.

Sluoksnio, užauginto 650°C TEM vaizduose (žr. pav. 3.2 c, d) matoma struktūra panaši į sluoksnių, užaugintų 600°C temperatūroje, nors kristalitų kolonos struktūra šiek tiek tvarkingesnė, amorfinis tarpsluoksnis plonesnis.

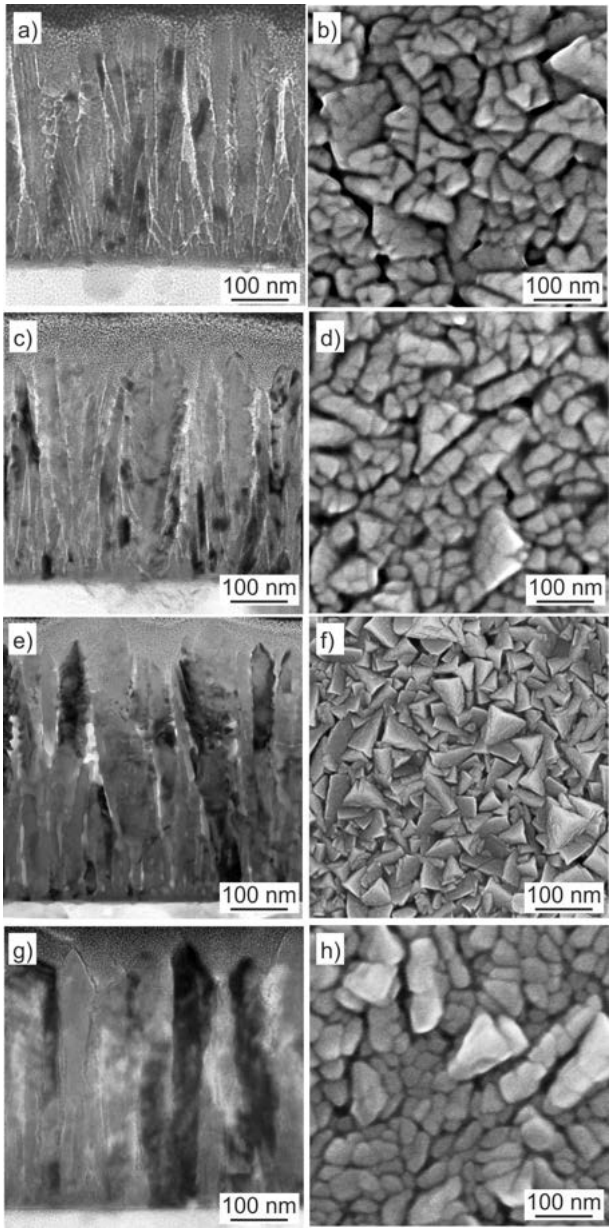

Pav. 3.2: Praėjusių elektronų šviesaus lauko (a, c, e, g) ir elektronų mikroskopo (b, d, f, h) LSMO sluoksnių augintų 600 °C (a,b), 650 °C (c, d), 700 °C (e, f) ir 750 °C (g, h) ant stiklo keramikos padėklų vaizdai.

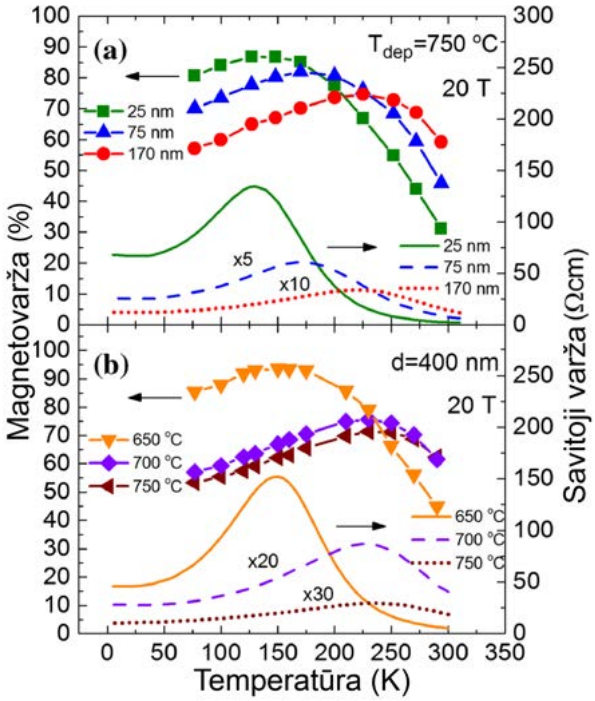

Pav. 3.3: Skirtingo storio sluoksnių (a) ir skirtingose temperatūrose augintų sluoksnių (b) savitosios varžos ir magnetovaržos (20 Teslų magnetiniame lauke) priklausomybė nuo temperatūros.

Augimo temperatūros padidinimas iki 700°C ir 750°C lemia kokybiškesnių koloninių struktūrų susidarymą sluoksnyje ir didesnius kristalitų horizontalius bei vertikalius matmenis (žr. pav. 3.2 e-h). Pav. 3.2 e ir g matomi seklesni į sluoksnį įsiterpusios Pt dangos (nusodintos ant sluoksnio prieš bandinį pjaunant TEM tyrimui) pėdsakai rodo, kad sluoksnis yra tankesnis. Geriausia struktūra yra sluoksnio, nusodinto 750°C temperatūroje (žr. pav. 3.2 g).

Grafikai 3.3 pav. rodo, kad kiekvienas sluoksnis turi skirtingą metalo - izoliatoriaus fazinio virsmo temperatūrą T_m, o sluoksnių elektrinio laidumo parametrai yra susiję su sluoksnių storiu: plonesnių sluoksnių metalo - izoliatoriaus fazinio virsmo temperatūra T_m yra žemesnė, bet didesnė maksimali savitoji varža ρ_m. T_m ir ρ_m vertės rodo didelį skirtumą tarp polikristalinių ir geros kokybės epitaksinių LSMO sluoksnių: polikristalinių sluoksnių ρ_m svyruoja nuo 1 Ωcm iki daugiau nei šimto Ωcm, o T_m yra žemesnis nei 250 K,

o epitaksinių sluoksnių savitoji varža būna $\mu\Omega$cm eilės, o tipinė metalo- izoliatoriaus fazinio virsmo temperatūra T_m yra aukštesnė nei 310 K [5, 89].

Skirtingo storio sluoksnių ir skirtingose temperatūrose augintų sluoksnių magnetovaržų priklausomybės nuo temperatūros, kai magnetinio srauto tankis yra 20 Teslų, pateikiamos 3.3 pav. Manganitų sluoksnių MR yra neigiama, tad patogesniam $\rho_m(T)$ ir $MR(T)$ sugretinimui pateikiamos absoliutinės MR vertės. Visų sluoksnių didžiausios MR vertės pasiekiamos, kai temperatūra yra artima metalas - izoliatorius fazinio virsmo temperatūrai T_m, o aukštos MR vetės stebimos plačiame temperatūrų ruože. Tuo šie nanostrutūrizuoti sluoksniai skiriasi nuo epitaksinių sluoksnių, kurių aukštos MR vertės stebimos tik esant temperatūrai artimai T_m [5, 89].

Pastarojo reiškinio mechanizmas yra susijęs su feromagnetine tvarka kai sluoksnio $T < T_m$. Tobulos struktūros kristalitų ar epitaksinių sluoksnių fazinis virsmas iš paramagnetinės į feromagnetinę fazę vyksta visame tūryje siaurame temperatūros ruože, atitinkamai, su virsmu susijęs savitosios varžos ρ_m pokytis įvyksta greitai ir jos kitimo nuo temperatūros grafikas yra labai status. Žemoje temperatūroje epitaksinis manganito sluoksnis arba polikristalinėje medžiagoje esantis kristalitas yra feromagnetinėje fazėje ir jų įmagnetėjimą galima įsotinti gana silpnu magnetiniu lauku. Priešingai, polikristalinių sluoksnių tarpkristalitinės sritys veikia kaip netvarkinga magnetinė medžiaga, pasižyminti mažesniu įmagnetėjimu ir žemesne fazinio virsmo temperatūra, nanostrutūrizuotų LSMO sluoksnių įsotinimą galima pasiekti tik stipriu magnetiniu lauku.

Pav. 3.3 b pateikiamos 400 nm storio manganitų sluoksnių, užaugintų 650°C, 700°C ir 750°C nusodinimo temperatūrose, savitųjų varžų priklausomybės nuo temperatūros. Sluoksnio, auginto 650°C , savitosios varžos priklausomybė panaši į 25 nm sluoksnio savitosios varžos priklausomybę (tik 15% aukštesnės T_m ir ρ_m), šis panašumas rodo, kad sluoksnis yra netvarkus. LSMO sluoksnis, užaugintas 600°C temperatūroje (paveiksle neparodyta), turėjo labai didelę savitąją varžą, o metalas – izoliatorius fazinis virsmas matuotame ruože (matavimo riba buvo iki 9 kΩcm esant 50 K) nebuvo pastebėtas. Sluoksnio, užauginto 700°C , parametrai yra labai artimi parametrams 170 nm storio sluoksnio, užauginto esant 750°C nusodinimo temperatūrai.

3.3 b pav. pateikiamos sluoksnių magnetovaržos priklausomybės nuo temperatūros kai B= 20 Teslų. Sluoksnis, užaugintas T_{dep} = 650 °C temperatūroje ir turintis labiausiai netvarkią struktūrą su mažesniais nei kiti sluoksniais kristalitais, turi didžiausias MR reikšmes kai $T < T_m$. Sluoksniai, užauginti aukštesnėje T_{dep} temperatūroje ir turintys tvarkingesnę struktūrą, parodė didesnes

MR reikšmes kambario temperatūroje ($\approx$290 K).

3.1.2 Išvados

Ploni $La_{1-x}Sr_xMnO_3$ manganitų sluoksniai, nusodinti impulsiniu injekciniu MOCVD būdu ant stiklo keramikos padėklų, turi makroskopiškai homogeniškas struktūras, kurių parametrai (tolimoji tvarka, kristalitų formavimasis, jų dydis bei forma, tarpkristalitinės sritys) labai priklauso nuo nusodinimo temperatūros ir sluoksnių storio. Sluoksniai, kurių storis yra mažesnis nei $\approx$ 25 nm, susideda daugiausia iš amorfinės fazės, o storesniems sluoksniams būdingos polikristalinės koloninės mikrostruktūros.

Nanostruktūrizuotų sluoksnių augimo sąlygų įtaka augintų ir tirtų sluoksnių kolosalios magnetovaržos reiškiniui impulsiniuose magnetiniuose laukuose iki 20 T rodo galimybę valdyti sluoksnių charakteristikas (varžą, magnetovaržą ir jos anizotropiją) pritaikant įvairiai darbinei temperatūrai ir magnetiniams laukams. Tad įmanoma kurti iš anksto nustatytų parametrų magnetinio lauko jutiklius pagal konkretaus jų taikymo reikalavimams. Gaminant kambario temperatūros jutiklius, optimalu auginti 400 nm nanostruktūrizuotus La-Sr-Mn-O sluoksnius 750°C temperatūroje.

3.2 Su Mn pertekliumi auginti LSMO sluoksniai

3.2.1 Tyrimai

Nanostruktūrizuoti manganitų sluoksniai su Mn pertekliumi buvo auginti ant polikristalinių Al_2O_3 padėklų 750°C temperatūroje, jų storis $\approx$ 400nm. Bandinių savitosios varžos matavimų rezultatai pateikti 3.4 pav., palyginimui pateiktos ir ant stiklo keramikos padėklo užauginto sluoksnio savitosios varžos priklausomybės nuo temperatūros kreivė. Bandinių su Mn pertekliumi magnetovaržos priklausomybės nuo temperatūros 20 Teslų magnetiniame lauke pateiktos 3.5 pav.

Iš grafikų ir lentelės 2.3 matoma, kad LSMO sluoksniuose Mn daliai (koncentracijai) padidėjus virš stechiometrinės (santykiui $\frac{Mn}{La+Sr}$ padidėjus nuo 1,05 iki 1,10 ir 1,15), metalas - izoliatorius fazinio virsmo temperatūra T_m padidėjo nuo 240 K iki 270 K, o maksimali savitoji varža sumažėjo nuo 0,475 Ωcm iki 0,25 Ωcm (net 47%).

Pokyčius galima paaiškinti tuo, kad legiruotuose milžiniškos magnetovaržos (CMR) manganituose yra įvairaus valentingumo Mn jonų, tačiau magnetines

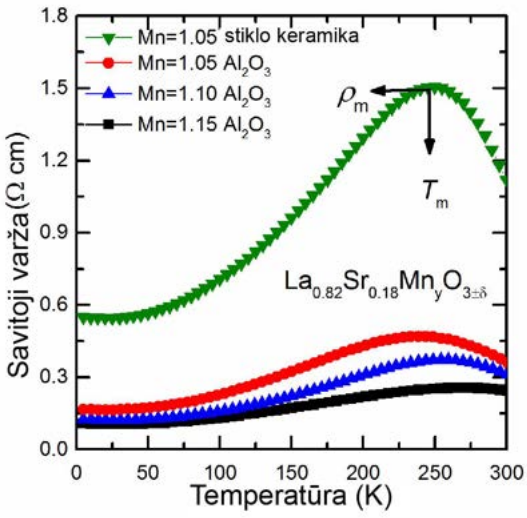

Pav. 3.4: Bandinių su Mn pertekliumi savitosios varžos priklausomybė nuo temperatūros.

sąveikas ir susijusias krūvio pernašos savybes lemia Mn^{4+} ir Mn^{3+} jonų koncentracijų santykis. Paprastai Mn^{4+}/Mn^{3+} santykis koreguojamas keičiant dvivalenčių Sr, Ca arba Ba legiravimo jonų koncentracijas [6, 96–98] arba formuojant struktūrinius defektus, pvz., Mn arba La vakancijas [99–104]. Tačiau panašų efektą galima pasiekti sukuriant santykinį Mn perteklių [99, 100], kuris paskatinamas La trūkumu. Tada gardelė, kurioje trūksta La^{3+}, atima elektroną iš Mn^{3+} ir padidina Mn^{4+}/Mn^{3+} santykį. Kitaip tariant, $La_{0,82}Sr_{0,18}Mn_yO_3$ sluoksnių legiravimas La vakansijomis leidžia pasiekti norimą Mn^{4+}/Mn^{3+} santykį, sumažinti savitąją varžą ir pakelti fazinio virsmo temperatūrą .

Sluoksnių magnetovarža apskaičiuota iš sluoksnių varžos, išmatuotos $B = 20$ Teslų srauto tankio magnetiniame lauke 77–363 K temperatūros ruože (3.5 pav.). Sluoksniai su artima stechiometrinei Mn dalimi (1,05) parodė didžiausią magnetovaržos vertę, tačiau ji buvo pasiekta esant 200 K temperatūrai; šio sluoksnio magnetovarža buvo mažiausia $T > 260$ K temperatūros ruože. Esant $T = 300$ K temperatūrai didžiausią MR parodė sluoksnis su 10% Mn pertekliumi, o esant 363 K temperatūrai, didžiausios MR vertės gautos sluoksniui su 15% Mn pertekliumi. Šis rezultatas - kad padidėjus Mn koncentracijai, padidėja magnetovarža - koreliuoja su T_m pasislinkimu į aukštesnes temperatūras didinant Mn koncentraciją.

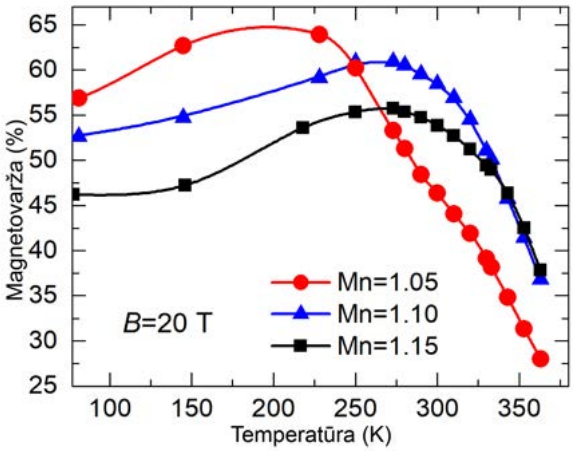

Pav. 3.5: Bandinių su Mn pertekliumi magnetovaržos priklausomybė nuo temperatrūros. Matavimai atlikti esant B=20 Teslų magnetinei indukcijai.

363 K temperatūroje silpname magnetiniame lauke (kai magnetinio srauto tankis $\leqslant$ 1 Tesla) sluoksnių su Mn koncentracija 1,05 ir 1,10 jautrumas labai mažas (MR, atitinkamai, tik apie 0,16% ir 0,35%), tuo tarpu sluoksnių, kurių Mn dalis viršija 15%, MR to paties tankio magnetiniame lauke buvo 0,65% .

3.2.2 Išvados

Mn kiekio įtakos nanostruktūrizuotuose $La_{1-x}Sr_xMn_yO_3$ sluoksniuose tyrimų rezultatai rodo, kad Mn perteklius keičia šių sluoksnių elektrinį laidumą ir magnetines savybes.

- Padidinus santykį $\frac{Mn}{La+Sr} > 1$, metalas - izoliatoriaus fazinio virsmo temperatūra T_m pasislenka į aukštesnių temperatūrų sritį, o maksimali varža ρ_m sumažėja. Padidinus Mn kiekį nuo 1,05 iki 1,15, T_m pakilo maždaug 30°C. Nors sluoksnių su Mn pertekliumi magnetovaržos vertės mažėja žemų temperatūrų srityje (daug žemesnėje nei T_m), esant aukštesnei nei 320 K temperatūrai didžiausios MR vertės buvo gautos sluoksniams, kurių didžiausias Mn perteklius buvo 1,21. Gautus rezultatus galima paaiškinti La–Sr–Mn–O sluoksnių savilegiravimu, kai Mn perteklius sąlygoja La vakansijas La vakansijas, gerindamas Mn^{4+}/Mn^{3+} santykį ir sustiprina La–Sr–Mn–O sluoksnių feromagnetizmą.

- Magnetinio lauko jutikliai, pagaminti iš sluoksnių, kurių Mn koncentracija viršija 15%, turi didesnį jautrį magnetiniam laukui aukštoje temperatūroje. Mn kiekio padidėjimas La–Sr–Mn–O sluoksniuose leidžia juos panaudoti kuriant stipraus impulsinio magnetinio lauko jutiklius, veikiančius iki 360 K temperatūroje.

3.3 Ant įvairių padėklų auginti LSMO sluoksniai

3.3.1 Tyrimai

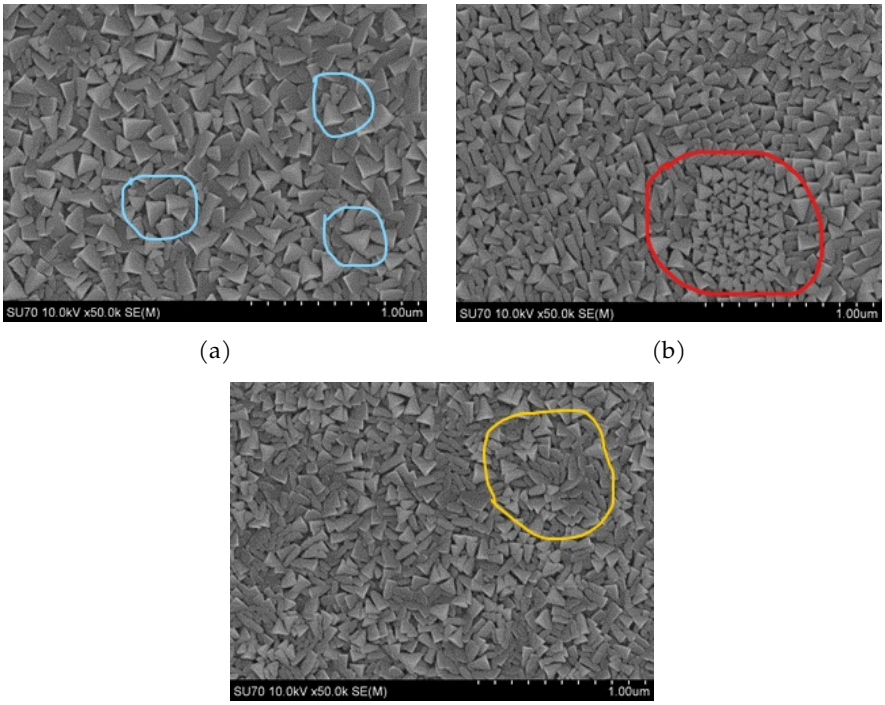

(a) (b)

(c)

Pav. 3.6: 360 nm storio LSMO sluoksnių augintų ant kvarco (a), polikristalinio Al_2O_3 (b) ir Si/SiO_2-1000 padėklų paviršių SEM nuotraukos.

Šios bandinių grupės auginimo ir analizės tikslas buvo ištirti, kaip padėklo cheminė sudėtis ir kristalinė struktūra veikia sluoksnių struktūrą, elektrines ir magnetovaržines savybes. Tyrimams buvo pasirinkti AT-pjuvio monokristalinio kvarco, polikristalinio Al_2O_3 ir amorfinio Si/SiO_2-1000 padėklai. Remi-

antis tendencija, kad padidėjęs Mn kiekis padidina maksimalios varžos temperatūrą T_m, PI MOCVD prekursoriai buvo subalansuoti taip, kad pasiekti ≈20% Mn perteklių. Nusodinimo laikas ir greitis užauginti ≈400 nm sluoksnio storį bei 750°C nusodinimo temperatūra buvo tokie patys, kaip ir auginant 3-čios serijos bandinius.

360 nm storio LSMO sluoksnių SEM vaizduose (žr. 3.6 pav.) matomi ant skirtingų padėklų užaugintų sluoksnių paviršių morfologijos skirtumai, tame tarpe ir kristalitų dydžių skirtumai. Ant kvarco užaugintų sluoksnių kristalitai yra didžiausi, jų tikimiausias skermuo yra 70 nm, o ženklios dalies kristalitų skermuo siekia beveik 200 nm; dauguma kristalitų turi trikampę formą. Ant polikristalinio Al_2O_3 padėklo augintų kristalitų matmenys yra labiausiai homogeniški (net 14% kristalitų yra 60 nm skermens). Trikampio ir daugiakampio formos kristalitų kiekiai yra maždaug vienodi. Išskirtinis ant polikristalinio Al_2O_3 padėklo augintų sluoksnių bruožas yra kristalitų klasterizacija: apatinėje dešinėje SEM nuotraukos dalyje aiškiai matomas mažesnių kristalitų klasteris.

Ant Si/SiO_2-1000 padėklo auginto sluoksnio kristalitų matmenys yra mažiau homogeniški (12% kristalitų skermuo yra 60 nm), tačiau daugiakampio formos kristalitų yra daugiau nei trikampio formos kristalitų. Kristalitų formų ir dydžių pasiskirstymai SEM vaizdo plote yra atsitiktiniai.

Sluoksnių TEM vaizdai parodo kitus ant skirtingų padėklų augintų sluoksnių skirtumus (žr. 3.7 pav.): amorfinius tarpsluoksnius tarp padėklų ir koloninių struktūrų (kvarco ir Si/SiO_2-1000 padėklai - atitinkamai 3.7 a pav. ir 3.7 c pav.) bei mažų kristalitų sankaupos virš amorfinio pilko sluoksnio (3.7 c pav. apibrėžta taškinėmis linijomis). Pastarieji kristalitai arčiau sluoksnio paviršiaus suauga į didesnes kolonas.

Ant kvarco ir Si/SiO_2-1000 padėklų augintų sluoksnių padėklų ir sluoksnių pagrindinių cheminių elementų TEM-EDS linijų profiliai (žr. 3.8 pav.) parodo abipusę pagrindinių elementų difuziją. LSMO sluoksnių ant Al_2O_3 padėklo TEM-EDS analizė tarpusavio difuzijos neatskleidė.

Kristalitų struktūros kokybę galima vertinti iš dviejų gretimų LSMO kristlitų, užaugintų ant kvarco ir Si/SiO_2-1000 padėklų ribų TEM vaizdų (žr. 3.9 pav.). Abiem atvejais matomos siauros tarpinės sritys, skiriančio skirtingų kristalinių orientacijų LSMO kristalitus. Skirtumą tarp struktūrų, užaugintų ant skirtingos rūšies padėklų parodo linijų formos: riba tarp kristalitų, esančių ant kvarco padėklo yra tiesi, maždaug vieno nm pločio, du gretimi kristalitai yra pasukti vienas kito atžvilgiu tik keliais laipsniais (3.9a pav.), o sluoksnyje, užaugintame ant Si/SiO_2-1000 riba tarp kristalitų sudaro maždaug 2 - 3 nm

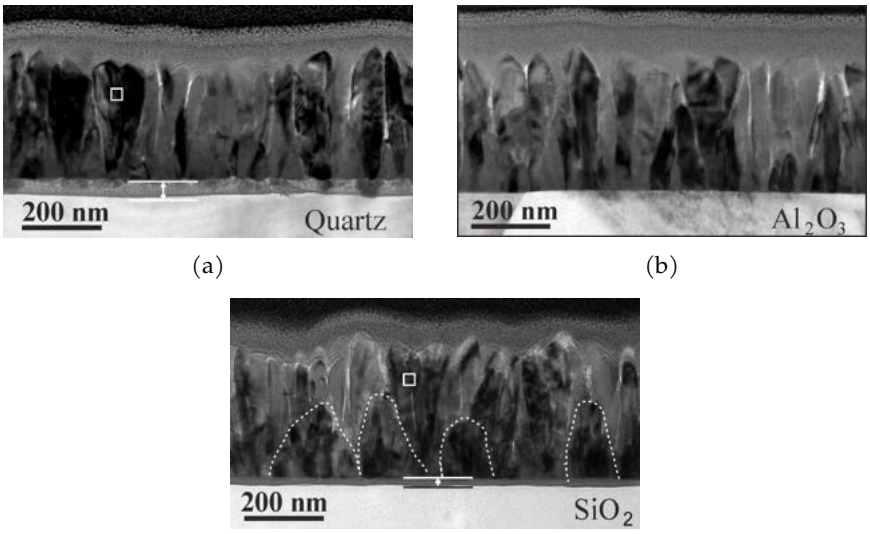

(a) (b)

(c)

Pav. 3.7: 360 nm storio LSMO sluoksnių augintų ant kvarco (a), polikristalinio Al_2O_3 (b) ir Si/SiO_2-1000 padėklų TEM nuotraukos.

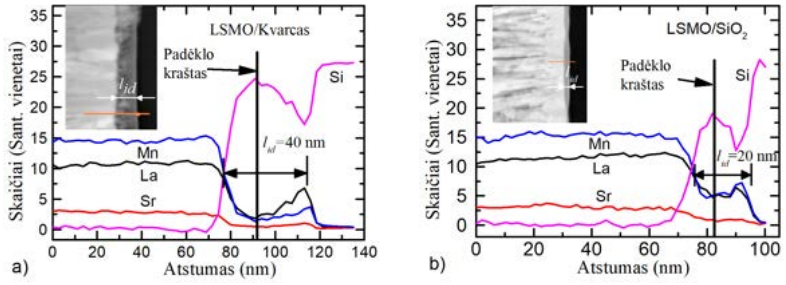

Pav. 3.8: 360 nm storio sluoksnių augintų ant kvarco (a) ir Si/SiO_2-1000 (b) pagrindinių elementų TEM-EDS pasiskirstymo profilių grafikai. Intarpuose pateiktose STEM Z-kontrastinės nuotraukose parodytos skenavimo linijos.

pločio zigzagą (žr. 3.9b pav.). Šis skirtumas parodo, kad ant kvarco užaugintų kristalitų geometrija yra tvarkingesnė.

Paveiksle 3.10 pateikiamos plonų (60 nm) ir storų (360 nm) LSMO sluoksnių, užaugintų ant kvarco, polikristalinio Al_2O_3 ir Si/SiO_2-1000 padėklų savitųjų varžų ρ priklausomybės nuo temperatūros. Visų sluoksnių metalas - izoliat-

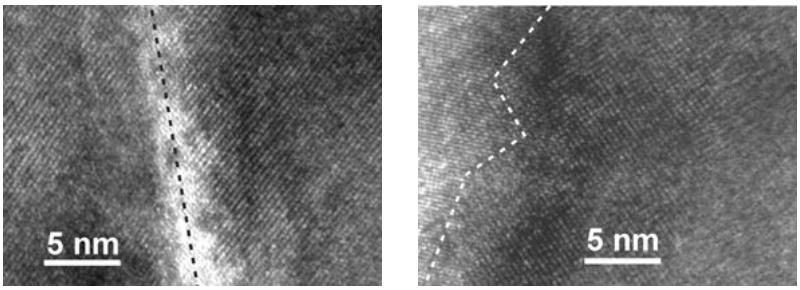

(a) (b)

Pav. 3.9: Bandinių augintų ant kvarco (a) ir ant Si/SiO_2-1000 (b) kelių LSMO kristalitų sąlyčio ribų didelės raiškos TEM vaizdai.

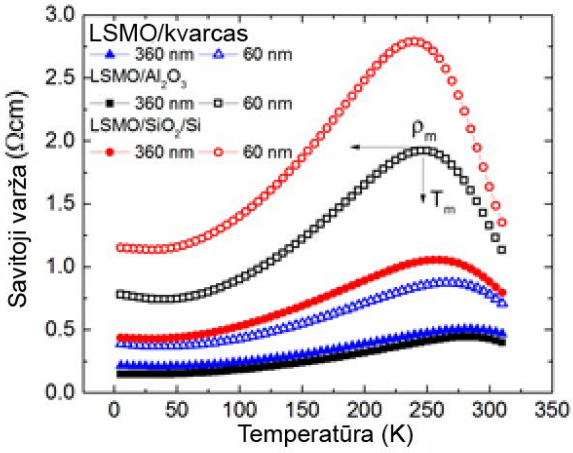

Pav. 3.10: Bandinių augintų ant kvarco, Al_2O_3 ir Si/SiO_2-1000 padėklų savitosios varžos priklausomybė nuo temperatūros. Sluoksnių storiai buvo 60 nm ir 360 nm.

orius faziniai virsmai stebimi tarp 250 K ir 285 K. Tačiau maksimalios skirtingų sluoksnių savitosios varžos ρ_m yra išsibarsčiusios plačiame ruože. Matoma tendencija, kad tarp vienodo storio sluoksnių mažiausios savitosios varžos ρ_m vertės yra sluoksnių, užaugintų ant monokristalinio padėklo, o didžiausios vertės - sluoksnių, užaugintų ant amorfinio padėklo. Tai, kad plonų sluoksnių savitosios varžos didesnės nei storų, galima susieti su kristaline struk-

tūra: plonesnių sluoksnių kristalitai mažesni, o vienodame sluoksnio tūryje daugiau netvarkios medžiagos.

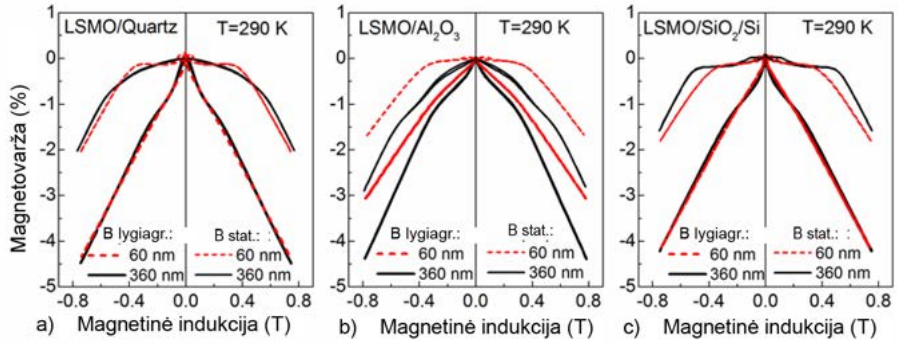

Pav. 3.11: 60 nm ir 360 nm storio sluoksnių augintų ant kvarco, Al_2O_3 ir Si/SiO_2-1000 magnetovaržos silpname magnetiniame lauke priklausomybė nuo magnetinės indukcijos 25 K temperatūroje.

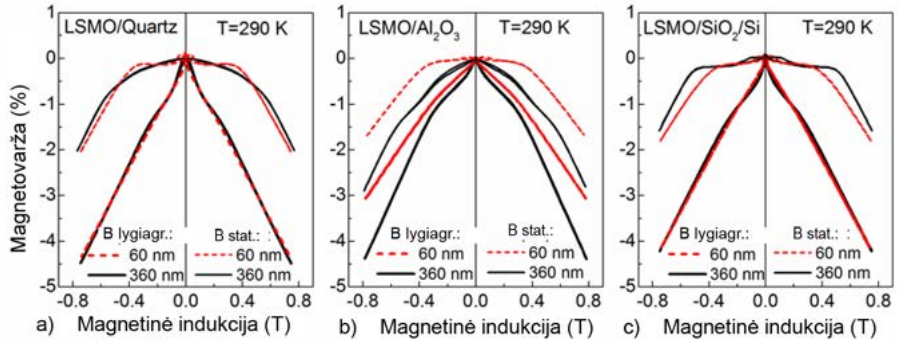

Pav. 3.12: 60 nm ir 360 nm storio sluoksnių augintų ant kvarco, Al_2O_3 ir Si/SiO_2-1000 magnetovaržos silpname magnetiniame lauke priklausomybė nuo magnetinės indukcijos 290 K temperatūroje.

Magnetovaržos (MR) priklausomybės nuo magnetinės indukcijos B, kai B kinta nuo 0 iki 0,75 Teslos, o magnetinis laukas nukreiptas lygiagrečiai ($B \parallel$) arba statmenai ($B \perp$) sluoksnio plokštumai, išmatuotos skirtingose temperatūrose, pateiktos 3.11 ir 3.12 paveiksluose. Pagrindinės MR savybės ryškesnės žemoje temperatūroje: aštri teigiamos MR smailė $B \parallel$ atveju; šios smailės padėtis atitinka maksimalią bandinio varžą, kai magnetinių domenų su lygiagrečiais ir antilygiagrečiais magnetiniais momentais koncentracijos susilygina.

Smailės magnetinės indukcijos vertė parodo bandinio koercinio lauko dydį.

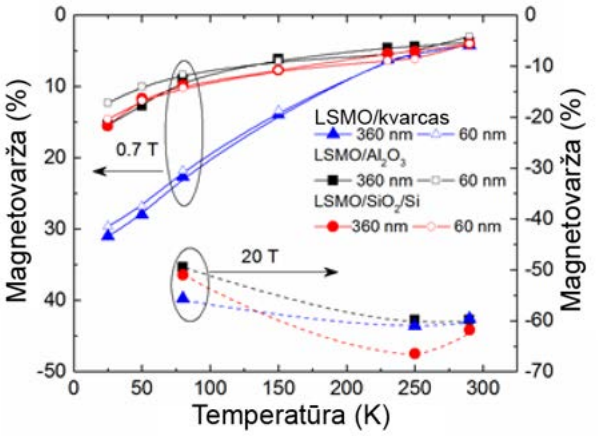

Pav. 3.13: 60 nm ir 360 nm storio sluoksnių augintų ant kvarco, Al_2O_3 ir Si/SiO_2-1000 magnetovaržos priklausomybės nuo temperatūros. Skalė kairėje - B= 0.7 Teslos, skalė dešinėje - B=20 Teslų.

Silpno lauko magnetovaržą $LFMR$ apibrėžėme kaip MR reikšmę 0,7 Teslos magnetiniame lauke. Ant kvarco užaugintų sluoksnių $LFMR$ yra didžiausia ($LFMR$= 31% 360 nm storio sluoksniui ir $LFMR$ = 30% 60 nm storio sluoksniui) - du kartus didesnės nei $LFMR$ bandinių užaugintų ant Si/SiO_2-1000 padėklų ($LFMR$ = 15,5% 360 nm storio sluoksniui ir $LFMR$ = 14,6% 60 nm storio sluoksniui) arba ant Al_2O_3 padėklo ($LFMR$ = 15,4% 360 nm storio sluoksniui ir $LFMR$ = 12,3% 60 nm storio sluoksniui).

Pav. 3.13 pateikti ketvirtosios plonų sluoksnių bandinių grupės magnetovaržos stipriame lauke matavimų rezultatai. Tarp šių bandinių ant kvarco padėklo užauginti bandiniai turi didžiausią magnetovaržą (26% - 60%) silpnuose (B = 0,7 Teslos) ir stipriuose (B = 20 Teslų) magnetiniuose laukuose esant žemai temperatūrai (žemiau 100 K) ir didelę (bet ne didžiausią) magnetovaržą ($\approx$60%) stipriame magnetiniame lauke kambario temperatūroje. Šių bandinių magnetovarža silpname magnetiniame lauke kambario temperatūroje yra <7%. Tokias charakteristikas galima paaiškinti palankia kristalitų ir tapkristalitinių sričių pusiausvyra: tarp didelių kristalitų yra daugiau netvarkios struktūros. Šioje struktūroje kristalitų viduje esančių Mn atomų sukinius sulygiuoja ir silpnas magnetinis laukas, tačiau netvarkioje tarpkristalitinėje srityje esančių atomų magnetinių momentų perorientavimui reikia stipresnio magnetinio

lauko ir (arba) žemos temperatūros.

Bandinių, užaugintų ant Si/SiO_2-1000 padėklų didžiausia (>60%) magnetovarža yra stipriame (B = 20 Teslų) magnetiniame lauke kambario temperatūroje, tačiau magnetovarža yra vidutinė (tarp vertintų bandinių) žemoje temperatūroje ir mažas silpname magnetiniame lauke kambario temperatūroje. Tokias savybes lemia medžiagos struktūra - santykinai maži, glaustai išsidėstę kristalitai, tarp kurių yra santykinai maža netvarkios struktūros. Mažuose kristalituose gali formuotis pavieniai magnetiniai domenai, kuriuos sunku perorientuoti, todėl stipriuose laukuose kambario temperatūroje magnetovarža yra didelė, tačiau silpnuose laukuose magnetovarža yra maža (nes nepakanka magnetinės jėgos perorientuoti kristalitų viduje susiformavusius magnetinius domenus). Stipriuose magnetiniuose laukuose, padidinus magnetinį lauką iki tam tikro lygio, plonose tarpkristalitinėse srityse magnetiniai momentai yra perorientuojami ir magnetovarža pradeda mažėti.

Bandinių užaugintų ant Al_2O_3 padėklo magnetovaržos kreivė silpname magnetiniame lauke yra labai panaši į bandinių ant Si/SiO_2-1000 padėklo magnetovaržos kreivę, tačiau stipriame lauke (B = 20 Teslų) magnetovarža yra tolygesnė plačiame temperatūros ruože. Pastarąjį skirtumą galima paaiškinti homogeniškesniais kristalitų matmenimis, dėl kurių visa sluoksnio struktūra yra homogeniškesnė mikro lygmenyje ir paskatina tiesines magnetovaržos charakteristikas.

3.3.2 Išvados

Padėklo pasirinkimas nusodinant nanostrutūrizuotus $La_{1-x}Sr_xMn_yO_3$ manganito sluoksnius, daro didelę įtaką šių sluoksnių charakteristikoms (savitajai varžai, magnetovaržai ir jos anizotropijai) silpname magnetiniame lauke (<0,7 Teslos) ir žemoje temperatūroje. Sluoksniai, kurių storis 360 nm, auginami ant monokristalinio kvarco, pasižymi didele magnetovaža silpname magnetiniame lauke (31%, esant T = 25K), tuo tarpu sluoksniams, auginamiems ant polikristalinio Al_2O_3 ir amorfinių SiO_2 padėklų, ši vertė buvo apie 15,5%. Tai gali lemti tobulesnė sluoksnių, užaugintų ant kvarco, koloninė struktūra ir difuzinio sluoksnio tarp kvarco paviršiaus ir sluoksnio įtaka.

Ant skirtingų padėklų užaugintų nanostrutūrizuotų LSMO sluoksnių magnetovaržos vertės stipriame magnetiniame lauke yra panašios. Tai galima paaiškinti tuo, kad stiprus magnetinis laukas daugiausia įtakoja Mn jonų magnetinių momentų orientavimą netvarkingose tarpkristalitinėse srityse, nes tvarkingesnės struktūros kristalitų magnetiniai momentai pilnai orientuojami

jau ≈10 Teslų magnetiniame lauke ir jų magnetovarža jau būna įsotinta.

3.4 LSMO jutiklių pritaikymas matuoti magnetinį lauką magnetinio impulsinio metalų suvirinimo procese

3.4.1 Tyrimai

Su B-skaliariniais magnetinio lauko jutikliais, pagamintais iš LSMO sluoksnių užaugintų ant polikristalinio Al_2O_3 su Mn pertekliumi, buvo atlikti metalų magnetinio impulsinio suvirinimo magnetinio lauko dinamikos tyrimai.

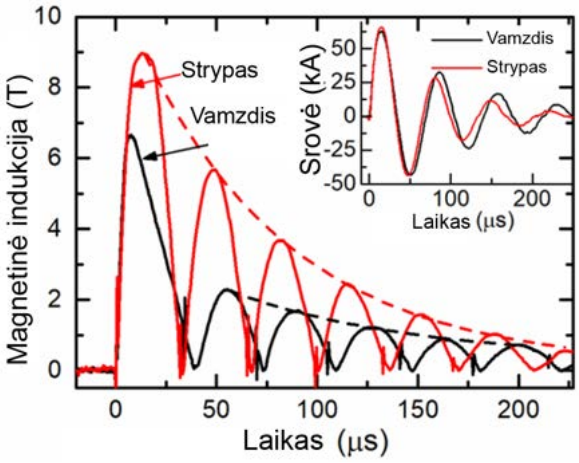

Pav. 3.14: Magnetinio lauko dinamika tarpe tarp magnetinio lauko formuotuvo ir judančios (spaudžiamos) detalės. Intarpe pateikti kondensatorių iškrovos elektros srovių grafikai. Juodos kreivės – aliuminio vamzdis 1.5 mm storio sienele spaudimas, raudonos kreivės – tyrimai su masyviu aliuminio strypu.

Matavimų metu (1) kondensatorių baterija (pav. 2.4) buvo įkraunama iki $E =$ 4 kJ energijos, (2) kondensatorių iškraunant per ritę, ritėje buvo generuojami slopstantys srovės svyravimai ir indukuojamas kintamas silpstantis magnetinis laukas. Slopinimo efektą sukelia vidinė sistemos varža. Tarpe tarp magnetinio lauko formuotuvo ir judančios detalės (arba strypo) patalpintas CMR-B skaliarinis magnetinio lauko jutiklis matavo absoliučią magnetinio srauto tankio B vertę (pav. 3.14), tad grafikuose atvaizduotos vieno poliariškumo periodinio mažėjančios amplitudės magnetinio lauko kreivės.

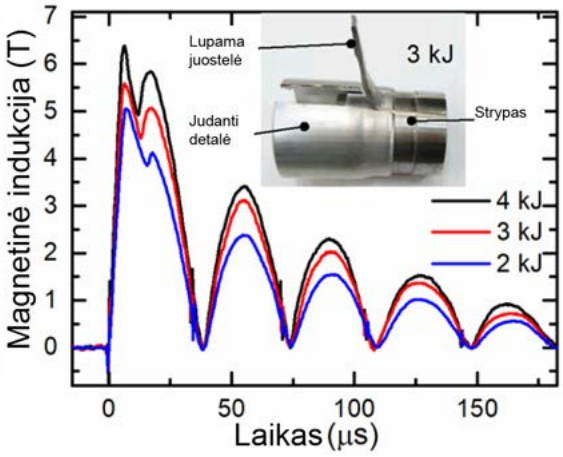

Pav. 3.15: Magnetinio lauko dinamika tarpe tarp magnetinio lauko formuotuvo ir judančios (spaudžiamos) aliuminio detalės (vamzdžio) esant įvairioms kondensatorių baterijos įkrovos energijoms. Vamzdžio sienelės storis 1.5 mm, tarpas tarp spaudžiamo vamzdžio ir strypo – 1.5 mm. Intarpe parodytas suvirintų detalių suvirinimo kokybės tyrimas plėšimo būdu.

Matavimų su aliuminio strypu metu magnetinio lauko svyravimų amplitudė mažėja pagal slopinamųjų svyravimų dėsnį (punktyrinė linija) su eksponentine laiko konstanta $\tau = 75{,}5\ \mu$s. Tačiau vamzdžio suspaudimo atveju po pirmojo (nukrypusio nuo sinuso formos) pusbangio sekančių pusbangių amplitudės yra žymiai mažesnės ir magnetinis laukas svyruoja pagal slopinamųjų svyravimų dėsnį su eksponentine laiko konstanta $\tau = 90{,}7\ \mu$s. Taip yra dėl to, kad per pirmąjį srovės pusbangį vamzdis deformuojamas, dėl to smarkiai padidėja sistemos, susidedančios iš vamzdžio ir lauko formuotuvo, induktyvumas. Šią išvadą patvirtina ir magnetinio lauko svyravimų dažnio sumažėjimas (žr. pav. 3.14).

Tolesni MIS eksperimentai vyko su aliuminio vamzdžiais, spaudžiamais aplink plieninę šerdį esant skirtingoms kondensatorių baterijos įkrovos energijoms E. Magnetinio lauko svyravimai eksperimentų metu kai $E = 2$, 3 ir 4 kJ parodyti 3.15 paveiksle. Pradiniu momentu atstumas tarp vamzdžio vidinės sienelės ir plieninė šerdies buvo 1,5 mm. Iš 3.15 pav. matoma, kad visų trijų suvirinimo eksperimentų pirmasis pusbangis turi dvi smailes. Pirmoji smailė yra panaši į tą, kuri pastebėta atliekant laisvą vamzdžio suspaudimą (žr. 3.14 pav.). Smailių amplitudė priklauso nuo kondensatoriaus įkrovimo energijos: kuo mažesnė įkrovimo energija, tuo mažesnė magnetinio lauko smailės amp-

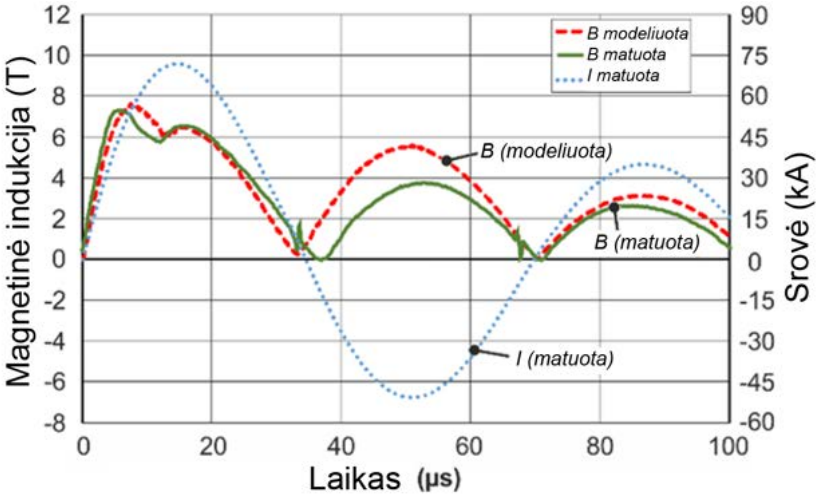

Pav. 3.16: Išmatuotos (žalia linija) magnetinio lauko dinamikos tarpe tarp magnetinio lauko formuotuvo ir judančios (spaudžiamos) aliuminio detalės (vamzdžio) palyginimas su LS-DYNA programa modeliuota (dauginta iš koeficiento 0.3, raudona brūkšninė linija) magnetinio lauko dinamika (skalė kairėje) išmatuoti elektros srovės svyravimai (mėlyna taškinė linija). Aliuminio vamzdžio sienelės storis $d = 2$ mm.

litudė, o šių smailių maksimumas pasiekiamas vėliau. Šis pasikeitimas lyginant su laisvo suspaudimo eksperimentais (žr. 3.14 pav.), gali būti siejamas su plieninės šerdies įtaka: sistemos induktyvumas matavimo taške susideda iš judančio (spaudžiamo) aliuminio vamzdžio kintančio induktyvumo ir standžios plieninės šerdies induktyvumo. Todėl stebima magnetinio lauko dinamika yra dviejų reiškinių superpozicija: magnetinio lauko kitimo vamzdžio laisvo suspaudimo metu ir magnetinio lauko kitimo su standžiu ruošiniu. Pasibaigus pirmajai smailei, įvykus detalių susidūrimui, magnetinė indukcija sumažėja iki tam tikros minimalios vertės, tada atsiranda antra smailė po kurios magnetinė indukcija nukrenta iki nulio. Matavimų rezultatus palyginus su suvirinimo kokybės tyrimu plėšimo būdu nustatyta, kad dviejų smailių atsiradimas parodo, jog suvirinimas įvyko, o šių smailių aukščių santykis ir minimumo vieta sietini su suvirinimo kokybe.

Matavimų rezultatai buvo lyginami su kompiuterinio modeliavimo rezultatais, gautais Dortmundo Technologijos universiteto Formavimo technologijų ir Lengvųjų Komponentų institute (Vokietija). 3D modeliai buvo sukurti su komercine LS-DYNA programine įranga. Išmatuotos magnetinio lauko din-

amikos, modeliuotos magnetinio lauko dinamikos ir išmatuotos ritės srovės palyginimas pateiktas 3.16pav. Grafikai rodo modeliuotų ir išmatuotų magnetinių laukų verčių atitikimą - tai rodo, kad magnetinio lauko dinamikos matavimas su CMR B-skaliariniu jutikliu tarp magnetinio lauko formuotuvo ir judančio vamzdžio (ruošinio) magnetinio impulsinio metalų suvirinimo metu suteikia naujos vertingos informacijos apie reiškinius, vykstančius formuojant ir suvirinant vamzdžius. Vamzdžio ir šerdies susidūrimo laiką dabar galima nustatyti be sudėtingų ir nepatogių naudoti Doplerio greičio matuoklių ar sudėtingų kompiuterinių modeliavimų.

3.4.2 Išvados

Magnetinio lauko jutikliai, pagaminti iš nanostruktūrizuotų $La_{1-x}Sr_xMn_yO_3$ manganito sluoksnių su Mn pertekliumi, elektromagnetinio formavimo ir magnetinio impulsinio suvirinimo (MPW) procesuose gali lokaliai išmatuoti magnetinio lauko dinamiką siaurame tarpelyje tarp magnetinio lauko formuotuvo ir judančios detalės.

4 Pagrindinės išvados

1. Ploni $La_{1-x}Sr_xMnO_3$ manganitų sluoksniai, impulsiniu injekciniu MOCVD būdu nusodinti ant stiklo keramikos padėklų, pasižymi makroskopiškai homogenine struktūra, kuri labai priklauso nuo nusodinimo temperatūros ir sluoksnių storio. Sluoksniai, kurių storis ne didesnis nei $\approx$25 nm, susideda daugiausia iš amorfinės fazės, o storesniems sluoksniams būdinga polikristalinė koloninė mikrostruktūra.

2. Nanostruktūrizuotų sluoksnių augimo sąlygų įtakos kolosalios magnetovaržos reiškinio ypatumams analizė, paveikus šiuos sluoksnius impulsiniais magnetiniais laukais iki 20 Teslų, parodė galimybę valdyti sluoksnių pagrindinius parametrus (varžą, magnetovaržą ir jos anizotropiją) plačiame temperatūrų ir magnetinių laukų ruože, pritaikant juos konkretaus taikymo reikalavimams. Tokiu būdu galime kurti magnetinio lauko jutiklius su iš anksto nustatytais parametrais. Kuriant kambario temperatūroje veikiančius jutiklius, pirmenybė turėtų būti teikiama nanostruktūrizuotiems $\approx$400 nm nanostruktūrizuotiems La-Sr-Mn-O sluoksniams, užaugintiems 750°C temperatūroje.

3. Krūvio pernašos ir magnetinės nanostruktūrizuotų $La_{1-x}Sr_xMn_yO_3$ sluoksnių savybės labai priklauso nuo Mn pertekliaus (y). Padidinus

santykį $\frac{Mn}{(La+Sr)}$ nuo 1,15 iki 1,21, metalo - izoliatoriaus fazinio virsmo temperatūra T_m pasislenka į aukštesnę temperatūrų sritį nuo 240 K iki 285 K. Esant aukštesnei nei kambario temperatūrai, didžiausios MR vertės gaunamos sluoksniams, kuriuose didžiausias Mn perteklius yra 1,15–1,21 (363 K temperatūroje $MR \approx 39\%$, kai B=20 Teslų). Gautus rezultatus galima paaiškinti La–Sr–Mn–O savilegiravimu La vakancijomis, kurios lemia stipresnį feromagnetizmą La–Sr–Mn–O sluosniuose ir optimalų Mn^{3+}/Mn^{4+} santykį.

4. Padėklo pasirinkimas nusodinant nanostruturizuotus $La_{1-x}Sr_xMn_yO_3$ manganito sluoksnius, daro didelę įtaka šių sluoksnių pagrindiniams parametrams (savitajai varžai, magnetovaržai ir jos anizotropijai) feromagnetinėje fazėje silpname magnetiniame lauke (<0,7 Teslų). Sluoksniai, kurių storis 360 nm, užauginti ant monokristalinio kvarco padėklo, pasižymi dvigubai didesne magnetovaža silpname magnetiniame lauke (31%, esant $T = 25$K), lyginant su sluoksniais, užaugintais ant polikristalinio Al_2O_3 ir amorfinio Si/SiO_2-1000 padėklų (15,5%). Tai gali sąlygota tobulesnės sluoksnių, užaugintų ant kvarco padėklo, struktūros, pasižyminčios kolonų formos kristalitais, atskirtais plonų tarpkristalitinių sričių, ir kvarco-manganito riboje susiformavusio difuzinio sluoksnio.

5. Ant skirtingų padėklų užaugintų nanostrutūrizuotų LSMO sluoksnių magnetovaržos vertės stipriame magnetiniame lauke yra panašios. Tai galima paaiškinti tuo, kad stiprus magnetinis laukas daugiausia įtakoja Mn jonų magnetinių momentų orientaciją netvarkingose tarpkristalitinėse srityse, nes tvarkingesnės struktūros kristalitų magnetiniai momentai jau pilnai suorientuojami esant ≈10 Teslų magnetiniam laukui ir jų magnetovarža jau yra praktiškai įsisotinusi.

6. Iš nanostrutūrizuotų $La_{1-x}Sr_xMn_yO_3$ manganito sluoksnių su Mn pertekliumi sukurti magnetinio lauko jutikliai gali būti naudojami elektromagnetinio metalų formavimo ir magnetinio impulsinio suvirinimo (MIS) procesų metu lokaliems magnetinio lauko dinamikos matavimams siaurame tarpelyje tarp magnetinio lauko formuotuvo ir judančios detalės.

Curriculum Vitae

Vardas, pavardė: Jonas Klimantavičius - Klimantas
Gimimo data: 1967-01-06
El. paštas: jonas.k@apertika.eu

Išsilavinimas
2015-2020 m. Valstybinis mokslinių tyrimų institutas Fizinių ir technologijos mokslų centras, Vilnius, Lietuva. Doktorantūros studijos
2002-2003 m. Baltic Management Institute (BMI), Vilnius. Verslo magistras
1993-1995 m. Vilniaus universiteto Tarptautinio verslo mokykla. Vilnius. Tarptautinio verslo specialistas
1985-1992 m. Vilniaus universitetas, Fizikos fakultetas, Vilnius. Magistras

Darbo patirtis
2015 m. - dabar. Tyrėjas, Valstybinis mokslinių tyrimų institutas Fizinių ir technologijos mokslų centras, Vilnius.
2019 m. - dabar. Ekspertas. Mokslo, inovacijų ir technologijų agentūra. Vilnius.
2010-2015 m. Direktorius, ELAS, UAB, Vilnius
2008-2010 m. Direktorius, Apertika, UAB, Vilnius
1998-2008 m. Sistemų integravimo skyriaus vadovas, Ericsson Lietuva, UAB, Vilnius

Sertifikatai
PRINCE2 projektų vadovo sertifikatas

Bibliography

[1] M. Ziese, "Extrinsic magnetotransport phenomena in ferromagnetic oxides," *Reports on Progress in Physics*, vol. 65, pp. 143–249, jan 2002.

[2] C. Israel, M. J. Calderón, and N. D. Mathur, "The current spin on manganites," *Materials Today*, vol. 10, no. 10, pp. 24–32, 2007.

[3] N. Zurauskiene, S. Balevicius, V. Stankevic, S. Kersulis, M. Schneider, O. Liebfried, V. Plausinaitiene, and A. Abrutis, "B-scalar sensor using CMR effect in thin polycrystalline manganite films," *IEEE Transactions on Plasma Science*, vol. 39, no. 1, pp. 411–416, 2011.

[4] T. Stankevič, L. Medišauskas, V. Stankevič, S. Balevičius, N. Žurauskienė, O. Liebfried, and M. Schneider, "Pulsed magnetic field measurement system based on colossal magnetoresistance B-scalar sensors for railgun investigation," *Review of Scientific Instruments*, vol. 85, no. 4, p. 044704, 2014.

[5] A. Haghiri-Gosnet and J. Renard, "CMR manganites: physics, thin films and devices," *Journal of Physics D: Applied Physics*, vol. 36, no. 8, p. R127, 2003.

[6] J. Coey and M. Viret, "Mixed-valence manganites," *Advances in Physics*, vol. 48, no. 2, pp. 167–293, 1999.

[7] J. Dhahri, S. Zemni, K. Cherif, J. Dhahri, M. Oumezzine, M. Ghedira, and H. Vincent, "The effect of deficit of strontium on structural, magnetic and electrical properties of $La_{0.8}Sr_{0.2-x}\square_xMnO_3$ manganites," *Journal of Alloys and Compounds*, vol. 394, no. 1, pp. 51 – 57, 2005.

[8] P. K. Muduli, G. Singh, R. Sharma, and R. C. Budhani, "Magnetotransport in polycrystalline la2/3sr1/3mno3 thin films of controlled granularity," *Journal of Applied Physics*, vol. 105, no. 11, p. 113910, 2009.

[9] S. Balevičius, N. Žurauskienė, V. Stankevič, S. Keršulis, V. Plaušinaitienė, A. Abrutis, S. Zherlitsyn, T. Herrmannsdörfer, J. Wosnitza, and F. Wolff-Fabris, "Nanostructured thin manganite films in megagauss magnetic field," *Applied Physics Letters*, vol. 101, no. 9, p. 092407, 2012.

[10] S. Balevičius, N. Žurauskienė, V. Stankevič, T. Herrmannsdörfer, S. Zherlitsyn, Y. Skourski, F. Wolff-Fabris, and J. Wosnitza, "CMR-B-scalar sensor application for high magnetic field measurement in nondestructive pulsed magnets," *IEEE Transactions on Magnetics*, vol. 49, no. 11, pp. 5480–5484, 2013.

[11] J. Bellmann, J. Lueg-Althoff, S. Schulze, S. Gies, E. Beyer, and A. E. Tekkaya, "Measurement and analysis technologies for magnetic pulse welding: established methods and new strategies," *Advances in Manufacturing*, vol. 4, no. 4, pp. 322–339, 2016.

[12] R. Merte, D. Peier, and J. Teunissen, "Optical position and time resolved measurement of magnetic field distribution in high speed metal forming," *In High Speed Forming 2004, Proceedings of the 1st International Conference*, pp. 261–268, 2004.

[13] V. I. Zinenko and M. S. Pavlovskii, "Lattice dynamics and the phase transition from the cubic phase to the tetragonal phase in the $LaMnO_3$ crystal within the polarizable-ion model," *Physics of the Solid State*, vol. 49, no. 9, pp. 1749–1758, 2007.

[14] L. Malavasi, "Role of defect chemistry in the properties of perovskite manganites," *J. Mater. Chem.*, vol. 18, pp. 3295–3308, 2008.

[15] W. H. Shah, K. Safeen, and G. Rehman, "Effects of divalent alkaline earth ions on the magnetic and transport features of $La_{0.65}A_{0.35}Mn_{0.95}Fe_{0.05}O_3$ (A=Ca, Sr, Pb, Ba) compounds," *Current Applied Physics*, vol. 12, no. 3, pp. 742 – 747, 2012.

[16] H. Y. Hwang, S.-W. Cheong, P. G. Radaelli, M. Marezio, and B. Batlogg, "Lattice effects on the magnetoresistance in doped $lamno_3$," *Phys. Rev. Lett.*, vol. 75, pp. 914–917, Jul 1995.

[17] H. Kronmüller and S. Parkin, *Handbook of Magnetism and Advanced Magnetic Materials: Spintronics and magnetoelectronics*. Handbook of Magnetism and Advanced Magnetic Materials, John Wiley & Sons, 2007.

[18] S. C. Tidrow, "Mapping comparison of goldschmidt's tolerance factor with perovskite structural conditions," *Ferroelectrics*, vol. 470, no. 1, pp. 13–27, 2014.

[19] G. Trimarchi and N. Binggeli, "Structural and electronic properties of $LaMno_3$ under pressure: An ab initio LDA + U study," *Phys. Rev. B*, vol. 71, p. 035101, Jan 2005.

[20] D. Y. Xing, S.-J. Xiong, and D. Feng, "Metal-insulator transition below the curie temperature in layered manganites," *Phys. Rev. B*, vol. 58, pp. 14139–14142, Dec 1998.

[21] J. P. Zhou, J. T. McDevitt, J. S. Zhou, H. Q. Yin, J. B. Goodenough, Y. Gim, and Q. X. Jia, "Effect of tolerance factor and local distortion on magnetic

properties of the perovskite manganites," *Applied Physics Letters*, vol. 75, no. 8, pp. 1146–1148, 1999.

[22] S. Cheong and H. Hwang, "Contribution to colossal magnetoresistance oxides, monographs in condensed matter science," 1999.

[23] P. Schiffer, A. P. Ramirez, W. Bao, and S.-W. Cheong, "Low temperature magnetoresistance and the magnetic phase diagram of $\mathrm{La}_{1-x}\mathrm{Ca}_x\mathrm{MnO}_3$," *Phys. Rev. Lett.*, vol. 75, pp. 3336–3339, Oct 1995.

[24] D. Fuchs, O. Morán, P. Adelmann, and R. Schneider, "Thickness-dependent Curie temperature of epitaxial $\mathrm{La}_{0.7}\mathrm{A}_{0.3}\mathrm{CoO}_3$ (A=Ca, Sr, Ba) films," *Journal of Magnetism and Magnetic Materials*, vol. 272-276, pp. E1377 – E1378, 2004. Proceedings of the International Conference on Magnetism (ICM 2003).

[25] K. I. Kugel and D. I. Khomski, "The Jahn-Teller effect and magnetism: transition metal compunds," *Usp. Fiz. Nauk*, vol. 136, pp. 621–664, Apr 1982.

[26] N. Izyumskaya, Y. Alivov, and H. Morkoç, "Oxides, oxides, and more oxides: High-κ oxides, ferroelectrics, ferromagnetics, and multiferroics," *Critical Reviews in Solid State and Materials Sciences*, vol. 34, no. 3-4, pp. 89–179, 2009.

[27] H. S. Lee and H. H. Park, "Band structure analysis of $la_{0.7}sr_{0.3}mno_3$ perovskite manganite using a synchrotron," *Advances in Condensed Matter Physics*, vol. 2015, 2015.

[28] D. Yakovlev and W. Ossau, "Magnetic polarons," *Springer Series in Materials Science*, vol. 144, 2010.

[29] J. M. D. Teresa, M. R. Ibarra, P. A. Algarabel, C. Ritter, C. Marquina, J. Blasco, J. García, A. del Moral, and Z. Arnold, "Evidence for magnetic polarons in the magnetoresistive perovskites," *Nature*, vol. 386, no. 6622, pp. 256–259, 1997.

[30] P. W. Anderson, "Antiferromagnetism. theory of superexchange interaction," *Phys. Rev.*, vol. 79, pp. 350–356, Jul 1950.

[31] P. W. Anderson, "Generalizations of the weiss molecular field theory of antiferromagnetism," *Phys. Rev.*, vol. 79, pp. 705–710, Aug 1950.

[32] C. Zener, "Interaction between the d shells in the transition metals," *Phys. Rev.*, vol. 81, pp. 440–444, Feb 1951.

[33] C. Zener, "Interaction between the d-shells in the transition metals. ii. ferromagnetic compounds of manganese with perovskite structure," *Phys. Rev.*, vol. 82, pp. 403–405, May 1951.

[34] P. W. Anderson and H. Hasegawa, "Considerations on double exchange," *Phys. Rev.*, vol. 100, pp. 675–681, Oct 1955.

[35] P. Bastiaansen and H. Knops, "Percolation mechanism for colossal mag-

netoresistance," *Journal of Physics and Chemistry of Solids*, vol. 59, no. 3, pp. 297 – 303, 1998.

[36] L. Zhang, C. Israel, A. Biswas, R. L. Greene, and A. de Lozanne, "Direct observation of percolation in a manganite thin film," *Science*, vol. 298, no. 5594, pp. 805–807, 2002.

[37] B. Raveau, A. Maignan, C. Martin, and M. Hervieu, "Colossal magnetoresistance manganite perovskites: relations between crystal chemistry and properties," *Chemistry of Materials*, vol. 10, no. 10, pp. 2641–2652, 1998.

[38] M. Viret, L. Ranno, and J. D. Coey, "Magnetic localization in mixed-valence manganites," *Physical Review B*, vol. 55, no. 13, p. 8067, 1997.

[39] S. Jin, T. H. Tiefel, M. McCormack, R. Fastnacht, R. Ramesh, L. Chen, *et al.*, "Thousandfold change in resistivity in magnetoresistive La-Ca-Mn-O films," *Science-AAAS-Weekly Paper Edition-including Guide to Scientific Information*, vol. 264, no. 5157, pp. 413–414, 1994.

[40] J. Fontcuberta, B. Martínez, A. Seffar, S. Piñol, J. L. García-Muñoz, and X. Obradors, "Colossal magnetoresistance of ferromagnetic manganites: Structural tuning and mechanisms," *Phys. Rev. Lett.*, vol. 76, pp. 1122–1125, Feb 1996.

[41] A. Gupta, G. Gong, G. Xiao, P. Duncombe, P. Lecoeur, P. Trouilloud, Y. Wang, V. Dravid, and J. Sun, "Grain-boundary effects on the magnetoresistance properties of perovskite manganite films," *Physical Review B*, vol. 54, no. 22, p. R15629, 1996.

[42] R. Shreekala, M. Rajeswari, K. Ghosh, A. Goyal, J. Y. Gu, C. Kwon, Z. Trajanovic, T. Boettcher, R. L. Greene, R. Ramesh, and T. Venkatesan, "Effect of crystallinity on the magnetoresistance in perovskite manganese oxide thin films," *Applied Physics Letters*, vol. 71, no. 2, pp. 282–284, 1997.

[43] K. Steenbeck, T. Eick, K. Kirsch, K. O'Donnell, and E. Steinbeiß, "Influence of a 36.8° grain boundary on the magnetoresistance of $La_{0.8}Sr_{0.2}MnO_{3-\delta}$ single crystal films," *Applied Physics Letters*, vol. 71, no. 7, pp. 968–970, 1997.

[44] N. D. Mathur, G. Burnell, S. P. Isaac, T. J. Jackson, B.-S. Teo, J. L. MacManus-Driscoll, L. F. Cohen, J. E. Evetts, and M. G. Blamire, "Large low-field magnetoresistance in $La_{0.7}Ca_{0.3}MnO_3$ induced by artificial grain boundaries," *Nature*, vol. 387, pp. 266–268, May 1997.

[45] X. W. Li, A. Gupta, G. Xiao, and G. Q. Gong, "Low-field magnetoresistive properties of polycrystalline and epitaxial perovskite manganite films," *Applied Physics Letters*, vol. 71, no. 8, pp. 1124–1126, 1997.

[46] A. Gupta, T. R. McGuire, P. R. Duncombe, M. Rupp, J. Z. Sun, W. J. Gallagher, and G. Xiao, "Growth and giant magnetoresistance proper-

ties of La−deficient $La_xMnO_{3-\delta}$ $(0.67 \leqslant x \leqslant 1)$ films," *Applied Physics Letters*, vol. 67, no. 23, pp. 3494–3496, 1995.

[47] K. Zhang, J. Dai, X. Zhu, X. Zhu, X. Zuo, P. Zhang, L. Hu, W. Lu, W. Song, Z. Sheng, W. Wu, Y. Sun, and Y. Du, "Vertical $La_{0.7}Ca_{0.3}MnO_3$ nanorods tailored by high magnetic field assisted pulsed laser deposition," *Scientific Reports*, vol. 6, p. 19483, Jan 2016.

[48] C.-W. Chong, D. Hsu, W.-C. Chen, C.-C. Li, Y.-F. Huang, H.-C. Han, J. G. Lin, L.-C. Chen, K.-H. Chen, and Y.-F. Chen, "Giant room temperature electric-field-assisted magnetoresistance in $La_{0.7}Sr_{0.3}MnO_3$/n-Si nanotip heterojunctions," *Nanotechnology*, vol. 22, p. 125701, feb 2011.

[49] C.-H. Hsu, H.-C. Lo, C.-F. Chen, C. T. Wu, J.-S. Hwang, D. Das, J. Tsai, L.-C. Chen, and K.-H. Chen, "Generally applicable self-masked dry etching technique for nanotip array fabrication," *Nano Letters*, vol. 4, no. 3, pp. 471–475, 2004.

[50] A. Abrutis, V. Plausinaitiene, V. Kubilius, A. Teiserskis, Z. Saltyte, R. Butkute, and J. Senateur, "Magnetoresistant $La_{1-}Sr_xMnO_3$ films by pulsed injection metal organic chemical vapor deposition: effect of deposition conditions, substrate material and film thickness," *Thin Solid Films*, vol. 413, no. 1, pp. 32 – 40, 2002.

[51] V. Stankevič, F. Anisimovas, A. Abrutis, V. Plaušinaitienė, J. Novickij, and S. Bartkevičius, "Preparation and properties of polycrystalline and epitaxial manganite films for pulsed magnetic field application," *Elektronika ir Elektrotechnika*, vol. 61, pp. 38–38, May 2005.

[52] X. Liu, Z. Jiao, K. Nakamura, T. Hatano, and Y. Zeng, "The grain size dependence of the resistance behaviors in doped lanthanum manganite polycrystalline films," *Journal of Applied Physics*, vol. 87, no. 5, pp. 2431–2436, 2000.

[53] A. Moreo, S. Yunoki, and E. Dagotto, "Phase separation scenario for manganese oxides and related materials," *Science*, vol. 283, no. 5410, pp. 2034–2040, 1999.

[54] M. Uehara, S. Mori, C. H. Chen, and S.-W. Cheong, "Percolative phase separation underlies colossal magnetoresistance in mixed-valent manganites," *Nature*, vol. 399, pp. 560–563, Jun 1999.

[55] M. Mayr, A. Moreo, J. A. Vergés, J. Arispe, A. Feiguin, and E. Dagotto, "Resistivity of mixed-phase manganites," *Phys. Rev. Lett.*, vol. 86, pp. 135–138, Jan 2001.

[56] M. Julliere, "Tunneling between ferromagnetic films," *Physics Letters A*, vol. 54, no. 3, pp. 225 – 226, 1975.

[57] M. B. Stearns], "Simple explanation of tunneling spin-polarization of Fe, Co, Ni and its alloys," *Journal of Magnetism and Magnetic Materials*, vol. 5,

no. 2, pp. 167 – 171, 1977.

[58] S. Maekawa and U. Gafvert, "Electron tunneling between ferromagnetic films," *IEEE Transactions on Magnetics*, vol. 18, no. 2, pp. 707–708, 1982.

[59] T. Miyazaki and N. Tezuka, "Giant magnetic tunneling effect in $Fe/Al_2O_3/Fe$ junction," *Journal of Magnetism and Magnetic Materials*, vol. 139, no. 3, pp. L231 – L234, 1995.

[60] J. C. Slonczewski, "Conductance and exchange coupling of two ferromagnets separated by a tunneling barrier," *Phys. Rev. B*, vol. 39, pp. 6995–7002, Apr 1989.

[61] Y. Qi, D. Y. Xing, and J. Dong, "Relation between julliere and slonczewski models of tunneling magnetoresistance," *Phys. Rev. B*, vol. 58, pp. 2783–2787, Aug 1998.

[62] L. I. GLAZMAN, "Inelastic tunneling across thin amorphous films," *Sov. Phys. JETP*, vol. 67, no. 6, pp. 1276–1282, 1988.

[63] C. Höfener, J. B. Philipp, J. Klein, L. Alff, A. Marx, B. Büchner, and R. Gross, "Voltage and temperature dependence of the grain boundary tunneling magnetoresistance in manganites," *Europhysics Letters (EPL)*, vol. 50, pp. 681–687, jun 2000.

[64] J. Inoue and S. Maekawa, "Theory of tunneling magnetoresistance in granular magnetic films," *Phys. Rev. B*, vol. 53, pp. R11927–R11929, May 1996.

[65] N. F. Mott and E. A. Davis, *Electronic processes in non-crystalline materials*. Clarendon Press, 2012.

[66] P. H. Wagner, V. Metlushko, L. Trappeniers, A. Vantomme, J. Vanacken, G. Kido, V. V. Moshchalkov, and Y. Bruynseraede, "Magnetotransport in epitaxial thin films of the magnetic perovskite $Pr_{0.5}Sr_{0.5}MnO_3$," *Phys. Rev. B*, vol. 55, pp. 3699–3707, Feb 1997.

[67] B. Belevtsev, V. Krasovitsky, D. Naugle, K. Rathnayaka, A. Parasiris, S. Surthi, R. Pandey, and M. Rom, "Transport and magnetic anisotropy in cmr thin film $La_{1-x}Ca_xMnO_3$ $(x \approx 1/3)$ induced by a film-substrate interaction," *ArXiv Preprint cond-mat/0103493*, 2001.

[68] N. ŽURAUSKIENĖ, S. KERŠULIS, L. MEDIŠAUSKAS, and S. TOLVAIŠIENĖ, "Investigation of magnetoresistance and its anisotropy of thin polycrystalline $La_{0.83}Sr_{0.17}MnO_3$ films in high pulsed magnetic fields.," *Acta Physica Polonica, A*, vol. 119, no. 2, pp. 186 – 188, 2011.

[69] V. Shribman, "Magnetic pulse welding of automotive hvac parts," *Acta Physica Polonica, A*, pp. 1–25, 2006.

[70] A. Kapil and A. Sharma, "Magnetic pulse welding: an efficient and environmentally friendly multi-material joining technique," *Journal of Cleaner Production*, vol. 100, pp. 35 – 58, 2015.

[71] R. M. Miranda, B. Tomas, T. G. Santos, and N. Fernandes, "Magnetic pulse welding on the cutting edge of industrial applications," *Soldagem & Inspecao*, vol. 19, pp. 69 – 81, 03 2014.

[72] M. Ishak, *Joining Technologies*. IntechOpen, 2016.

[73] D. Pereira, J. P. Oliveira, T. Pardal, R. M. Miranda, and T. G. Santos, "Magnetic pulse welding: machine optimisation for aluminium tubular joints production," *Science and Technology of Welding and Joining*, vol. 23, no. 2, pp. 172–179, 2018.

[74] A. Abrutis, V. Plausinaitiene, V. Kubilius, A. Teiserskis, Z. Saltyte, R. Butkute, and J. Senateur, "Magnetoresistant La_{1-x} Sr_xMnO_3 films by pulsed injection metal organic chemical vapor deposition: effect of deposition conditions, substrate material and film thickness," *Thin Solid Films*, vol. 413, no. 1, pp. 32–40, 2002.

[75] Felten, F., Senateur, J. P., Weiss, F., Madar, R., and Abrutis, A., "Deposition of oxide layers by computer controlled"injection-lpcvd"," *J. Phys. IV France*, vol. 05, no. 5, pp. 1079–1086, 1995.

[76] G. H. Beall, "Milestones in glass-ceramics: A personal perspective," *International Journal of Applied Glass Science*, vol. 5, no. 2, pp. 93–103, 2014.

[77] A. S. Cooper, "Precise lattice constants of germanium, aluminum, gallium arsenide, uranium, sulphur, quartz and sapphire," *Acta Crystallographica*, vol. 15, pp. 578–582, Jun 1962.

[78] H. Kawano, R. Kajimoto, M. Kubota, and H. Yoshizawa, "Canted antiferromagnetism in an insulating lightly doped $La_{1-x}Sr_xMnO_3$ with x$\leqslant$0.17," *Phys. Rev. B*, vol. 53, pp. 2202–2205, Feb 1996.

[79] G. C. Firth and V. E. Watkins Jr, "An interim report on investigation of low-temperature solders for cryogenic wind tunnel models," *Welding, Bonding, and Fastening*, p. 21, 1984.

[80] D. Pavilonis, *Investigation of magnetoresistance and resistance relaxation of La-Sr(Ca)-MnO nanostructured films*. PhD thesis, 2017.

[81] "Apiezon N Grease: Cryogenic high vacuum grease properties," *M & I Materials Ltd.*, 2020.

[82] A. Grainys, J. Novickij, T. Stankevič, V. Stankevič, V. Novickij, and N. Žurauskienė, "Single Pulse Calibration of Magnetic Field Sensors Using Mobile 43 kJ Facility," *Measurement Science Review*, vol. 15, no. 5, pp. 244 – 247, 2015.

[83] J. Lueg-Althoff, A. Lorenz, S. Gies, C. Weddeling, G. Goebel, A. E. Tekkaya, and E. Beyer, "Magnetic pulse welding by electromagnetic compression: Determination of the impact velocity," in *Tribology in Manufacturing Processes & Joining by Plastic Deformation*, vol. 966 of *Advanced Materials Research*, pp. 489–499, Trans Tech Publications Ltd, 7 2014.

[84] S. Balevičius, N. Žurauskienė, V. Stankevič, S. Keršulis, V. Plaušinaitienė, A. Abrutis, S. Zherlitsyn, T. Herrmannsdörfer, J. Wosnitza, and F. Wolff-Fabris, "Nanostructured thin manganite films in megagauss magnetic field," *Applied Physics Letters*, vol. 101, no. 9, p. 092407, 2012.

[85] T. Stankevič, L. Medišauskas, V. Stankevič, S. Balevičius, N. Žurauskienė, O. Liebfried, and M. Schneider, "Pulsed magnetic field measurement system based on colossal magnetoresistance-B-scalar sensors for railgun investigation," *Review of Scientific Instruments*, vol. 85, no. 4, p. 044704, 2014.

[86] M. Zacharias and P. Streitenberger, "Crystallization in the limit of ultra thin layers- a new crystallization model," *MRS Proceedings*, vol. 638, p. F6.2.1, 2000.

[87] M. Zacharias, J. Bläsing, K. Hirschman, L. Tsybeskov, and P. Fauchet, "Extraordinary crystallization of amorphous Si/SiO_2 superlattices," *Journal of Non-Crystalline Solids*, vol. 266-269, pp. 640 – 644, 2000.

[88] M. Zacharias and P. Streitenberger, "Crystallization of amorphous superlattices in the limit of ultrathin films with oxide interfaces," *Phys. Rev. B*, vol. 62, pp. 8391–8396, Sep 2000.

[89] M. B. Salamon and M. Jaime, "The physics of manganites: Structure and transport," *Rev. Mod. Phys.*, vol. 73, pp. 583–628, Aug 2001.

[90] J. Evetts, M. Blamire, N. Mathur, S. Isaac, B. Teo, L. Cohen, and J. Macmanus-Driscoll, "Defect-induced spin disorder and magnetoresistance in single-crystal and polycrystal rare-earth manganite thin films," *Philosophical Transactions-Royal Society of London Series A: Mathematical Physical and Engineering Sciences*, pp. 1593–1616, 1998.

[91] K. Dörr, "Ferromagnetic manganites: spin-polarized conduction versus competing interactions," *Journal of Physics D: Applied Physics*, vol. 39, no. 7, p. R125, 2006.

[92] C. Dubourdieu, M. Audier, H. Roussel, J. P. Sénateur, and J. Pierre, "Crystallization and related magnetotransport properties of amorphous manganite films grown by metalorganic chemical vapor deposition," *Journal of Applied Physics*, vol. 92, no. 1, pp. 379–384, 2002.

[93] P. Wagner, I. Gordon, L. Trappeniers, J. Vanacken, F. Herlach, V. Moshchalkov, and Y. Bruynseraede, "Spin dependent hopping and colossal negative magnetoresistance in epitaxial $Nd_{0.52}$ $Sr_{0.48}MnO_3$ films in fields up to 50 T," *Physical Review Letters*, vol. 81, no. 18, p. 3980, 1998.

[94] J. Colino and A. De Andrés, "Huge magnetoresistance in ultrathin $La_{0.7}Ca_{0.3}MnO_3$ films: The role of superparamagnetic clusters and domain walls," *Applied Physics Letters*, vol. 87, no. 14, p. 142509, 2005.

[95] P. Mandal, P. Choudhury, K. Bärner, R. von Helmolt, and A. Jansen, "Magnetotransport properties of $La_{2/3}Sr_{1/3}MnO_3$ thin film," *Journal of Applied Physics*, vol. 91, no. 9, pp. 5940–5944, 2002.

[96] N. Zurauskiene, S. Balevicius, V. Stankevic, S. Kersulis, J. Klimantavicius, V. Plausinaitiene, V. Kubilius, M. Skapas, R. Juskenas, and R. Navickas, "Magnetoresistive properties of thin nanostructured manganite films grown by metalorganic chemical vapour deposition onto glass-ceramics substrates," *Journal of Materials Science*, vol. 53, pp. 12996–13009, Sep 2018.

[97] N. Žurauskienė, S. Balevičius, D. Pavilonis, V. Stankevič, V. Plaušinaitienė, S. Zherlitsyn, T. Herrmannsdörfer, J. M. Law, and J. Wosnitza, "Magnetoresistance and resistance relaxation of nanostructured la-ca-mno films in pulsed magnetic fields," *IEEE Transactions on Magnetics*, vol. 50, no. 11, pp. 1–4, 2014.

[98] H. Gencer, M. Gunes, A. Goktas, Y. Babur, H. Mutlu, and S. Atalay, "Labamno films produced by dip-coating on a quartz substrate," *Journal of Alloys and Compounds*, vol. 465, no. 1, pp. 20 – 23, 2008.

[99] I. Marozau, P. T. Das, M. Döbeli, J. G. Storey, M. A. Uribe-Laverde, S. Das, C. Wang, M. Rössle, and C. Bernhard, "Influence of La and Mn vacancies on the electronic and magnetic properties of $LaMnO_3$ thin films grown by pulsed laser deposition," *Phys. Rev. B*, vol. 89, p. 174422, May 2014.

[100] P. A. Joy, C. R. Sankar, and S. K. Date, "The limiting value of x in the ferromagnetic compositions $La_{1-x}MnO_3$," *Journal of Physics: Condensed Matter*, vol. 14, pp. L663–L669, sep 2002.

[101] F. Figueiras, J. Araùjo, V. Amaral, P. Tavares, J. Sousa, and J. Vieira, "Structural and magnetic study of self- doped $La_{1-x-y}Ca_x\emptyset_yMnO_3$," *Journal of Magnetism and Magnetic Materials*, vol. 272-276, pp. 1753 – 1755, 2004. Proceedings of the International Conference on Magnetism (ICM 2003).

[102] J. Araújo, V. Amaral, P. Tavares, F. Lencart-Silva, A. Lourenço, J. Sousa, and J. Vieira, "Doping manganites by la-site vacancies and ca ions: bulk ceramics and thin films," *Journal of Magnetism and Magnetic Materials*, vol. 226-230, pp. 821 – 823, 2001. Proceedings of the International Conference on Magnetism (ICM 2000).

[103] P. B. Tavares, V. S. Amaral, J. P. Araújo, J. B. Sousa, A. A. C. S. Lourenço, and J. M. Vieira, "Substrate, annealing, and mn excess effects on La–Ca–MnO_3 thin films grown by metalorganic chemical vapor deposition: A way to room-temperature T_C," *Journal of Applied Physics*, vol. 85, no. 8, pp. 5411–5413, 1999.

[104] F. Figueiras, J. M. Vieira, M. Guzik, J. Legendziewicz, P. B. Tavares,

and V. S. Amaral, "The effects of Ca and Mn excess co-doping in CMR manganites solid solution structures," in *Advanced Materials Forum III*, vol. 514 of *Materials Science Forum*, pp. 294–298, Trans Tech Publications Ltd, 4 2006.

[105] I.-B. Shim, C.-S. Kim, K.-T. Park, and Y.-J. Oh, "Role of intermediate layer for $La_{2/3}Sr_{1/3}MnO_3/SiO_2/Si(100)$ granular thin films," *Journal of Magnetism and Magnetic Materials*, vol. 226-230, pp. 1672 – 1674, 2001. Proceedings of the International Conference on Magnetism (ICM 2000).

[106] Y.-M. Kang, A. N. Ulyanov, S.-Y. Lee, and S.-I. Yoo, "Low field magnetoresistance properties of $(La_{0.75}Sr_{0.25})_{1.05}Mn_{0.95}O_3$ polycrystalline thin films on a-SiO_2/Si substrates prepared by ex-situ solid phase crystallization," *Metals and Materials International*, vol. 17, pp. 1045–1053, Dec 2011.

[107] H. Y. Hwang, S.-W. Cheong, N. P. Ong, and B. Batlogg, "Spin-polarized intergrain tunneling in $La_{2/3}Sr_{1/3}MnO_3$," *Phys. Rev. Lett.*, vol. 77, pp. 2041–2044, Sep 1996.

[108] S. Lee, H. Y. Hwang, B. I. Shraiman, W. D. Ratcliff, and S.-W. Cheong, "Intergrain magnetoresistance via second-order tunneling in perovskite manganites," *Phys. Rev. Lett.*, vol. 82, pp. 4508–4511, May 1999.

[109] V. Psyk, D. Risch, B. Kinsey, A. Tekkaya, and M. Kleiner, "Electromagnetic forming—a review," *Journal of Materials Processing Technology*, vol. 211, no. 5, pp. 787 – 829, 2011. Special Issue: Impulse Forming.

[110] M. Kleiner, C. Beerwald, and W. Homberg, "Analysis of process parameters and forming mechanisms within the electromagnetic forming process," *CIRP Annals*, vol. 54, no. 1, pp. 225 – 228, 2005.

[111] A. Henselek, M. Beerwald, and B. C., "Design and adaptation of emf equipment – from direct acting multi-turn coils to separable tool coils for electromagnetic tube compression," *1st International Conference on High Speed Forming*, pp. 275 – 284, 3 2004.

[112] J. Lueg-Althoff, J. Bellmann, S. Gies, S. Schulze, A. E. Tekkaya, and E. Beyer, "Influence of the flyer kinetics on magnetic pulse welding of tubes," *Journal of Materials Processing Technology*, vol. 262, pp. 189 – 203, 2018.

[113] M. Schneider, R. Schneider, V. Stankevic, S. Balevicius, and N. Zurauskiene, "Highly local measurements of strong transient magnetic fields during railgun experiments using CMR-based sensors," *IEEE Transactions on Magnetics*, vol. 43, pp. 370–375, Jan 2007.

[114] M. Schneider, O. Liebfried, V. Stankevic, S. Balevicius, and N. Zurauskiene, "Magnetic diffusion in railguns: Measurements using CMR-based sensors," *IEEE Transactions on Magnetics*, vol. 45,

no. 1, pp. 430–435, 2009.

Publications by the Author

Publications on the Topic of Dissertation

Journals in the list of ISI Web of Knowledge

P1. N. Žurauskienė, S. Balevičius, V. Stankevič, S. Keršulis, **J. Klimantavičius**, V. Plaušinaitienė, V. Kubilius, M. Skapas, R. Juškėnas, R. Navickas. Magnetoresistive properties of thin nanostructured manganite films grown by metalorganic chemical vapour deposition onto glass-ceramics substrates. **Journal of Materials Science**. New York : Springer. ISSN 0022-2461. eISSN 1573-4803. 2018, vol. 53, iss. 18, p. 12996-13009. DOI: 10.1007/s10853-018-2567-y.

P2. N. Žurauskienė, V. Stankevič, S. Keršulis, **J. Klimantavičius**, Č. ŠimkevičiusV. Plaušinaitienė, M. Vagner, S. Balevičius. Increase of operating temperature of magnetic field sensors based on La–Sr–Mn–O films with Mn excess. **IEEE Transactions on Plasma Science**. 2019, vol. 47, iss. 10, p. 4530-4535. DOI: 10.1109/TPS.2019.2911545.

P3. B. Vengalis, G. Grigaliūnaitė-Vonsevičienė, A.Maneikis, **J. Klimantavičius**, R. Juškėnas, K.Mažeika. Low-field magnetoresistance and switching behavior of polycrystalline $La_{0.66}Sr_{0.34}MnO_3$/YSZ(001) films with columnar grain structure. **Thin Solid Films**. 2017, vol. 625, p. 42–48. DOI: 10.1016/j.tsf.2017.01.040.

P4. V. Stankevic, J. Lueg-Althoff, M. Hahn, A. E. Tekkaya, N. Zurauskiene, J. Dilys, **J. Klimantavičius**, S. Kersulis, C. Simkevicius, S. Balevicius. Magnetic field measurements during magnetic pulse welding using CMR-B-scalar sensors. **Sensors**. 2020, vol. 20, art. no. 5925. DOI: 10.3390/s20205925.

Conference proceedings

P5. V. Stankevič, N. Žurauskienė, S. Balevičius, S. Keršulis, Č. Šimkevičius, **J. Klimantavičius**. High Pulsed Magnetic Fields: Measurement with Magnetoresistive Sensors. **Proceedings of 15th Symposium Magnetoresistive Sensors and Magnetic Systems**. 19th – 20th March 2019, Wetzlar, Sensitec GmbH, p.1-8.

Publications not included in the Dissertation

1. N. Žurauskienė, D. Pavilonis, J. Klimantavičius, S. Balevičius, V. Stankevič, R. Vasiliauskas, V. Plaušinaitienė, A. Abrutis, M. Skapas, R. Juškėnas (2017) Magnetoresistance Relaxation Anisotropy of Nanostructured La-Sr(Ca)-Mn-O Films Induced by High-Pulsed Magnetic Fields. IEEE Transactions on Plasma Science, VOL. 45 NO. 11, DOI: 10.1109/TPS.2017.2688727.
2. N. Žurauskienė, D. Pavilonis, J. Klimantavičius, S. Balevičius, V. Stankevič, S.Keršulis, V. Plaušinaitienė, A. Abrutis, R. Lukošė, M. Skapas, R. Juškėnas, B. Knašienė, E. Naujalis, J. M. Law (2017) Influence of MOCVD Growth Pressure on Magnetoresistance of Nanostructured La-Ca-Mn-O Films Used for Magnetic Field Sensors. IEEE Transactions on Plasma Science, VOL. 45 NO. 11, DOI: 10.1109/TPS.2017.2711032.

Conference presentations

C1. V. Stankevič, N. Žurauskienė, S. Balevičius, S. Keršulis, Č. Šimkevičius, J. Klimantavičius. High Pulsed Magnetic Fields: Measurement with Magnetoresistive Sensors. 15th XMR-Symposium „Magnetoresistive Sensors and Magnetic Systems" Wetzlar, Germany, March 19-20, 2019.

C2. N. Žurauskienė, S. Keršulis, V. Stankevič, V. Plaušinaitienė, J.Klimantavičius, S. Balevičius. Increase of operating temperature of magnetic field sensors based on La–Sr–Mn–O films with Mn excess. 7th Euro-Asian pulsed power conference EAPPC & BEAMS 2018, Changsha, China, September 16-20, 2018.

C3. N. Žurauskienė, Vakaris Rudokas, Saulius Balevičius, Voitech Stankevič, Skirmantas Keršulis, Jonas Klimantavičius, Valentina Plaušinaitienė, Milita Vagner, Adulfas Abrutis, Rasuolė Lukošė, Martynas Skapas, Remigijus

Juškenas, Romualdas Navickas. Nanostructured manganite-cobaltite thin films for pulsed magnetic field sensing: physics and applications, Collaborative Conference on Materials Research CCMR 2017, Jeju, South Korea, June 26-30, 2017.

C4. J. Klimantavičius. Development of Sensors and Measurement Systems for Pulsed Magnetic Field. Poster presentation. 14th Symposium "Magnetoresistive sensors and magnet systems", Wetzlar, Germany, March 21-22, 2017.

C5. J. Klimantavicius, V. Rudokas, N. Zurauskiene, C. Simkevicius, S. Kersulis, V. Stankevic, S. Balevicius, D. Pavilonis, R. Vasiliauskas, S. Tolvaisiene, V. Plausinaitiene. Multi-Step Accelerated Ageing of Magnetic Field Sensors Based on Nanostructured La-Sr-Mn-O Thin Films. Poster presentation. 6th Euro- Asian pulsed power conference EAPPC 2016, Estoril, Portugal, September 18-22, 2016.

NOTES

NOTES

NOTES

Vilniaus universiteto leidykla
Saulėtekio al. 9, III rūmai, LT-10222 Vilnius
El. p. info@leidykla.vu.lt, www.leidykla.vu.lt
Tiražas 20 egz.